Modeling, Simulation, Hardware Development, and Testing of a Lab-Scale Airborne Wind Energy System

by

Andreas Klein-Miloslavich
B.Sc., Simon Bolivar University, 2016

A Thesis Submitted in Partial Fulfillment of the
Requirements for the Degree of

MASTER OF APPLIED SCIENCES

in the Department of Mechanical Engineering

Modeling, Simulation, Hardware Development, and Testing of a Lab-Scale Airborne Wind Energy System

by

Andreas Klein-Miloslavich
B.Sc., Simon Bolivar University, 2016

Supervisory Committee

Dr. Curran Crawford, Supervisor
(Department of Mechanical Engineering)

Dr. Afzal Suleman, Departmental Member
(Department of Mechanical Engineering)

ABSTRACT

Airborne Wind Energy Systems (AWES) harness the power of high-altitude winds using tethered planes or kites. Continuous and reliable operation requires that AWES become autonomous devices, but the wind intermittency forces the system to repeatedly take-off to start, and land to shut-off. Therefore, a common approach to facilitate the operation is implementing Vertical take-off and landing (VTOL) functionality. This thesis models and simulates AWES flights working towards the implementation of flight controller hardware and autonomous operation of an AWES demonstrator platform.

The `Ardupilot` open-source autopilot platform provides a convenient tool for modeling, simulation, and hardware implementation of small-scale airplanes. An AWES lab-scale demonstrator was developed to obtain operational insight, get preliminary flight data, and real-world experience in this technology. A quadplane was developed by combining a structurally reinforced glider with VTOL and autopilot components. Its performance is obtained from static and aerodynamic studies and converted into the `Ardupilot` parameter format to define it in the simulation.

An AWES flight model was developed from the ground up to evaluate the performance of a simple flight controller in trajectory tracking. The `Ardupilot` Software-in-Loop (SIL) tool expands the simulation capabilities by running the flight controller code without requiring any hardware. This allowed controller tuning and flight plan evaluation with a more advanced fight model. AWES crosswind flight simulation was only possible due to the incorporation of an elastic tether and an ideal winch into the physics model. As a result, different trajectories and configurations were tested to find the optimal parameters that were uploaded to the flight controller board.

The operational capabilities of the AWES demonstrator were expanded with a flight testing campaign. By targeting individual objectives, each test gradually increased its complexity and ensured that the flight envelope was safely expanded. The results were validated with the simulation before moving on to the next flight test. The testing campaign is still underway due to challenges and limitations presented by the legal and logistical aspects of operating the quadplane. However, preliminary flight tests in VTOL mode have been completed and were consistent with the simulated results in terms of autonomous waypoint navigation and attitude control.

Table of Contents

List of Tables

List of Figures

ACKNOWLEDGEMENTS

I would like to thank:

My supervisor Dr. Curran Crawford for his mentorship and patience, for teaching me to understand and tackle challenges from another perspective, and for believing in me.

The University of Victoria and IESVic for providing a friendly learning environment. For the resources and opportunities provided throughout the program, and for encouraging personal and professional development.

Mrs. Sue Walton and Mrs. Pauline Sheppard for always being supportive, and for having the patience to order the many parts and pieces required for this project.

The Mechanical Engineering students that were involved in this project, specially Jack Baker, Steven Samuel, and Aidan Polglase. Without them, the project wouldn't have reached this stage.

Dr. Frederic Bourgault for the continuous advice and for representing the team at a conference presentation. And the CfAR crew for providing guidance in the legal and technical aspects of making the flight tests possible.

Bob and Marleen for sharing their kindness and love, and for making their home my own. And Rad and Markus for their friendship and support, and for always being available to brainstorm ideas and challenges in the whiteboard.

A Papa, Mama, Stefi, and Tania for their love and encouragement, and for being so close no matter how far.

Charlotte, for her love and laughs. She drives me everyday to become a better person and see the bright side of things.

DEDICATION

To Stefi & Tania, if you think that something is too big to accomplish, break it down into smaller pieces, and put the effort to work your way through.

Chapter 1

Airborne Wind Energy and a Review of Technologies

The world has realized that it needs to take action against climate change. A group of nations around the world came together to adopt The Paris Agreement [1], the main purpose being to act against climate change and help the most vulnerable to adapt to its consequences. It defines an ultimate objective of avoiding a global temperature increase of $2°C$ by 2100. The main actions are being done through implementing a robust and transparent framework for developing technologies that will reduce total greenhouse gas emissions, and provide impetus to transitioning and developing countries to organize their long term goals against climate change.

The Intergovernmental Panel on Climate Change (IPCC) published that the energy and heating sector accounts for 25% of the global greenhouse gas emissions of which 28% is represented by electricity generation worldwide [2]. With the undeniable consequences of climate change, investments, research, and policies are increasingly favoring growing renewable industries such as wind power, solar photovoltaic (PV), and grid-scale energy storage. More and more specialized technologies are emerging to provide a particular solution to an energy challenge: (1) negative emission plants that suck the carbon out of the air are being tested, (2) ocean energy devices that harness the power from tides and waves provide clean electricity to coastal remote communities, (3) small-scale wind turbines are placed in crowded cities to harness the wind from every direction, and so on. Our society is on the verge of an energy revolution. Now is the time to develop smart and innovative technology to power our civilization and contribute to the $2°C$ goal and keep developing until shifting the

trend of the greenhouse gas emission.

An innovative technology that uses an old concept has grown in interest in the last couple of decades. Airborne Wind Energy Systems (AWES) claim that theoretically they can power the entire civilization by harnessing the power of high-altitude winds using kites. Practically, AWES are still in an early stage of development and are not commercially available yet. The next section presents an overview of the technology, challenges, and leading companies.

1.1 Airborne Wind Energy Systems

In 1980 Myles Loyd described the power equations of a tethered flying wing [3]. The idea was to either generate power from the tension produced by the aerodynamic lift force through tension, or by the drag of onboard rotors while flying a tethered kite in crosswind motion. However, at the time the idea was presented, flight automation was the main hindrance to this technology. It was just in the last decade that advances in computers, composite materials, sensors, and flight controllers allowed development of Loyd's idea. A particular case is the increased development of the drone industry and the continuous growth in its applications, this allowed them to become easily accessible to any kind of consumer. Today, we have drones that can autonomously and seamlessly follow us around [4], equipped with coin-size computers with unimaginable capacities a few decades ago. These solutions for automation and controls are closing the computational gap and shifting the challenge to the seamless integration of areas such as aerodynamics, aeroelasticity, controls, power generation and grid integration, environmental conditions, regulations, and social acceptance. Only a combined effort will push the industry towards commercialization and will continue to assist in the fight against climate change.

The ultimate goal of AWES is to reduce the cost of electricity by decreasing the capital costs and increasing the capacity factor. The first, suggest replacing the bulky, non-generating components of conventional wind turbines with smart controls, and lightweight strong composite structures. The latter suggests decreasing the intermittency of wind power generation. Wind turbines are fixed to harness the energy that is available only at the design height while airborne wind turbines have the flexibility to shift their flight altitude to maintain the designed operation wind speeds, consequently increasing the reliability of the energy production. A study that compares the production costs from conventional wind turbines with AWES concludes that AWES

with the same rated power have half of the production costs [5]. This assumes that the structural and non-generating parts of conventional wind turbines have higher costs than all the sensors and advanced controllers required to produce AWES.

The technology is not yet mature to confidently say where it will be implemented. However, with its capacity to operate over 80-500 m altitudes, considered as high-altitude, it can see a significant improvement in the wind power density [6], making the locations for deployment almost unlimited. For now, a few AWES companies are targeting small-scale generation such as off-grid communities that rely only on high-cost diesel fuel electricity, among them are mines, resorts, fishing and agricultural villages. In contrast, others continue to pursue and develop grid-scale devices for either on-shore or floating off-shore generation.

Loyd describes that the key to generating electricity from the wind with a kite lies on crosswind flight. This approach has the potential to generate as much power as a conventional wind turbine but with significantly less infrastructure and therefore with reduced costs. The foundation of this idea is that the force generated by an airfoil is proportional to the square of its apparent velocity, the airfoil is assumed to fly completely perpendicular to the wind direction, and that the lift force is in the same direction as the tether tension.

$$P_{Loyd} = \frac{2}{27}\rho A_k v_w^3 \frac{C_L^3}{C_D^2} \tag{1.1}$$

The power limit P_{Loyd} represents the maximum power that can be harnessed from the wind using a crosswind kite system: ρ is the density of the air, A_k is the planform area of the kite, v_w the wind speed, and C_L and C_D the aerodynamic lift and drag coefficients respectively. To better represent the potential of AWES it is best to make a simple comparison to a conventional wind turbine. The Enercon E-126 wind turbine with a rated power of 7.58 MW has a rotor diameter of 127 m (blade of 63.5 m long) [7]. Using the power curve, the rated power is obtained at hub-height wind speeds of 16 m/s. Using the Makani Wing 7 prototype specifications [8] we can reverse-calculate the size of a AWES wing required to obtain the same power output. A wing with $C_L = 1.7$, $C_D = 0.06$, and aspect ratio of 16, flying at steady uniform wind speeds of 16 m/s requires a wingspan of approximately 22 m to have a theoretical rated power of 7.58 MW. Evidently, this comparison is not accurate because the wind turbine power curve used is based on real power while the equation used for the AWES wing is purely theoretical and simplified. However, this gives a

ballpark view of the size and infrastructure required. The 22 m wingspan resultant from the calculation is close to the Makani M600 prototype with 26 m wingspan [9]; the difference is that it is rated at 600 kW, less than 10% of the estimated theoretical power for its size. The significant power losses show the impact of the highly idealized assumptions made by Loyd in the first place, a few of them being the tether drag and weight losses, the flight angle, the kite mass, etc. This, however, has not stopped start-up companies from constantly developing AWES technology. The number of institutions working on AWES is rapidly increasing from just a handful in 2000 to over 50 in 2013 [10]. It is a growing industry that has a general goal of transitioning from fossil fuels to renewable energy. Through Loyd's power equation this technology promise great potential. However, the highly idealized power calculations have been put to the test through more realistic models that even though they will never achieve such power numbers, continue to convince us that AWES is worth pursuing.

Another reason why we should invest in developing AWES it the high-altitude wind resource. The wind power density can reach averages of over 10 KW/m^2 in the jetstream at 10,000 m [6], harnessing this power would provide more electricity than what our entire civilization demands [11]. It seems unrealistic that any generation technology can reach these altitudes due to the structural challenge involved, therefore a study that only considers the wind resource in the first 1000 m suggests that the optimal operational altitude for AWES is around 150 - 500 m [12], where a single AWES device has the flexibility to operate in a range of altitudes allowing to search for these optimal operation conditions.

1.2 Classification of Airborne Wind Energy Systems

In overview, AWES harness the power of high altitude winds using aloft tethered devices. There is a continuous discussion around which type of AWES will set the standards and drive the industry into commercialization and grid integration, and companies are pushing their designs and strategies to set the pace to win the high altitude generation race. A comprehensive review of technologies summarizes the crosswind generation approach as drag and lift mode; the latter also called pumping mode, as well as non-crosswind technologies such as lighter-than-air aerostats and static suspension quadrotors [13].

1.2.1 Generation approach

Crosswind drag mode generation shown in Figure 1.1.a produces electricity onboard with specially designed rotors that can operate as both small-scale wind turbines, and propellers to occasionally provide thrust and sustain crosswind flight. The electricity is then sent to the ground through a conductive tether.

Lift or pumping mode crosswind generation shown in Figure 1.1.b produces the electricity on the ground by transmitting the aerodynamic forces generated on the plane thought high tension cables to a motor-generator-winch system; the generator is driven by the winch reeling-out motion produced from the plane's pull. Once the tether reaches its limit the system requires to spend energy reeling-in the plane and re-starting the cycle, this approach aims to maximize the power generation during the reel-out phase while minimizing the power consumption during the reel-in phase.

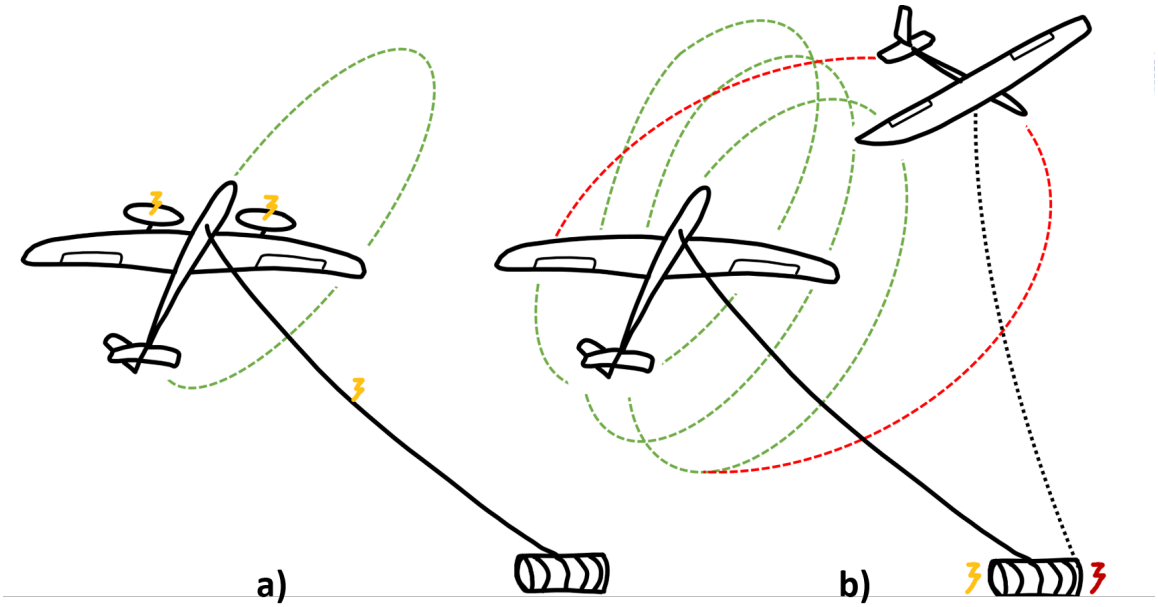

Figure 1.1: Drag mode (a) and lift mode (b)

Non-crosswind technologies as the aerostats filled with lighter-than-air gas contain a wind turbine in the center enabling them to operate at higher altitudes. Another concept is the use of static suspension quadrotors that placed at a specific angle can generate power and provide enough thrust with the rotors to maintain the device airborne. These concepts don't take advantage of the high aerodynamic lift generated by the apparent wind speed during crosswind flight, and therefore will not be studied throughout this thesis.

1.2.2 Wing shape: planes vs kites

Crosswind AWES can either be rigid-wing planes, soft-kites, or a combination of both. For simplicity's sake, throughout this thesis, we refer to any crosswind flying device as a plane unless otherwise explicitly mentioned. The reason research groups and companies use soft-kites is because of the relatively low initial investment required to develop a prototype; soft kites can be easily acquired from the kite-surfing industry and can be quickly set-up and placed in the air. The disadvantages of soft kites are that they are hard to model structurally, have low aerodynamic efficiency, and are difficult to autonomously take-off and land. On the other hand, rigid wing planes are specially designed for crosswind flight which makes them more expensive and take more time to manufacture; they are structurally resilient and generally have a good aerodynamic performance making them the best option for using in flight models. However, AWES in the early developing phases are prone to crashes, and replacing a plane is significantly more expensive than a soft-kite which can be easily switched for a new off-the-shelf model.

1.2.3 Take-off and landing strategy

One of the main challenges of AWES is the take-off and landing strategy; same as with the generation approach, there is a debate between what is the most efficient way to get the plane from its parked position to the generation mode and back. The benefits and disadvantages of the most common approaches are studied in [14], which are currently being implemented by research groups and companies.

Vertical take-off and landing (VTOL) as in quad-copters widely available in the market, use their onboard propellers to vertically climb and hover into position. This process is the most demanding approach in terms of energy consumption and additional onboard equipment for larger-scale devices. However, the benefit is that the take-off and landing area can virtually be the size of the plane itself; it does not require a minimum airspeed to sustain flight as the vertically-facing motors provide enough thrust to propel the plane in the desired direction. VTOL simplifies the winch operation during this phase allowing for a controlled reel-in and out speeds with low tension forces. With the growing interest in the hobbyist and commercial drone industry more advanced flight controllers are constantly being developed making devices with VTOL capabilities to fly effortlessly. This approach is currently being implemented by the Makani M600 prototype with a tail-sitter type configuration where

the propellers are aligned with the flight direction. The M600 uses the propellers for VTOL and also for onboard power generation. On the other hand, Twingtec and Kitemill rigid-wing prototypes have a configuration that resembles a combination of a quadcopter and a plane, where the vertically-facing propellers are perpendicular to the direction of flight and are exclusively used for taking-off and landing.

Linear take-off and landing (LTOL) is the most commonly-known approach for airplanes, it requires a sufficiently long runway and enough forward propulsion to reach the minimum airspeed that generates the lift required to sustain the plane flight. For AWES, having onboard propellers is highly inefficient due to the weight and aerodynamic losses. Therefore companies and research groups have developed systems that change the take-off power equipment from the plane to the ground station as a winch system assist resembling an aircraft carrier catapult, minimizing the onboard propulsion equipment and runway length. The trade-off is that the ground station is over-dimensioned concerning the energy generation capacity due to the large torque required to get the plane to its minimum flight speed in a short distance. This approach results in a less power demanding systems than the VTOL and it is most likely to be implemented in devices with pumping mode generation to take advantage of the already installed power equipment on the ground. The Dutch company Ampyx Power has embraced this approach since its earliest prototypes, and is currently in the development of a 4 MW device that will operate in an off-shore platform.

Rotational take-off and landing (RTOL) approach uses a rotating platform to generate enough airspeed on the plane, initially attached to the rotating arm, and then slowly reeled-out when enough aerodynamic forces are produced, reverting the process for landing. The benefit of this strategy is that the rotating ground station requires a relatively low power compared to the previous VTOL and LTOL approaches. Also, the kite does not require any onboard propulsion and therefore no additional mass. However, to achieve the take-off speeds, the rotating arm must have a significantly long length mainly because the aerodynamic forces must overcome the centrifugal force, therefore increasing the required available area to operate. Another challenge is the difference of apparent wind speed acting on the kite during the take-off and landing phase; it can have a variation of $\pm$ the wind speed with each half rotation of the ground station. All of the previous challenges did not stop the Dutch company Enerkite to develop a mobile 30 KW research and development prototype, with over 100 hours of operation time with RTOL approach using a crane mounted

on a truck.

1.2.4 Flight control strategies

AWES kites or planes are able to be stay airborne due to their advanced flight control and seamless integration with the ground station through different tether configurations. Single tether AWES control most of the flight using onboard actuators such as motors and control surfaces (aileron, elevator, and rudder); as a conventional plane, the ground station is then controlled separately to reel out the tether depending on the plane's position and demanded torque. Rigid-wing planes such as the Ampyx and Kitemill prototypes implement this approach. Also, drag mode AWES such as the Makani prototypes that require a conductive tether use single tether as it becomes increasingly wider and heavier depending on the rated current that it must withstand.

Soft-kites in general require two lines to control their direction during crosswind flight, a length difference in the lines causes the kite to roll towards the side with the smaller length. This can be either performed at the ground station by having two independent reeling motors, or by having one line attached to a control pod located just below the kite, that then attaches to either side of the kite [15]. The latter approach seen in the Kitepower prototype reduces the tether aerodynamic drag as the total cross section area of the tether is significantly reduced from two long lines to one long and two short lines. All lines in this approach are used for harnessing the traction force generated by the kite.

Semi-rigid planes also implement a combination of control surface with double line control. The Twingtec prototype controls the navigation of the plane using a two line approach, while the pitch is controlled onboard with the implementation of an elevator [16].

Three line kites have also been developed such as the Enerkite EK30 prototype [17], and the research platform developed at the University of California [18]. The two lines attached to both ends of the wings control the navigation direction, while the center line controls the pitch angle and therefore handles the traction forces generated by the kite.

1.3 Crosswind generation technologies

Currently, AWES companies are at the stage of testing multi-kilowatt scale prototypes and pushing forward to develop megawatt-scale concept designs. This section presents a general overview of the latest development of the leading companies in the AWES industry.

The largest AWES prototype built is by the American company **Makani** [9], the M600 in Figure 1.2.a has a rated power of 600KW and a wingspan of 26 m. This device is currently being tested off the coast of Norway in partnership with Shell [19]. This recent partnership has all the AWES players paying close attention because it might just be the push that the industry requires to be introduced into the global energy system.

Another big company is the Dutch-based **Ampyx Power** [20], which intends to finish its 300KW prototype seen in Figure 1.2.b by mid-2021, and continue scaling-up to the AP4 4 MW prototype intended to be finished by 2030. Ampyx makes emphasis on the rigorousness of their manufacturing process as they plan to certify the technology under the Federal Aviation Administration (FAA) regulations instead of under the wind turbine certifications, setting a baseline for the following companies that want to enter the industry.

Kitemill is a growing Norwegian company [21] that is currently testing its largest 7.5 m fixed-wing prototype with 30KW rated power shown in Figure 1.2.c. The device aims to generate electricity using the pumping mode approach while having VTOL capabilities. Some of their developments and innovations include a ground-fixed testing platform where the plane can be secured to a rotating arm that will simulate the circular flight. This was intended to be used for calibrating the sensors such as GPS, accelerometers, and pitot tubes.

On the soft-kite side of the industry, **Kite Power** in Figure 1.2.d developed a mobile 100 KW nominal power system that is all contained in a container-size ground station [22]. It uses a soft kite that is flown by a control pod mounted on the tether bridle. The system aims for diesel dependency displacement, which means that it can be easily transported and deployed in remote locations.

Twingtec is a Switz company that also provides a solution for remote sites [23]. Their 100 KW rigid-wing concept prototype in Figure 1.2.e is able to fit inside a shipping container and be transported and deployed wherever is required. Same as the Kitemill device, the TT100 has VTOL capabilities and uses the pumping mode

for energy generation.

Enerkite is a German company that uses a combination of soft and rigid delta-wing kite [24]. It's the only company that is currently pursuing the rotational take-off, and it's been done on top of a transport vehicle seen in Figure 1.2.f. This allows portability and facilitates the deployment and testing, considering that the rotating arm requires a larger area to operate than VTOL systems. The EK30 is rated to 30 KW and it's currently being tested as a pumping mode generation AWES.

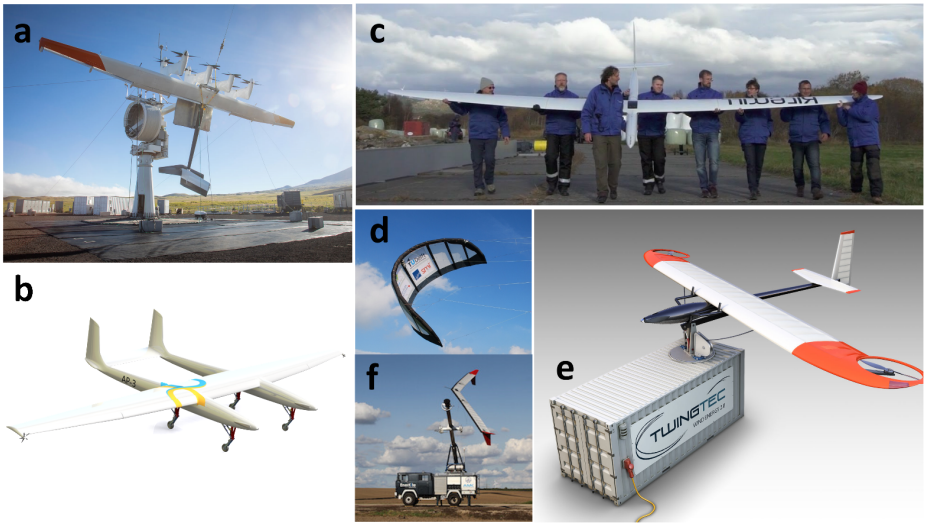

Figure 1.2: Recent prototype development (a) Makani M600, (b) Ampyx AP4, (c) Kitemill prototype, (d) Kitepower 100 KW soft-kite, (e) Twingtec TT100 concept, and (f) Enerkite EK30.

.

1.4 Lab-scale initial development

All of the above companies had to start somewhere before jumping into the development of multi-kilowatt scale devices. A few early AWES adopters started developing soft-kites and lab-scale fixed-wing planes to validate flight models, controls, and obtain first-hand practical experience in getting their devices from the computer models into the air. Makani started with soft-kites to then move to a 5.5 m wingspan prototype shown in Figure 1.3.a. Ampyx also started with a smaller prototype shown in Figure 1.3.b of 5.5 m wingspan that is still being used today for testing flight models. Kitemill and Twingtec shown in Figures 1.3.c and 1.3.d respectively, developed a small-scale device that can perform VTOL and then transition into power generation

mode. Before Enerkite built it's mobile RTOL platform there was a small-scale rotational take-off platform shown in Figure 1.3.e developed at KU Leuven [25]. Finally, there are other research groups and institutes that have developed their systems and collaborated with the companies mentioned above, one of them is the project at ABB corporate research [26] shown in Figure 1.3.f that has a winch assisted horizontal take-off now implemented in the Ampyx prototypes.

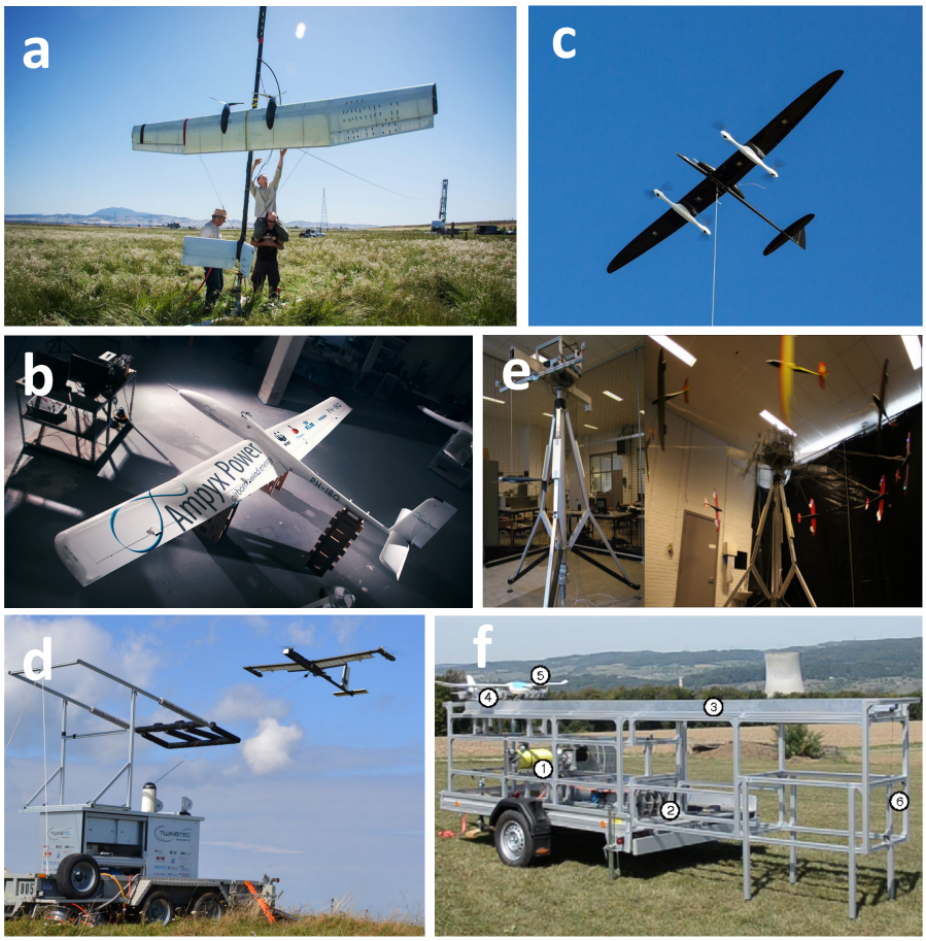

Figure 1.3: Initial prototype development (a) Makani, (b) Ampyx, (c) Kitemill, (d) Twingtec, (e) KU Leuven, and (f) ABB corporate research.

A recent lab-scale AWES project called AWEsome [27] implemented the open-source autopilot platform `Ardupilot` [28] into their structurally enhanced model plane to achieve autonomous tethered flight. The AWEsome project achieved autonomous tethered flight but the take-off and landing were performed manually. Also, the tether was reeled manually with fishing equipment. The goal of the project was to provide an inexpensive alternative for research groups and start-up companies to develop a

AWES testing platform and provide invaluable experience in first-time flight testing. Although this tool provides a robust AWES flight operation, it left untapped a few key challenges such as pumping mode flight paths, winch control, and autonomous take-off and landing, which became the main driver of this master's thesis.

1.5 Motivation and contribution

This thesis builds up from the development of a AWES flight model, to the implementation of an open-source autopilot for simulating AWES flights, to finally the development and testing of a lab-scale demonstrator platform. The main motivation of this project is to provide an AWES platform that allows preliminary flight data acquisition, real-world insights, and flight testing experience in AWES operation.

- The quadplane, a hybrid aircraft between fixed-wing and quadcopter, is considered for the development of the testing platform . Implementing the `Ardupilot` open-source flight code and the quadplane airframe, the entire AWES operation is conveniently automated.

- The detailed plane and ground station building process is described, providing the list of materials, wiring directions, and encountered challenges, to provide future groups an advantage in developing their systems and promptly advance into flight testing.

- A simple 3 degree-of-freedom (DOF) flight model is developed from scratch to provide a general tool for controller tuning, load estimation, and evaluation of trajectory tracking. Trajectories evaluated with this model could be further implemented in real flights using open-source software and hardware.

- The `Ardupilot` open-source platform is implemented with the goal of having an actual controller that can fly the plane. The physics model is modified to account for tethered flight and power generation. The platform provides a simulation tool to tune the controllers and flight paths based on the developed hardware. The autopilot automates the entire operation as the take-off and landing phase is simplified through the incorporation of VTOL approach.

- The process to operate the platform must follow local and national aerospace rules and regulations. Therefore, the legal requirements, documents, and certi-

fications are provided with the goal of establishing a plan of action for further tests.

1.6 Thesis Outline

This work presented in this thesis is separated into the following chapters.

Chapter 2 provides an overview of the developed lab-scale AWES demonstrator. It also presents a detailed description of the hardware building process, including the integration of a quadcopter frame to a fixed-wing plane to allow Vertical take-off and landing (VTOL), wing reinforcement for tethered flight, integration of the autopilot components, and characterization of the airframe. Lastly, the development and specifications of a portable ground station (GS) is described.

Chapter 3 presents the development of an AWES model for trajectory tracking. The simulation provides insight on the plane's performance and allows evaluating the tension and power generated in pumping mode flight. Different trajectories, such as a circle and figure-8 with constant and variable tether length, are simulated to evaluate the performance of the navigation and reeling speed controller. Also, the model is set to follow optimized trajectories that maximize the pumping cycle power generation, to further assess the viability of implementing these trajectories with an actual flight controller.

Chapter 4 implements an open-source autopilot platform for AWES simulation. An overview of the platform architecture and control strategy is presented. The physics model of the system is modified to account for tether drag, weight, and tension forces. Flight trajectories, as evaluated in Chapter 3, are used for assessing the flight controller performance. The `Arduplane` parameters obtained in the simulation are then considered for the actual flight controller. Lastly, AWES simulations assess the theoretical power production, from either pumping or drag mode generation.

Chapter 5 presents the incremental flight test campaign. Each test gradually increases its complexity with the objectives of: safely gain flight testing experience, tuning the flight controllers, validate and adapt the model developed in Chapter 4, obtaining preliminary data and results, identifying the limitations of the system, and expanding the capabilities of the platform. Ultimately, having the goal of a fully functional platform that is able to perform autonomous crosswind flights.

Chapter 6 summarizes and provides conclusions on the work performed in each Chapter. It presents the key aspects and challenges encountered, and provides direc-

tion for further work that could be performed in the models and hardware implementation.

Chapter 2

Hardware development of an Airborne Wind Energy System with open-source autopilot platform

2.1 Introduction

Prototype development is essential for validating the models, gaining technical experience, and even get further funding to continue developing the technology. Companies like Makani started building their first rigid-wing AWES prototype in 2010; upgrading from soft wing kites in 2008 for better aerodynamic efficiency and control, it was when the device generated electricity for the first time. Since then, the company has grown and scaled its first 10 KW device to a 26 m wing and 600 KW rated power kite that is being tested in an off-shore platform [9]. Once a prototype is operational it can be used for proof of concept and as a testing platform for improving the system. Ampyx Power is a great example of the use of their prototype to push forward the learning experience and develop scaled-up devices. The AP2 is constantly being tested with the software and controls of the pre-commercial demonstrator AP3 [20] so that when the next device is assembled, the flight control will already have been tested in similar equipment.

This chapter describes the hardware development and integration to create a lab-scale AWES platform. A fixed-wing plane model is structurally enhanced for tethered

flight and adapted with a quadcopter frame enabling autonomous vertical take-off and landing. Also, a compact and portable ground station was developed to control the reeling operation of the system. Moreover, this chapter will serve as guidelines for developing the entire hardware of the system, providing component description and integration aiming to give future students or research groups the opportunity to quickly build a similar system and accelerate the process into the flight testing phase.

2.1.1 Motivation

The work performed in the AWES lab-scale prototype was driven by the initial development of the AWEsome project [27], which provided an inexpensive, open-source platform for testing AWES. The project concluded with successful autonomous flights of a tethered radio-controlled (RC) model plane in a fixed length figure-8 trajectory. The take-off and landing were performed manually by a pilot, and the tether management was also manually controlled. This project aims to fully automate the system's operation by defining the following objectives.

- Develop a plane suitable for tethered flight that allows the evaluation of the `Ardupilot` open-source code for AWES operation. This includes the structural reinforcement and integration of the autopilot components.
- Enable autonomous Vertical take-off and landing (VTOL) by upgrading the fixed-wing plane model with a quadcopter frame.
- Obtain the quadplane main operating specifications for further parameter definition in the `Ardupilot` flight code.
- Develop a ground station for tether management and load assessment. Performed in collaboration with 4th year mechanical engineering students, through senior year courses part of the program requirements.

2.2 Development of a Quadplane for Airborne Wind Energy operation

2.2.1 Quadplane

Start and shut-off of AWES operation requires the aircraft to take-off and land. These phases are studied separately due to that they present a challenge of their own. The take-off and landing strategies presented in Chapter 1 have particular benefits at different scales. VTOL is the most power consuming approach [14]. However, at small scale, VTOL becomes beneficial as electric motors are more economic, efficient, and provide a higher thrust to weight ratios. Quadcopters are widely implemented in different industries, consequently benefiting from their advancements in flight control. Furthermore, quadplanes reduce the required deployment area while still allowing to cover large distances by operating as a conventional plane in forward flight. They are increasingly implemented for various purposes, including terrain surveillance, search and rescue, and package drops.

A fixed-wing glider and a quadrotor frame were merged into a fixed-wing plane with VTOL capabilities, namely a quadplane. The Phoenix V2 glider from Volantex has 2-meter wingspan and a structural weight of 1.2 kg, it comes with built-in control surfaces such as ailerons, elevator, and rudder, and with the option to enable flaps, convenient to increase the lift coefficient while landing and crosswind flight. The fuselage provides enough space to incorporate the additional autopilot hardware and power electronics. Figure 2.1 shows the model plane and the autopilot hardware. The quadrotor frame is designed to mount four brushless motors that combined provide over 8 kg of thrust for a total quadplane weight of 3.5kg, sufficient to vertically lift the plane with the attached tether and sustain hover flight until the transition into fixed-wing flight. The general specifications of the quadplane are presented in Table 2.1.

Table 2.1: General specifications of the quadplane.

Wing area (m^2)	Wingspan (m)	Chord (m)	Weight (kg)
0.36	2	0.18	3.5

Figure 2.1: Volatex Phoenix V2 model RC plane and autopilot hardware

Wing reinforcement

The wings of the model plane are made out of high-density Styrofoam with a 10 mm aluminum square beam as a wing spar. The high aerodynamic loads estimated to be generated during crosswind flight require a more robust structure, therefore the aluminum beam was changed for two 16 mm carbon fiber tubes as shown in Figure 2.2. The tubes pass through the fuselage and are fitted 60 cm inside of each Styrofoam wings, providing additional structural support and allowing a mounting point for the quadframe. The additional 40 cm from the end of the carbon tubes to the wing tip has a built-in square tube, which is used to slide in a carbon fiber rod into the end of one of the wing spar tubes providing additional structural support throughout the entire wing. Moreover, two tether sections are secured to the wing spar aligned with the center of gravity (CG), both lines go around the fuselage internal core and meet at the bottom of the plane joined together by a swivel mechanism. The swivel component was selected to be the weakest link in the tether with a maximum load

of 70 lb. When the plane experience a traction load over 331 N, the swivel ring will break and leave the plane in free flight preventing any damage to the plane or GS structure.

Figure 2.2: Carbon fiber wing spars

Quadcopter frame integration

The integration of the quadcopter frame with the fixed-wing plane was made through the double wing spars. Two carbon fiber tubes parallel to the fuselage, or booms, are mounted at the end of the carbon fiber wing spars. The quadcopter motors are then mounted at both ends of the booms. The entire frame is set up in a way that its center of gravity matches the plane suggested aerodynamic CG, which is located about 1/3 of the wind chord from the leading edge. Even though the quadcopter structure is built as an "H" shape, its geometry consists in an `Ardupilot` "X" type frame, meaning that the perpendicular distance from each motor to the center of gravity is equal. The plane wings have a fixed angle of approximately 3° between the chord line and the fuselage horizontal plane. Therefore the quadcopter booms are mounted to the wing spars with an inclined angle in order to make the frame parallel

to the fuselage horizontal axis, allowing positive angles of attack while transitioning from hovering to forward flight.

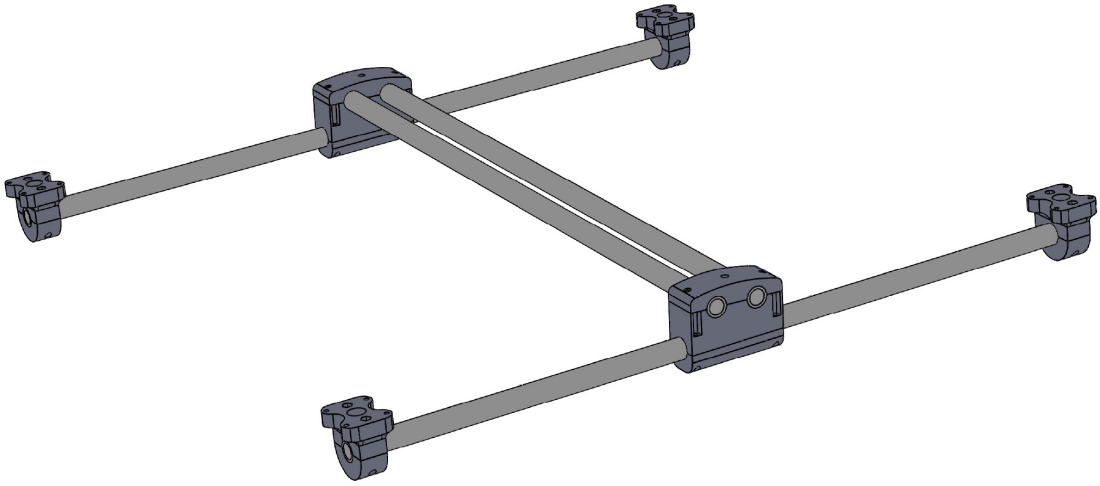

Figure 2.3: Quadcopter frame view

The motor mounts and boom mounts are 3D printed pieces designed with the motor and tube dimensions. The motor mount is a two-piece clamp secured around the boom with two bolts, mounting the motor with four bolts to the top part. The boom mounts connect the booms with the two wing spars with a 90° angle. It consists of a three-piece assembly where the middle part contains embedded nuts where the top and bottom clamps are secured with bolts. The top clamp has a curvature similar to the wing airfoil to reduce the aerodynamic drag. A detailed design of these parts is presented in Appendix D and a CAD model of the frame is presented in Figure 2.3. The booms must extend far enough to allow the motor to be mounted where the propeller wash does not interfere with the wing, resulting in a square frame geometry of 600x600 mm.

The VTOL motors selected initially based on a thrust to weight ratio value of 2, had the rated capacity to lift and hover the quadplane. However, in practice the hover throttle was above 50% and the motors overheated during operation. As a result, more powerful motors were selected with the goal of reducing the hover throttle under 50% and therefore have mote lifting capacity. The quadcopter frame and motor mounts had to be iterated to withstand the additional loads and torque generated by the new motors. For future design efforts, it is recommended to follow the aircraft design procedure for VTOL airplanes to appropriately select the propulsion

and energy storage systems. The final build of the quadplane is presented on Figure 2.5

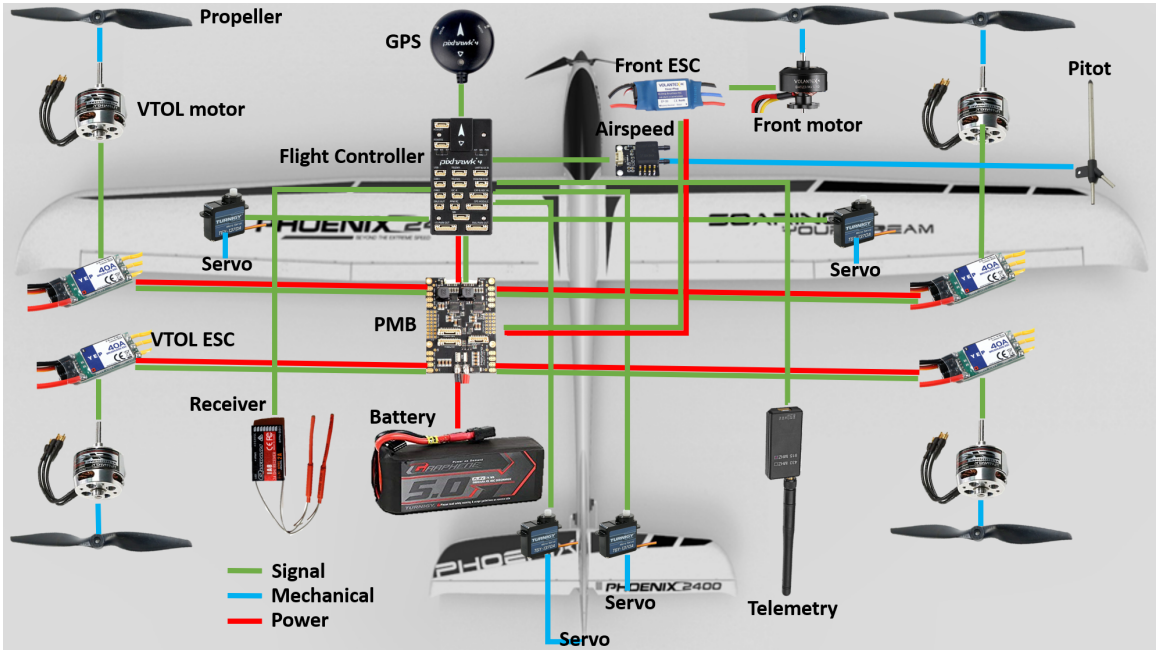

Figure 2.4: Quadplane connections diagram

`Ardupilot` hardware

The autopilot hardware such as the flight controller, sensors and power components are fitted inside the fuselage in agreement with the CG. The wires feeding the current to the motors are passed thought a covered groove on the wing to reduce their aerodynamic drag. The internal arrangement places the flight controller board as close as possible to the CG to better account for the rotational rates. The GPS module has to be placed at least 4 in away from any power components to prevent magnetic interference. In addition, the airspeed pitot tube is mounted at approximately 3/4 wing length facing forward and outside any of the propeller wash. The tubes that carry the differential pressure are passed through a groove on the wing and into the fuselage where the airspeed sensor is located.

The navigation and attitude of the plane can be either controlled manually or autonomously, in both cases the servos and motor commands are given by the Pixhawk 4 flight controller based on the desired state. The Pixhawk records information such as linear and rotational accelerations while collecting the position, airspeed, telemetry,

Figure 2.5: Quadplane final build

and radio commands from their respective sensors. Through a series of controller logic expanded in Chapter 4 and the desired reference state, the Pixhawk will send the signal to either surface servos in fixed-wing mode or motors in quadcopter mode. The entire vehicle is powered by a 4 cell (14.7 V) lithium-polymer battery with 5000 mAh capacity and 45C rating. The power is distributed to the flight controller, motors, and servos through a power management board (PMB). In addition, each motor contains an Electronic Speed Controller (ESC) which converts the flight controller signal into pulse width modulation (PWM) commands and outputs a rotational speed. The autopilot component diagram is shown in Figure 2.4, and the description along with their connections are presented in Table 2.3.

Pre-flight checks

Before each flight, the pilot and crew must ensure the correct operation of the motor and servos. The motor ordering and rotation direction must follow the diagram in Figure 2.6. Wrong ordering or rotation will cause the quadplane to flip at take-off or magnify the wrong angle command. Table 2.2 provides a summary of the manual and stabilized response of the plane to pilots command and external disturbances.

The motor rotation can be visually assessed by arming the vehicle with no propeller, the rotation can be inverted by switching any two of the three wires coming

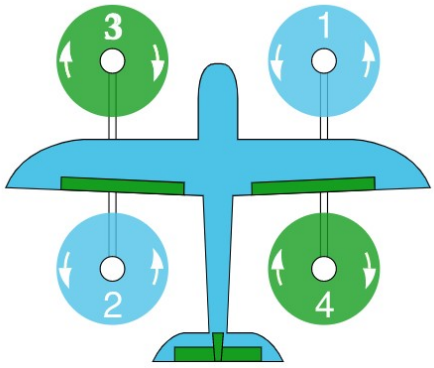

Figure 2.6: Motor ordering and rotation direction diagram

from the ESC to the motor. The motor ordering can be checked by manually rotating the armed quadplane in a stabilize mode, pitching the nose down will cause the front motors to spin faster, and rolling the plane to the right will cause the right motors to spin faster. A similar process must be verified for the fixed-wing servos. RC transmitter commands should move the servo in the right direction. A roll command to the right should lower the left aileron and lift the right aileron, a pitch-up command should lift the elevator, and a yaw right should move the rudder to the right. Moreover, the autonomous control of the servos is verified by rotating the plane along the pitch and roll axis during a stabilized mode. The autopilot aims to balance the plane, therefore manually rolling the plane to the right should generate a left roll command; moving the right aileron down, pitching the plane nose down should move the elevator up countering the dive with a pitch up command. This verification process is part of the pre-flight checks, a step-by-step checklist can be found in Appendix B.

Table 2.2: Motor and servo response to manual commands and stabilized disturbance

Manual mode	Command	VTOL response	Fixed-wing response
Roll	Stick Right	Left motors spin faster	Left aileron down, right aileron up
	Stick Left	Right motors spin faster	Left aileron up, right aileron down
Pitch	Stick Forward	Back motors spin faster	Elevator down
	Stick Back	Front motors spin faster	Elevator up
Yaw	Stick Right	M2 M4 spin slower	Rudder right
	Stick Left	M1 M3 spin slower	Rudder left
Stabilized mode	Disturbance	VTOL response	Fixed-wing response
Roll	Rotate right	Right motors spin faster	Left aileron up, right aileron down
	Rotate left	Left motors spin faster	Left aileron down, right aileron up
Pitch	Rotate forward	Front motors spin faster	Elevator up
	Rotate back	Back motors spin faster	Elevator down

Table 2.3: Autopilot components description and connection

Component	**Description**	**Connection In (receiving)**	**Connection Out (sending)**
Aileron Servo	Controls roll in forward flight	PMB/ Main1	
Elevator Servo	Controls pitch in forward flight	PMB/ Main2	
Rudder Servo	Controls yaw in forward flight	PMB/ Main4	
Plane Motor	Provides forward thrust	Plane motor ESC	
Plane Motor ESC	Controls the forward motor speed	PMB/ Main3	Plane Motor
Quadcopter Motor	Provides vertical thrust and controls pitch, roll, and yaw in VTOL mode	Quadcopter Motor ESC	
Quadcopter Motor ESC	Controls the vertical motor speed	PMB/MAIN 5-8	Quadcopter Motor 1-4
Pixhawk FC	Controls the plane flight	PMB/Power 1	Telem1 IC2 PPM RC GPS Module I/O PWM OUT FMU PWM OUT Micro SD
PMB	Distributes the flight controller signal outputs and receives the main power supply from the battery	Battery I/O PWM IN FMU PWM IN	FMU PWM OUT/ Aileron, Elevator, Rudder. FMU PWM OUT/ Plane motor ESC. I/O PWM OUT/ Quadcopter motor ESC 1-4
Telemetry	Transmits the plane's live data	Pixhawk/ Telem1	
GPS/Compass Module	Measures position and orientation	Pixhawk/ GPS Module	
RC Receiver	Receives transmitter commands	Pixhawk/ PPM RC	
Airspeed Sensor	Measures the airspeed	Pixhawk/ IC2	
Battery	Provides the plane power		PDB
Micro SD card	Logs the flight data	Pixhawk/ SD port	

2.2.2 Quadplane performance

The `Ardupilot` provides information about the vehicle performance to the flight controller through a list of parameters described in Chapter 4. The key parameters for a stable flight are the plane's operational speeds along with the trim and hover throttle. By setting these parameters, the flight controller can know the limitations of the vehicle and plan the autonomous commands accordingly, therefore it is of high importance to estimate these values as accurately as possible. There are two possible approaches for getting the required parameters. First is through experimental testing. The quadplane must be manually flown by an experienced pilot, who performs a series of maneuvers that allow the flight controller to record the pilot's commands and the plane response, logging data files that are later analyzed to obtain the plane's flight parameters. A second and more conservative approach involves calculating these values from the physics of the plane. The hover throttle can be estimated with the total weight and the trim conditions with the aerodynamic forces.

Performing a force balance on the plane during forward flight or hovering, as in Figure 2.7, allows estimating the key characteristics of the quadplane. The fixed-wing flight is sustained by the lift force generated by the wing airfoil, while during VTOL and hovering it's directly sustained by the vertical motors.

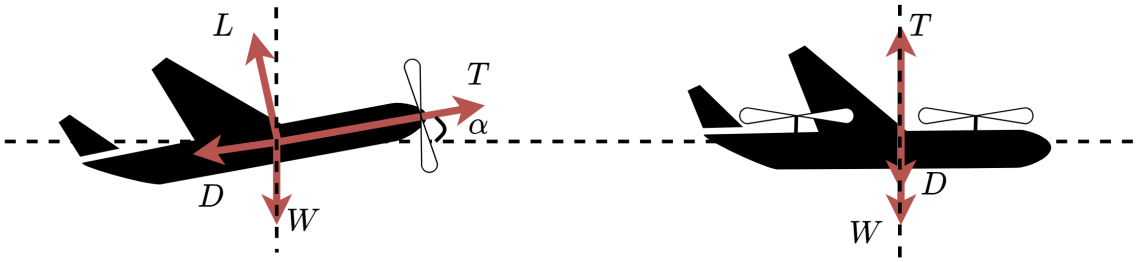

Figure 2.7: Quadplane forces as fixed-wing and quadcopter

Rigid-wing flight specifications

The total lift and drag coefficients of the RC plane were obtained as part of an undergraduate honors project [29]. The wing dimensions were obtained from scanning sections of the plane, used as input to the lifting line solver for low Reynolds number XFLR5 [30]. The aerodynamic coefficients were calculated for a range of flight speeds between 1-25 m/s and angles of attack between -15 to 15 presented in Figure 2.8.

The scanned airfoil resembles a low Reynolds airfoil, with a maximum lift coefficient of $C_{L,max} = 1.33$, and minimum drag coefficient of $C_{D,min} = 0.011$.

Loyd's power equation includes the C_L^3/C_D^2 ratio. Maximizing the power output using Equation 1.1 the optimal angle of attack for the evaluated speeds is obtained with the aerodynamic coefficient ratio. For this particular airfoil, not designed for AWES power generation, the optimal α gradually decreases as the plane flies faster.

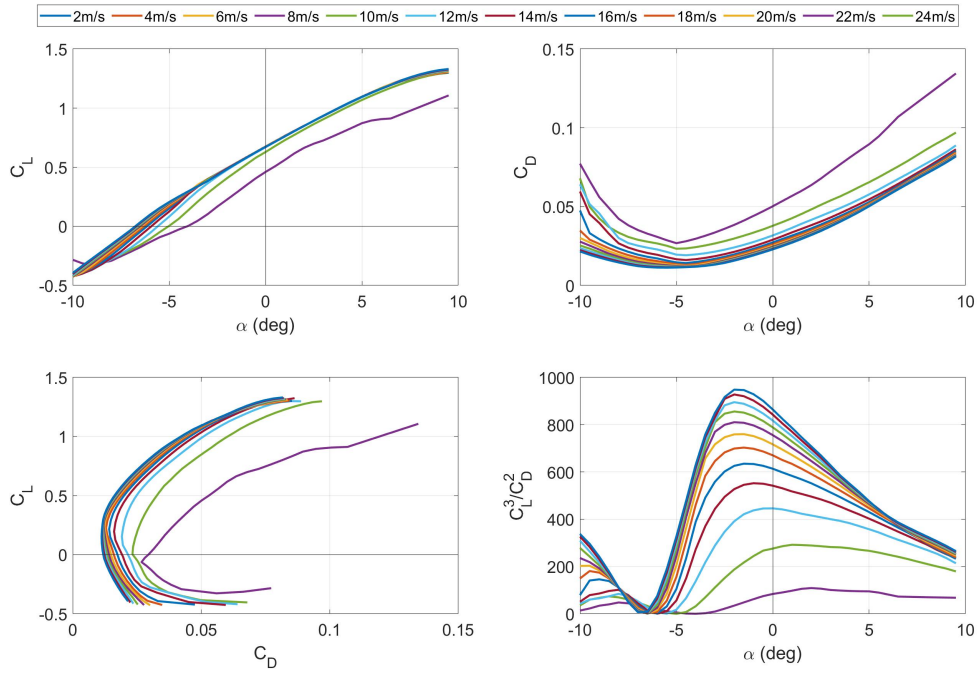

Figure 2.8: Aerodynamic lift and drag of fixed wing plane plane for different flight speeds

The plane flight characteristics, such as trim speed and cruise time, can be estimated using the results from the aerodynamic analysis. The forces acting on the plane during trim flight are shown in Figure 2.7, where L and D are the aerodynamic lift and drag respectively, T is the thrust, and W is the plane weight. Performing a balance of forces in the X and Y direction Equations 2.1 and 2.2 are obtained.

$$\sum F_x = 0 \implies T\cos(\alpha) = \frac{1}{2}\rho A V_a^2 C_L \sin(\alpha) + \frac{1}{2}\rho A V_a^2 C_D \cos(\alpha) \tag{2.1}$$

$$\sum F_y = 0 \implies \frac{1}{2}\rho A V_a^2 C_L \cos(\alpha) + T\sin(\alpha) = W + \frac{1}{2}\rho A V_a^2 C_D \sin(\alpha) \tag{2.2}$$

A $15m/s$ trim speed at zero angle of attack is directly calculated from Equation 2.2, where the lift is equal to the plane weight. To maintain this speed the front motor must provide enough thrust to overcome the aerodynamic drag generated by the wing, fuselage, and the quadcopter frame components. The drag coefficient of the quadcopter components are assumed from common geometries: the VTOL motors as cylinders, the mounts as cubes, and fuselage as a streamlined body. The thrust from Equation 2.1 is then converted to throttle knowing the maximum thrust the forward motor can produce, resulting in a trim throttle of around 40%, and a maximum speed of 25 m/s with zero angle of attack for maximum motor thrust.

The stall speed can be obtained by solving for the speed V_a and thrust T in Equations 2.1 and 2.2 for a range of angles of attack. Figure 2.9 summarizes the performance of the quadplane in fixed-wing flight where the minimum speed of approximately 11 m/s corresponds to the stall speed, which requires an angle of attack of 10° and over 90% throttle.

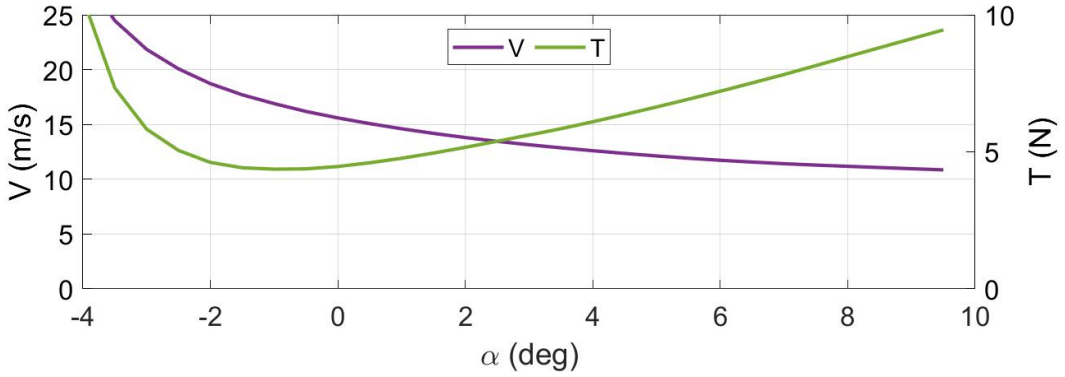

Figure 2.9: Speeds and thrust for range of angle of attack

The plane cruise time is estimated with the trim throttle, the current drawn from the motor allows calculating the battery discharge time. Estimating a continuous current of $15A$, the $5000mAh$ battery capacity is consumed in 20 minutes. This time, however, does not consider the power consumed during take-off and landing, which is presented in the following section.

Quadcopter flight specifications

During quadcopter operation, maintaining constant altitude requires that the hover thrust must be equal to the plane's weight. With a total weight of 3.5 kg, the hover thrust results in 34.3 N corresponding to approximately 40% throttle. Each

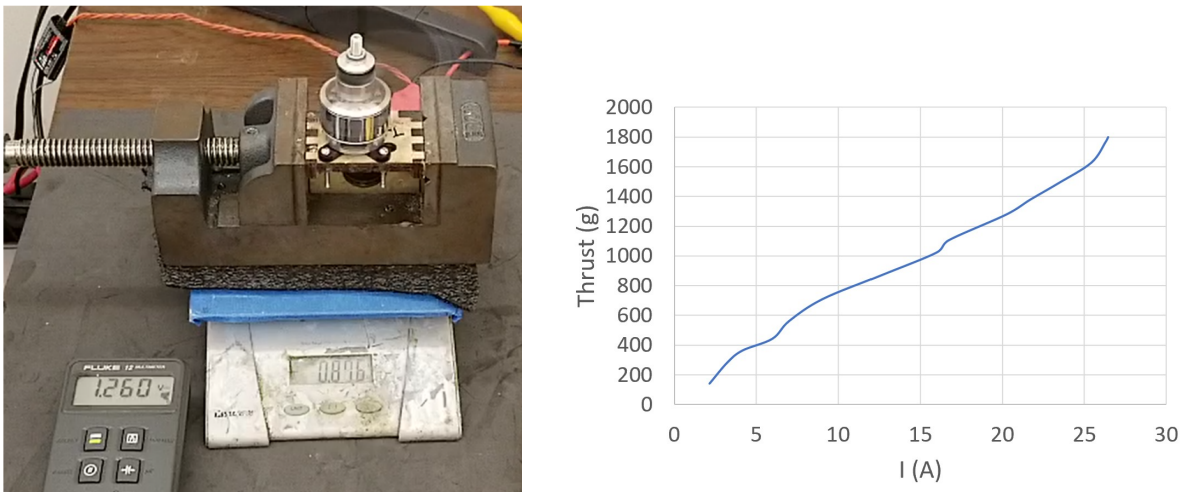

(a) (b)

Figure 2.10: Experimental setup (a) and results (b) for motor thrust bench test.

motor must provide $875g$ of thrust to maintain hover, the current drawn can be estimated using the motor power curve, which is not provided by the manufacturer. Therefore, bench tests were conducted to obtain the thrust and current curve. The test set-up shown in Figure 2.10.a consists of mounting the motor on a scale in a way that the effect of the propeller wash on the weight measurement is minimized. The throttle is increased manually while the weight, current, and voltage are recorded. The current was measured using a current/voltage converter with an appreciation of 100mV/A, whereas the voltage was directly measured from the battery. From Figure 2.10.a, the current is calculated to 12.6 A for 876 g of thrust. The throttle range implemented allowed to generate the curve presented in Figure 2.10.b. Finally, a continuous discharge current from the four motors is 50.4 A which allows a maximum discharge time of 6 minutes using a battery with $5000mAh$ capacity.

Vertical climb generates a downward drag force from the wing, tail, fuselage, and quadcopter components. Providing a maximum thrust with the VTOL motors, the maximum climb speed results in 10 m/s, requiring to operate the motors at the current limit, overheating the ESC, producing high loads on the structure, and significantly reducing the flight time. Therefore, more conservative climbing speed of approximately $3m/s$ is achieved by applying 50% throttle; 10% above the hover throttle. Descent speed is calculated similarly, if the thrust is off, the drag of the wing will slow down the fall. On the other hand, a controlled descent of $3m/s$ can be achieved with reducing the throttle just under the hover throttle.

The total flight time of the quadplane can be estimated combining the VTOL and forward flight phases. For this calculation, the capacity of the battery has a 20% safety factor, which is above the 5% recommended reserve fuel in aircraft design [31]. The battery voltage levels during flight is presented in Section 5.3.4 showing its limitation in terms of vehicle autonomy. Taking-off with the vertical motors is the most power-consuming phase, therefore it must be performed as quickly as possible, it's estimated to take around 30 seconds to reach the desired transition altitude. Hovering and transitioning into and out from forward flight should take no more than 10 seconds each. This leaves the remaining battery storage to estimate the forward flight time, or cruise time, at trim throttle. Table 2.4 shows the estimated times, current drawn, and capacity spent for each flight phase. The total flight time is estimated just over 10 minutes, with a forward flight of around 8.5 minutes.

Table 2.4: Times and consumed capacity for each flight phase.

Phase	**Take-off**	**Hover**	**Trans. In**	**Trans. Out**	**Hover**	**Land**	**Cruise**
Time (s)	30	10	10	10	10	30	510
Current (A)	80	60	75	60	60	60	15
Spent Cap (Ah)	0.67	0.17	0.21	0.17	0.17	0.50	2.13
Spent Cap (%)	16.67	4.17	5.21	4.17	4.17	12.50	53.13

A summary of the quadplane specifications is presented in Table 2.5. These values are translated into the `Ardupilot` parameters for both simulation and real flight.

Table 2.5: Quadplane main specifications for `Ardupilot` parameter definition.

Fixed-Wing		Quadcopter	
Trim speed	15 m/s	Climb speed	3 m/s
Trim throttle	40%	Hover throttle	40%
Max. Speed	25 m/s	Max. Climb speed	10 m/s
Stall speed	11 m/s	Descent speed	3 m/s
Stall AOA	10°	Max. Descent speed	9 m/s
Cruise time	20 min	Hover time	6 min

2.3 Ground station development

The ground station is arguably the most important component for harnessing the power of the wind with AWES. The plane or kite requires a fixture point on the ground that holds the tether and generates enough tension to be able to fly in crosswind motion. Furthermore, the GS manages the tether reel in and out motion during the

take-off and landing phases, avoiding entanglement while it controls the tension or speed during the power generation phase. There are different approaches regarding the interaction between the ground station and the plane. An experimental setup for a rigid wing plane was developed with no communication between the plane and the GS, a mass-spring system is implemented to calculate the tension on the tether and the appropriate motor torque [26, 32]. Other research platforms use onboard LED and ground-based cameras to estimate the state of the plane [33], while the Twingtec prototype estimates the plane state using the line angles measurements combined with an Extended Kalman Filter [16]. The control approach taken for this AWES prototype is implementing a motor controller that can follow a torque set-point, applying a constant tension on the plane during crosswind flight.

2.3.1 Design specifications

The design and development of the ground station were carried out by 4th-year mechanical engineering students as part of their program requirements. First, a group of 5 students used the design specifications from the Software-in-Loop (SIL) simulation in Chapter 4 to provide an initial design [34], then the design was iterated, and further developed as part of an undergraduate honors thesis [35]. The main objective of the development of the ground station was to automate the tether management system during autonomous flights. The proposed design aims for portability so that the GS could be easily transported along with the plane to the testing location. The GS structure in Figure 2.11 is built of laser-cut Plywood sheets. It's comprised of a 15 cm diameter spool that winds the tether evenly throughout its entire length due to a linear winding mechanism, which is mechanically connected to the drum with a belt-pulley system. The tether coming from the plane is guided through a pulley that can rotate 360 deg to align itself with the plane at all times, the tether then passes through a series of pulleys where the tension sensor is mounted, and finally through the winding system and onto the spool. The rotation of the spool is driven by an electric motor connected by a shaft, and the whole system is powered by a 48 V battery bank.

2.3.2 Component description

The mechanical part of the ground station is presented on Figure 2.12, the orange line represents the tether passing through a series of components, neatly rolling onto

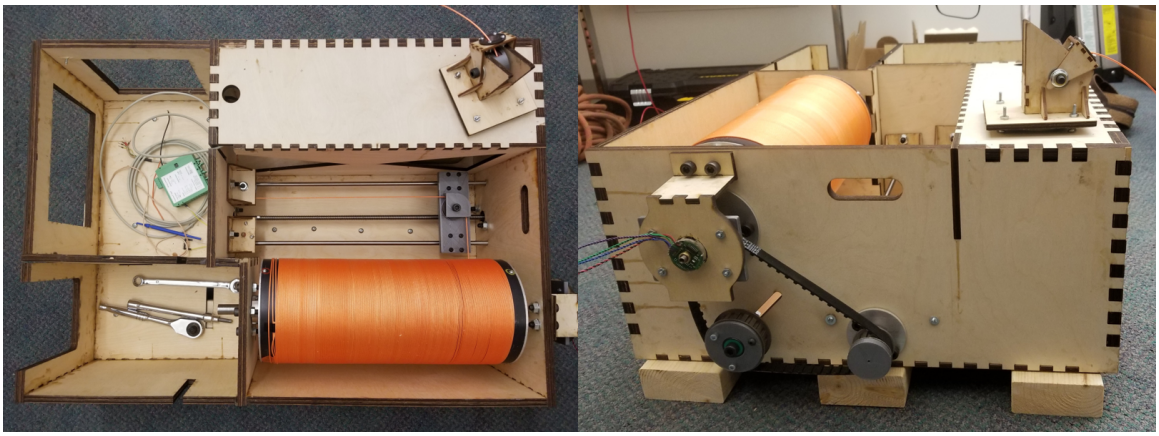

Figure 2.11: Ground station structure without power components

the spool, measuring tension, and orienting its direction towards the plane.

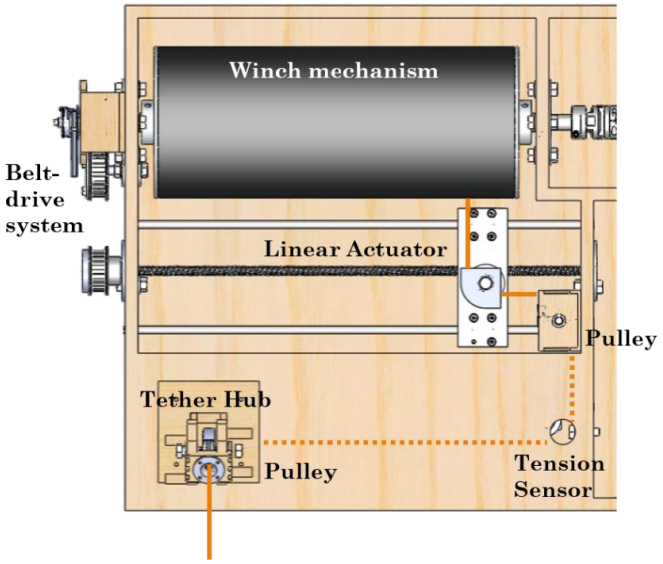

Figure 2.12: Ground station mechanical system diagram

The spool is a PVC tube of 15 cm diameter and 40 cm long, able to carry up to 100 m of tether, the tube is clamped on both sides by custom made aluminum caps, mechanically connected to the shaft by a set screw. One side of the shaft is connected to a belt-pulley system that drives the linear actuator mechanism, while the other end of the shaft couples to the motor gearbox.

The linear actuator consists of a lead screw that displaces a pulley along the spool center axis at a ratio of 1.6 mm per spool rotation, equivalent to the tether diameter. The pulley is mounted with linear bearings on two sliding rails, placing the tether

tangent to the spool radius and perpendicular to its center axis.

The tension sensor measurement is rated for up to 500 N, which is more than is expected to be generated during crosswind flight, still providing overload protection of over 800%. The Checkline RFS150 50K sensor is mounted "in-line", passing the tether through a pulley forming a 90° angle, the tension is then precisely calculated with the amplification of a strain-gauge measurement.

Finally, the tether changes direction from a horizontal to the vertical plane with a pulley that leads it to the rotating hub. A turntable equipped with a pulley receives the tether and allows free rotation along the vertical axis, along with free rotation from 0 to 90° elevation angle, covering all the orientations possibly achieved by the plane.

The electrical part is currently under development by a 4th year engineering student as part of a honours project. The next steps are to integrate the operational motor controller subsystem into the ground station, aiming to provide a constant torque set-point that would generate the constant tension used in the ideal winch simulation on Chapter 4. The Sevcon Gen4 motor controller is connected to an Arduino MEGA 2560, which uses the CANopen protocol to give the torque and speed commands. The micro-controller also integrates all the electronics of the ground station, recording tension and encoder measurements along with managing limiting switch signals.

2.4 Conclusions

This chapter presented the development of a lab-scale AWES prototype. A commercial RC model glider was structurally reinforced for tethered flight, VTOL hardware was incorporated, and autopilot components were integrated to allow a fully autonomous AWES mission. A detailed description of the autopilot components and how they are connected is presented, along with a description of the process that the pilot and crew must go through before each flight to ensure the safe operation of the quadplane. The key performance parameters were obtained from the quadplane physics in steady conditions. Trim speed and throttle were calculated from the balance of forces during stable flight, while hover throttle directly calculated from the plane weight and motor power. Moreover, the estimated mission time was presented as a function of the individual phases. Finally, a brief description of the ongoing development of the ground station is presented. Aiming for portability, the ground

station consists of an electric motor, spool, linear actuator, a tension sensor, and a battery pack contained in a custom-cut plywood box. The tether hub has the capability of rotating 360° to align the tether with the plane during flight. The ground station is currently under development to fully incorporate the motor controller and ultimately automate the entire system.

Further development is suggested on the expansion of battery capacity. The hovering time is a limiting factor for the quadplane, therefore, performing a power train and energy storage study could lead to weight reduction and flight time increase. To further reinforce the structure efficiently, it is appropriate to perform finite element analysis (FEA) studies on the wing spars, quadcopter frame, and 3D printed components reducing the weight while strengthening the overall structure for VTOL and tethered flight. Finally, vehicle weight is a crucial aspect of aerospace design, therefore replacing heavy and non-aerodynamic parts such as boom and motor mounts with custom-designed carbon fiber parts could potentially lead to better aerodynamic performance and increase of total flight time.

Chapter 3

Development of an Airborne Wind Energy System Model for Trajectory Following

3.1 Introduction

Computer modeling is the first step for understanding the physics of the system before moving into developing any prototype. A model allows evaluating the overall performance and assessing if the system will be feasible. Moreover, many different scenarios can be studied and further used for defining the initial design constraints. AWES relies on highly advanced control systems to autonomously maintain the plane airborne generating electricity. Therefore refining the control strategies is crucial before real-life implementation.

Sizing AWES is a challenging task; its operation makes these systems highly different from each other as seen in Chapter 1. The generation approach can either characterize the size of the ground station to handle the high tension, or the structural support on the plane to carry the onboard generators. On the other hand, the take-off and landing strategy will further affect the amount of power required by onboard motors, or the minimum torque required in the ground station winch. More challenges are introduced in the design of the plane, ground station, and tether themselves, where high aerodynamic forces generated in crosswind flight are the main constraint.

3.1.1 Motivation

The challenge of sizing the ground station with the loads generated in crosswind flight was the initial motivation for this chapter. In collaboration with New Leaf Management (NLM), the objective was to develop a simple MATLAB/Simulink AWES flight model that would integrate with the NLM proprietary ground station system Simulink block. The AWES flight model was developed with the following objectives

- Implement a simple navigation controller for trajectory tracking using as a reference geometrically defined trajectories such as circles and figure-8, or externally optimized trajectories; that maximize power output. The plane will apply roll rotations to stay along the flight path.
- Implement a simple reeling controller for pumping mode trajectory tracking, considering the plane speed and position, and assuming the tether as a inelastic rod.
- Assess traction loads and power generation for defining the initial design requirements of a commercial ground station.
- Develop a modular model allowing variations of input conditions such as wind speed profiles, and plane aerodynamic specifications, generation modes, and controller strategy.

3.2 Model Description

The dynamics model is a 3 DOF system developed in spherical coordinates. The plane or kite is modeled as a point-mass with aerodynamic properties. A similar study used spherical coordinate system to evaluate a control strategy using a kite's navigation angle for a fixed-length two-point trajectory [18]. Also, a Model-predictive-control (MPC) strategy was implemented to evaluate the system power generation potential for pumping and carousel configuration [36]. The developed model is adapted from the previous studies to use direct roll and pitch rotation control for single line rigid-wing planes, instead of line length roll control for soft kites. In addition, the navigation strategy implemented considers a non-linear trajectory tracking control for fully defined flight paths.

3.2.1 Coordinate System

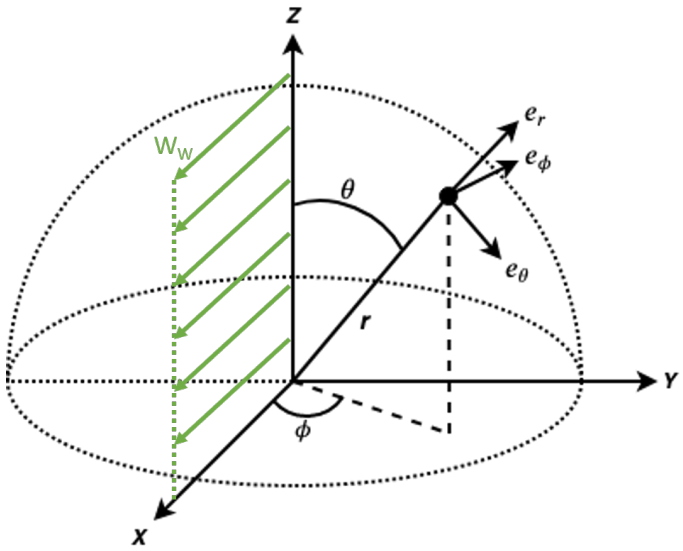

Figure 3.1: Coordinate system with reference uniform wind profile

.

The coordinate system used in the model is presented in Figure 3.1, the inertial system is represented in Cartesian coordinates system (X, Y, Z), and spherical coordinate system (ϕ, θ, r), where ϕ is the azimuth angle, θ is the elevation angle, and r is the radius. The relation between the two coordinate systems is described in Equation 3.1

$$\begin{pmatrix} X \\ Y \\ Z \end{pmatrix} = \begin{pmatrix} rsin(\theta)cos(\phi) \\ rsin(\theta)sin(\phi) \\ rcos(\theta) \end{pmatrix} \tag{3.1}$$

The body-fixed coordinate system (e_θ, e_ϕ, e_r) is obtained from rotating the inertial system with the rotation matrix described in Equation 3.2.

$$R = \begin{pmatrix} cos(\theta)cos(\phi) & -sin(\phi) & sin(\theta)cos(\phi) \\ cos(\theta)sin(\phi) & cos(\phi) & sin(\theta)sin(\phi) \\ -sin(\theta) & 0 & cos(\theta) \end{pmatrix} \tag{3.2}$$

3.2.2 Model Dynamics

The kite is assumed as a point-mass system with mass m, and wing area A. To obtain the particle's acceleration in spherical coordinates $(\ddot{\theta}, \ddot{\phi}, \ddot{r})$ in Equations 3.3, 3.4, 3.5,

the velocity of the particle $v = v_\theta e_\theta + v_\phi e_\phi + v_r e_r$ is derived in time obtaining a_θ, a_ϕ, a_r, which is finally used in Newton's Second Law of motion.

$$\ddot{\theta} = \frac{1}{mr}(F_{aero,\theta} + F_{app,\theta} + F_{grav,\theta} + F_{line,\theta}) \tag{3.3}$$

$$\ddot{\phi} = \frac{1}{mrsin(\theta)}(F_{aero,\phi} + F_{app,\phi} + F_{grav,\phi} + F_{line,\phi}) \tag{3.4}$$

$$\ddot{r} = \frac{1}{m}(F_{aero,r} + F_{app,r} + F_{grav,r} + F_{line,r} - F_{trac,r}) \tag{3.5}$$

The acting forces on the kite are the gravity $\bar{F}_{grav}$, apparent $\bar{F}_{app}$, line drag $\bar{F}_{line}$, aerodynamic $\bar{F}_{aero}$, and traction forces $\bar{F}_{trac}$.

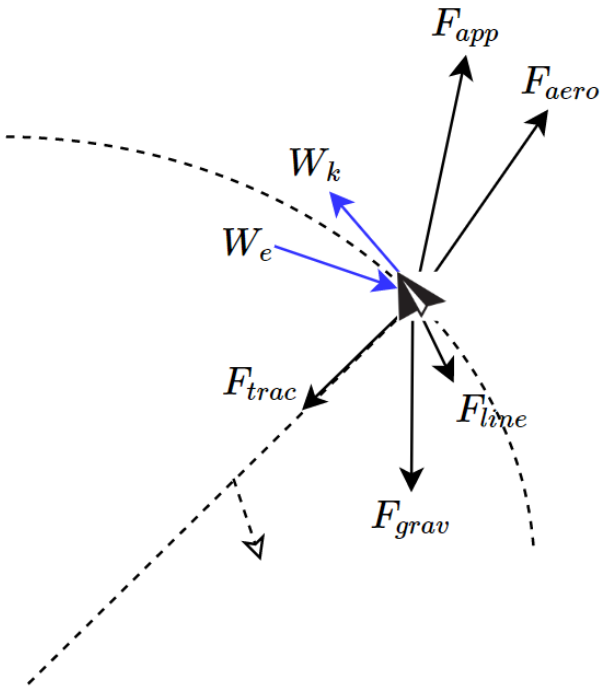

Figure 3.2: Model forces

The gravity force in Equation 3.6 combines the mass of the kite and lines, the latter assumed to be applied to the middle of its length and translated to the body coordinates.

$$\bar{F}_{grav} = \begin{pmatrix} (m + \frac{\rho_l \pi d_l^2 r}{4}) g sin(\theta) \\ 0 \\ -(m + \frac{\rho_l \pi d_l^2 r}{4}) g cos(\theta) \end{pmatrix} \tag{3.6}$$

The components resultant from deriving the position twice, become the apparent forces representing the centrifugal and inertial forces on the kite.

$$\bar{F}_{app} = \begin{pmatrix} m(\dot{\phi}^2 r sin(\theta) cos(\theta) - 2\dot{r}\dot{\theta}) \\ m(-2\dot{r}\dot{\phi} sin(\theta) - 2\dot{\phi}\dot{\theta} r cos(\theta)) \\ m(r\dot{\theta}^2 + r\dot{\phi}^2 sin^2(\theta)) \end{pmatrix} \tag{3.7}$$

Assuming that the apparent wind speed is perpendicular to the line direction, a tether with projected area A_l and drag coefficient $C_{D,l}$ produce a line drag force described in Equation 3.8.

$$\bar{F}_{line} = -\frac{\rho C_{D,l} A_l cos(\Delta\alpha)}{8} |\bar{W}_e|^2 \bar{x_W} \tag{3.8}$$

The line traction force F_{trac} is always oriented in the line direction or e_r unit vector and can't be negative. For this model, the speed in the r direction is an input and therefore the acceleration is known, using Equation 3.5 the line force is then calculated.

The total aerodynamic forces acting on the kite are obtained from Equation 3.9. Where the apparent kite speed W_e is obtained from the wind speed W_w, and the kite speed W_k in the inertial coordinate system.

$$\bar{F}_{aero} = -\frac{1}{2} C_D A \rho |\bar{W}_e|^2 \bar{x_W} - \frac{1}{2} C_L A \rho |\bar{W}_e|^2 \bar{z_W} \tag{3.9}$$

$$\bar{W}_e = \bar{W}_w - \bar{W}_k \tag{3.10}$$

$$\bar{W}_w = \begin{pmatrix} W_x \\ W_y \\ W_z \end{pmatrix} \tag{3.11}$$

$$\bar{W}_k = \begin{pmatrix} \dot{\theta} r \\ \dot{\phi} r sin(\theta) \\ \dot{r} \end{pmatrix} \tag{3.12}$$

The kite wind coordinate system represented as (x_W, y_W, z_W) with x_W aligned with the kite's apparent wind speed vector, y_W pointing in the direction of the right wing, and z_W pointing down. The wind coordinate system is affected by the roll control input ψ which navigates the plane through the waypoints by directly changing the direction of the aerodynamic forces.

$$\bar{x_W} = -\frac{\bar{W_e}}{|\bar{W_e}|} \tag{3.13}$$

$$\bar{y_W} = \bar{e_W}(-cos(\psi)sin(\eta)) + (e_r \times e_W)(cos(\psi)cos(\eta)) + e_r sin(\psi) \tag{3.14}$$

$$\bar{z_W} = \bar{x_W} \times \bar{y_W} \tag{3.15}$$

with

$$\bar{e_W} = \frac{\bar{W_e} - e_r(e_r \cdot \bar{W_e})}{|\bar{W_e} - e_r(e_r \cdot \bar{W_e})|} \tag{3.16}$$

$$\eta = \arcsin\left(\frac{\bar{W_e} \cdot e_r}{|\bar{W_e} - e_r(e_r \cdot \bar{W_e})|} tan(\psi)\right) \tag{3.17}$$

Finally, the lift and drag coefficients $C_L(\alpha)$ and $C_D(\alpha)$ are a function of the angle of attack α shown in Figure 3.3, obtained from the kite's pitch angle α_0 and the angle between the apparent wind speed and the plane perpendicular to r $(\Delta\alpha)$

$$\alpha = \alpha_0 + \Delta\alpha \tag{3.18}$$

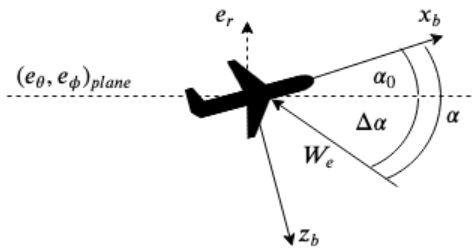

Figure 3.3: Pitch and angle of attack

$$\Delta\alpha = \arcsin\left(\frac{e_r \cdot \bar{W}_e}{|\bar{W}_e|}\right) \tag{3.19}$$

The system total power output in Equation 3.20 is estimated based on a pumping mode operation. The traction force during the reel-out phase drives a ground station generator resulting in positive power and consuming power during the reel-in phase.

$$P = F_{trac}\dot{r} \tag{3.20}$$

3.3 Controls

The control system is comprised of the navigation, reeling, and pitch controller.

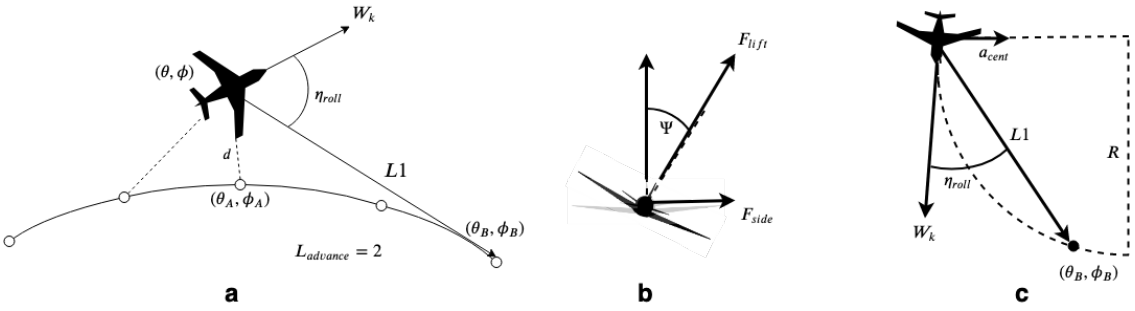

Figure 3.4: Navigation control

.

3.3.1 Navigation controller

The navigation controller produces a roll command to the kite to follow the defined trajectory as seen in [37], this navigation strategy is based on a non-linear guidance logic for trajectory tracking presented in [38]. The first step of the navigation controller is to find the closest point from the kite to the trajectory in the (θ, ϕ) plane, then an auxiliary vector $L1$ is generated from the kite to a point $L_{advance}$ positions ahead of the closest point, with $L_{advance} = [1, 2, 3, ...]$ and tuned for specific flight paths. This produces an angle η_{roll} with the apparent velocity of the kite, see Fig. 3.4.a for reference.

To calculate the required roll of the kite to meet the target point, the lateral acceleration must be calculated. By rolling the plane, the aerodynamic lift force is

rotated in the direction of the roll and can be then decomposed into a vertical force parallel to the weight of the plane, and a horizontal force; also called side-force, see Fig. 3.4.b then the lateral acceleration $a_{lateral}$ in Equation 3.21 can be obtained using Newton's law.

$$a_{lateral} = \frac{F_{lift} sin(\Psi)}{m} \tag{3.21}$$

On the other hand, the roll-induced side-force makes the plane move in a circular arc with a radius R (Fig. 3.4.c), described as a function of the centripetal acceleration in Equation 3.22; given by Newton's second law in the direction of the side-force, and the kite's airspeed.

$$a_{cent} = 2\frac{W_k^2}{L1} sin(\eta) \tag{3.22}$$

Combining Equations 3.21 and 3.22 we obtain the required roll Ψ that will take the kite to the target waypoint through a circular path presented in Equation 3.23.

$$\Psi = \arcsin\left(\frac{2mW_k^2 sin(\eta)}{F_{lift} L1}\right) \tag{3.23}$$

The navigation controller operates in the (X, Y, Z) space. As a result, it can cause deviation from the trajectory in cases where the path crosses itself, such as a figure-8 trajectory. Therefore, an enhanced navigation controller is implemented, where the closest point to the kite is selected from only a defined number of points ahead (*look-ahead*) from the previous target point. This allows the controller to ignore crossing trajectories, and avoid skipping sections. This variable depends on the number of points in the trajectory and must be tuned for each defined path.

3.3.2 Reeling controller

The reeling controller represents the ground station winch, in charge of allowing the kite to operate in pumping mode. The tether is assumed as an inelastic straight rod, therefore the reeling speed commanded by the GS directly affects the kite's state. The reeling speed can be either set constant to 0.25 times the wind speed for traction, and 1.5 times the wind speed for the retraction phase for maximum pumping cycle power as derived in [39]. For trajectory tracking a simple reeling speed controller is implemented which considers the time that the plane takes from its current position

to the target location Δt, the radial speed $\dot{r}$ needed to approach the target waypoint radius r_B is then calculated with Equation 3.24. The time from actual position to target position is calculated using Equation 3.25 where the distance $\bar{d}$ from the current point (θ, ϕ, r) to the target point (θ_B, ϕ_B, r_B) is divided by the velocity of the plane V_k projected in the target point direction.

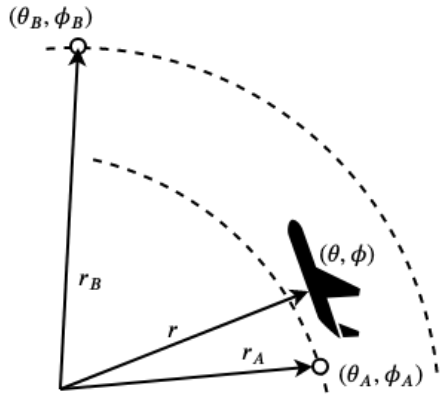

Figure 3.5: Reeling control

$$\dot{r} = \frac{r_B - r}{\Delta t} \tag{3.24}$$

$$\Delta t = \frac{|\bar{d}|}{\bar{V}_k \cdot \hat{d}} \tag{3.25}$$

3.3.3 Pitch controller

The pitch angle of the plane constantly changes following Equation 3.18 to meet the specified angles of attack. Throughout the reel-out phase the angle of attack is set to a maximum to increase the generated lift force and therefore the traction power generation. During the retraction phase, the plane should change its attitude to orient the nose towards the direction of the coming wind speeds, flying like a conventional plane while the ground station reels the tether in with low tension. The angle of attack then approximates to zero which provides enough lift to sustain the retraction flight. This strategy, however, requires a good interaction between the plane roll and pitch angles as an early pitch maneuver still in crosswind will decrease the tension on the tether and cause the plane to deviate from the flight path. Finally, for optimized trajectory tracking the angle of attack is used as an input to allow evaluation of the

navigation and reeling controllers.

3.4 Model Input

3.4.1 Wind profile

The simulation can be initialized with three different wind profiles defined in the (X, Y, Z) coordinate system in Equation 3.11. The uniform profile has a constant value throughout the Z axis. The logarithmic profile can be either read from a wind speed vs altitude file which is then linearly interpolated between the given points for the operating altitude, or calculated using the Hellman exponent where the wind speed at Z in Equation 3.26 is a function of the wind speed W_{10} at the reference height Z_{10} and the Hellman's exponent a which depends on the terrain and air conditions.

$$W_z(Z) = W_{10}\left(\frac{Z}{Z_{10}}\right)^a \tag{3.26}$$

Finally, more realistic wind profiles are obtained from Weather Research and Forecasting Model (WRF) models [40], which are also used to output the reference trajectory from the open-source flight trajectory optimizer `AWEbox` [41].

3.4.2 Reference trajectory

The reference trajectory can be defined as a circle, figure-8, or an optimized trajectory given by the `AWEbox` toolbox, these can be either constant or variable tether length for drag and pumping mode respectively.

A circular trajectory on the surface of a sphere of radius R can be generated in the (X, Y, Z) reference system with Equation 3.27, with r the radius of the circle, $\theta = [0, 2\pi]$, and a constant altitude h. Then it is rotated with an angle ϕ along y axis using the matrix in Equation 3.28.

$$\begin{pmatrix} X \\ Y \\ Z \end{pmatrix} = \begin{pmatrix} r\sin(\theta) \\ r\cos(\theta) \\ \sqrt{R^2 - r^2} \end{pmatrix} \tag{3.27}$$

$$R_y = \begin{pmatrix} cos(\phi) & 0 & sin(\phi) \\ 0 & 1 & 0 \\ -sin(\phi) & 0 & cos(\phi) \end{pmatrix} \tag{3.28}$$

The figure-8 trajectory is described as a Lissajous curve, and can be generated using Equation 3.29, with $\delta_x = RJ_{lissajous}$ and $\delta_y = \sqrt{R^2 - Z^2}$, with an scaling factor $J_{lissajous} = [0.3, 0.7]$ that changes the angle between the crossing lines. Finally the trajectory is rotated along the Y axis using the rotation matrix R_y.

$$\begin{pmatrix} X \\ Y \\ Z \end{pmatrix} = \begin{pmatrix} x_0 + \delta_x \sin(2t) \\ y_0 + \delta_y \cos(t) \\ 0.8R \end{pmatrix} \tag{3.29}$$

Figure 3.6 presents the result of a circular trajectory with a radius of 50m and a figure-8 trajectory with $J_{lissajous} = 0.3$ projected on a sphere with radius 120m and with 45°inclination angle.

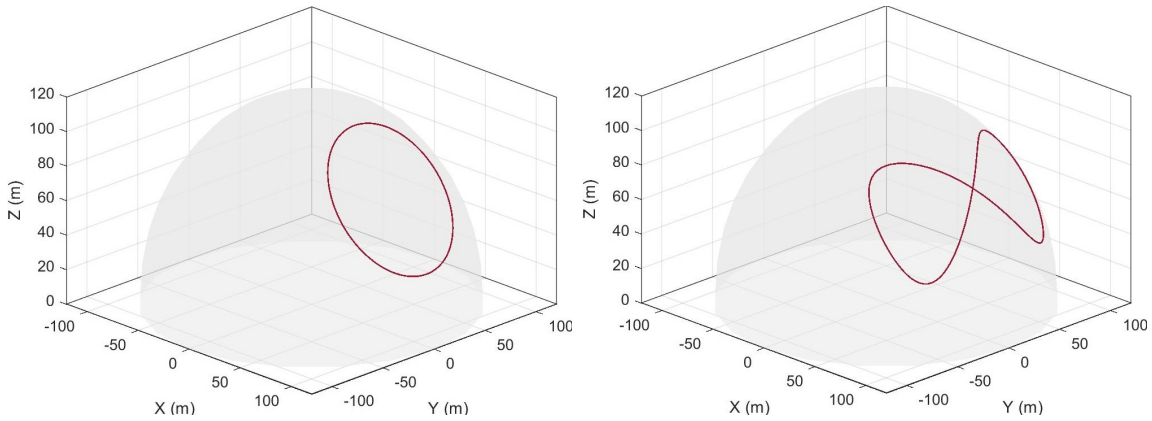

Figure 3.6: Circle and figure-8 reference trajectories

Pumping mode trajectory

Pumping mode operation in the model can be achieved with two different trajectories and control approaches. First, a constant reeling speed is commanded while the constant radius trajectory is projected at the current plane radial position, once the maximum radius or tether length is reached the reeling speed becomes negative to allow the plane retraction until switching back to reel-out after reaching the minimum length. In this case, a different retraction trajectory can be implemented where the

circle θ, ϕ angles can be scaled to create a bigger or smaller trajectory. The switch between reel in/out does not happen always at the same point in the trajectory, as it only depends on the radial position of the plane.

The second approach involves pre-defining the trajectory, incorporating a non-constant r coordinates to a series of loops prescribed with θ and ϕ angles. Thus using the reeling controller to calculate the tether speed to closely follow the flight path. The trajectory in Figure 3.7 is generated by setting 3.25 reel-out loops, and 0.75 reel-in loops between the limit radius of 100 and 150 meters, the retraction path azimuth angle is scaled from 1 to 1.7 for the first half and inversely for the second half, the scaling in ϕ leads the trajectory outside the wind power zone preventing peaks in the apparent wind speed.

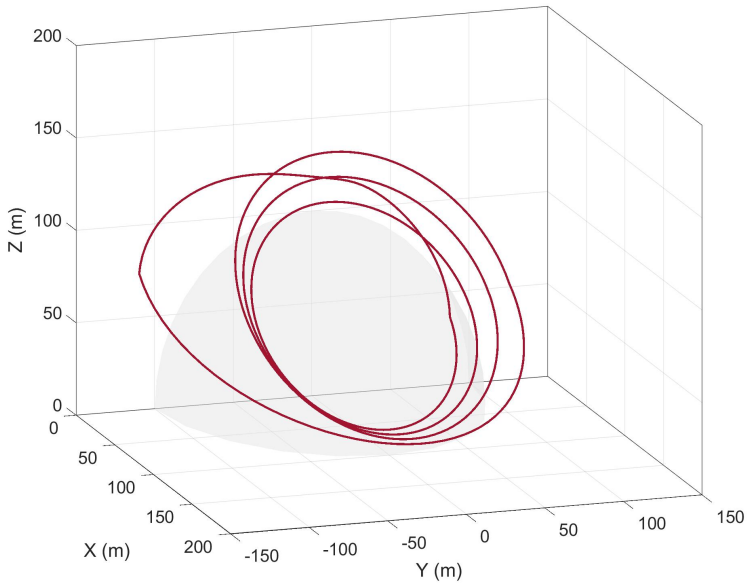

Figure 3.7: Reference trajectory for variable tether length

AWEbox reference trajectory

An open-source toolbox `AWEbox` [41] is implemented to obtain optimal flight paths that maximize the pumping cycle power generation. The trajectories can be generated from a series of different wind profiles as presented in Figure 3.8 which result in less geometrically symmetric trajectories than the common circle or figure-8. The optimization considers losses in tether weight and drag, non-uniform wind profiles,

plane aerodynamics, and more. A uniform wind trajectory will keep a low altitude to prevent further tether losses due to its length, as it is not convenient to climb higher as the wind speeds remain constant. A logarithmic wind profile increases its wind speed with height. Therefore, the plane can take advantage of the increased wind speeds when the power tends to decrease. These trajectories tend to approximate to a symmetric circle. Finally, WRF profiles can have a maximum wind speed at different heights, thus the optimizer tends to perform the power loops closer to these high wind zones. The trajectory is discretized from its function form to 100 points in Cartesian coordinates and then converted into spherical coordinates using Equation 3.30.

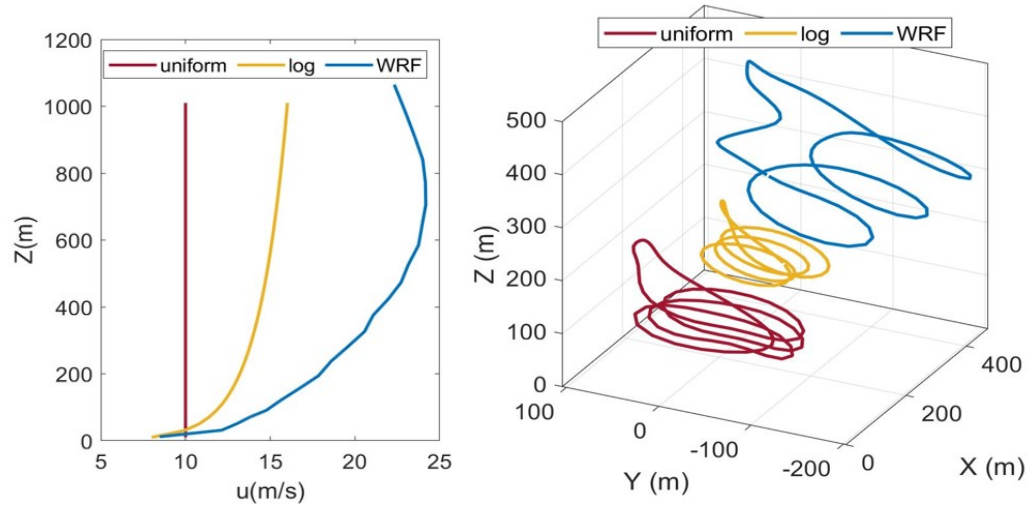

Figure 3.8: Wind profiles and optimized trajectories for uniform, logarithmic, and WRF wind profiles

$$\begin{pmatrix} \theta \\ \phi \\ r \end{pmatrix} = \begin{pmatrix} \arccos \frac{Z}{r} \\ \arctan \frac{Y}{X} \\ \sqrt{X^2 + Y^2 + Z^2} \end{pmatrix} \tag{3.30}$$

3.4.3 Aerodynamic parameters

The plane aerodynamic parameters are an input to the aerodynamic force calculation. They are taken directly from the Ampyx AP2 prototype specified in the `AWEbox` code, the lift and drag constants are used to generate a linear and quadratic curves for the lift and drag coefficients respectively shown in Figure 3.9. Another plane could be

easily implemented in the model by following the same definition of the aerodynamic specifications.

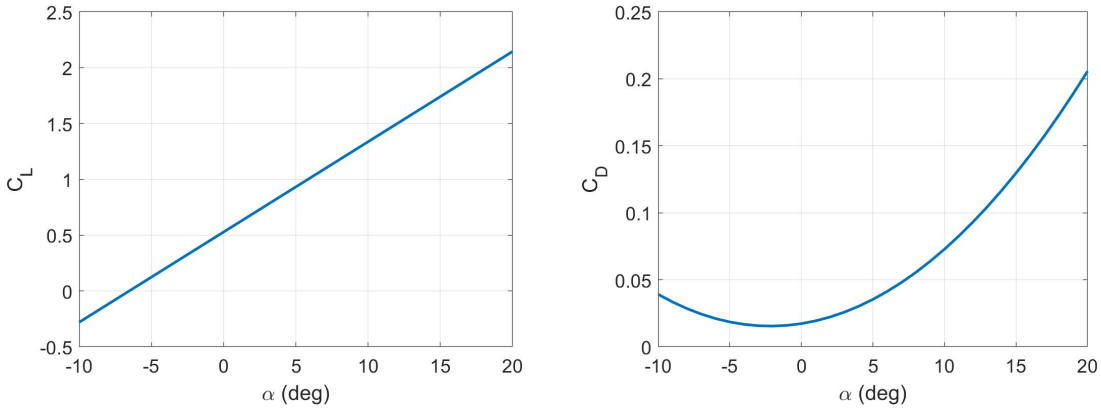

Figure 3.9: Lift and drag coefficient of the reference plane

3.5 Results and Discussion

Fixed tether length trajectory tracking

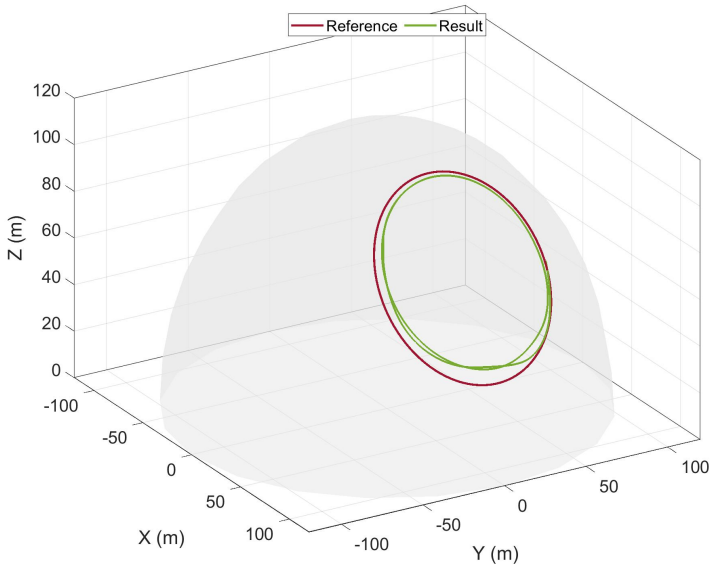

Figure 3.10: Simulation result for circle trajectory

The performance of the navigation controller can be evaluated by simulating reference trajectories with fixed tether length, in the following cases the radius of the sphere or tether length is defined to $R_{sph} = 120m$. The plane specifications are based on the Ampyx AP2 prototype which weights 36 kg and has 4 m^2 of wing area. The tether selected has a diameter of 3 mm and a density of 970 kg/m^2. The wind profile is uniform and has a speed of 10 m/s in the X direction.

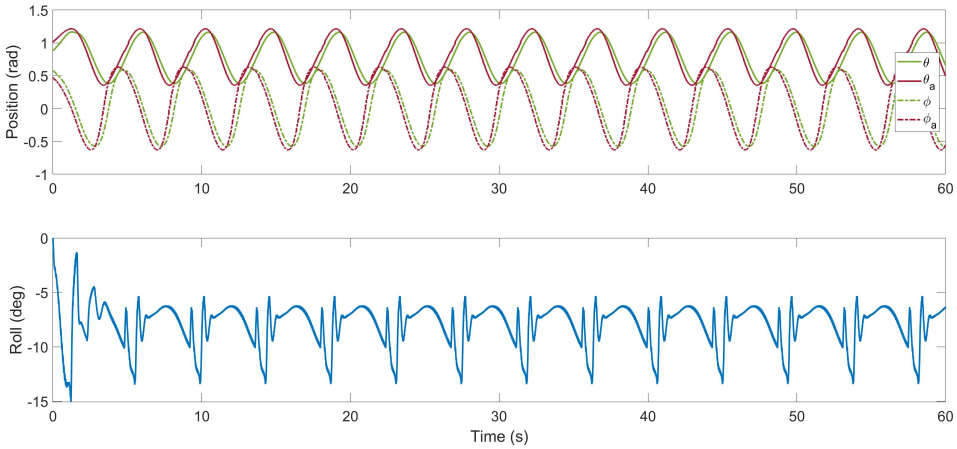

Figure 3.11: Navigation results for circle trajectory

The navigation controller requires tuning before it can successfully follow the defined trajectory. The L_{adv} refers to how many points ahead of the closest point the plane should be aiming, smaller L_{adv} will generate higher roll angle commands and will tend to follow the trajectory closely, while higher L_{adv} will have lower roll angle commands and will tend to cut the corners of the trajectory. A proportional gain G_P is applied to the roll command to smooth or intensify the commanded roll angle. Finally, a second-order Butterworth filter with a cut-off frequency ω_η is applied on the reference heading angle η_{roll} as seen previously in [18] to remove the high-frequency oscillations generated by the calculation of the L1 vector while the target point is moving in L_{adv} number of steps.

The circular trajectory simulation results are presented in Figure 3.10 and 3.11, the isometric plot presents a contrast of the reference trajectory (red) and the simulated result (green). The navigation controller is then evaluated by comparing the active point (θ_a, ϕ_a) with the plane position in spherical coordinates (θ, ϕ). This result corresponds to the control parameters of $L_{adv} = 6$, $G_P = 0.4$, and $\omega_\eta = 35$. Combined, they estimate the commanded roll angle that the plane must have to successfully

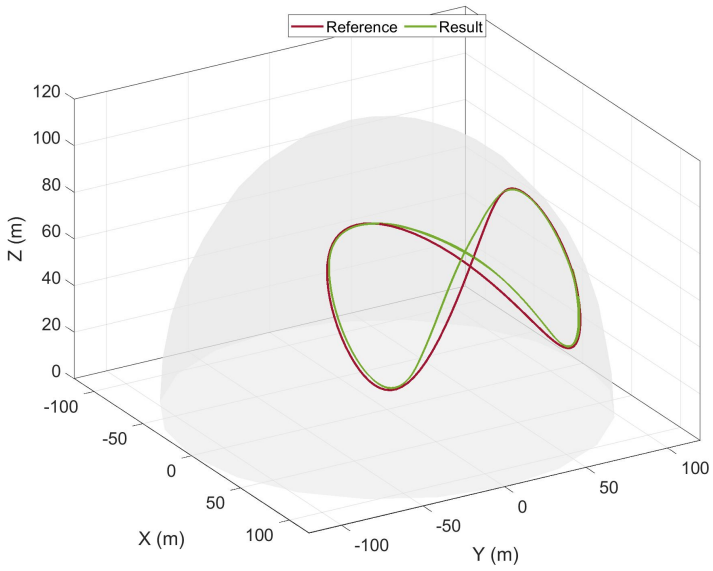

Figure 3.12: Simulation result from figure-8 trajectory

follow the reference trajectory.

A similar tuning process was performed for the figure-8 simulation; results are presented in Figure 3.12 and 3.13. The main difference is that the advance parameter had to be decreased to $L_{adv} = 6$ in order to avoid cutting the corners on the tight turns of the figure-8; additionally, the roll angle to perform these turns must be higher and therefore the proportional gain was increased to $G_P = 1.1$. The cut-off frequency of the filter for both trajectories provided a stable roll command calculation at $\omega_\eta = 35$. Any lower value will cause the roll to have high oscillation and become unrealistic for the plane operation.

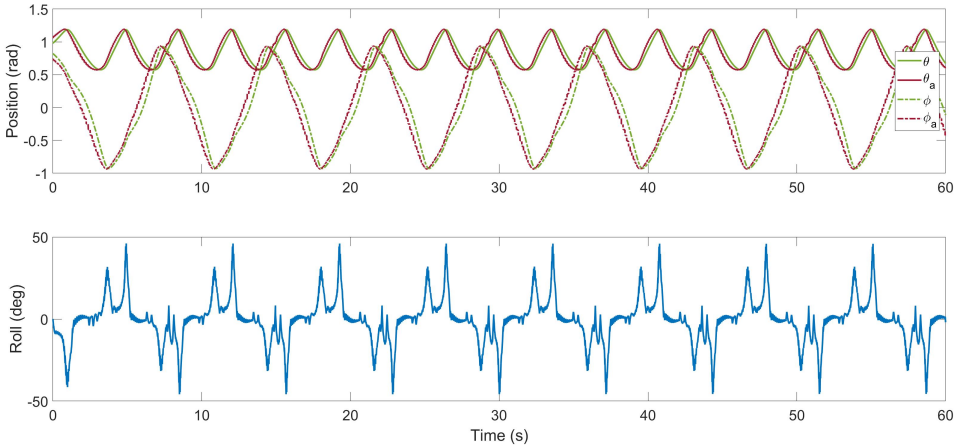

Figure 3.13: Simulation result from figure-8 trajectory

3.5.1 Pumping mode trajectory tracking

The simulation results presented in Figures 3.14 and 3.15 were obtained with a uniform wind profile of 10 m/s speeds. The results show three complete pumping cycles within 100 and 150 m of tether length. The reference and current position are shown as the red and green lines respectively. The position in spherical coordinates shows that the plane closely follows the reel-out trajectory and the reeling speed oscillates between the suggested 1/4 times the wind speed, consequently producing oscillations in the same frequency in the tether tension.

The reel-in or retraction phase does not follow the specified trajectory, mainly because the tether speed is saturated at -7 m/s. From several runs the reeling speed limit had to be tuned to allow the simulation to converge and have close to zero retraction tension. Removing the saturation entirely caused the tether speeds to become forbiddingly high and produce tension peaks over the physical limitations of the system.

The main hypothesis for the deviation of the retraction trajectory is the attitude of the plane. First, to reel-in with low tether tension and reduced power requires plane speeds higher than the reeling speed, causing a negative tension which physically means that the tether would become slack. Then, the pitch, roll, and yaw must align the plane so the lift force generated is just enough to sustain the plane flight, accounting only for the weight of the tether. Consequently, the reeling controller requires a successful trajectory tracking from the navigation and pitch controller. To investigate this hypothesis, optimized trajectories from `AWEbox` are implemented

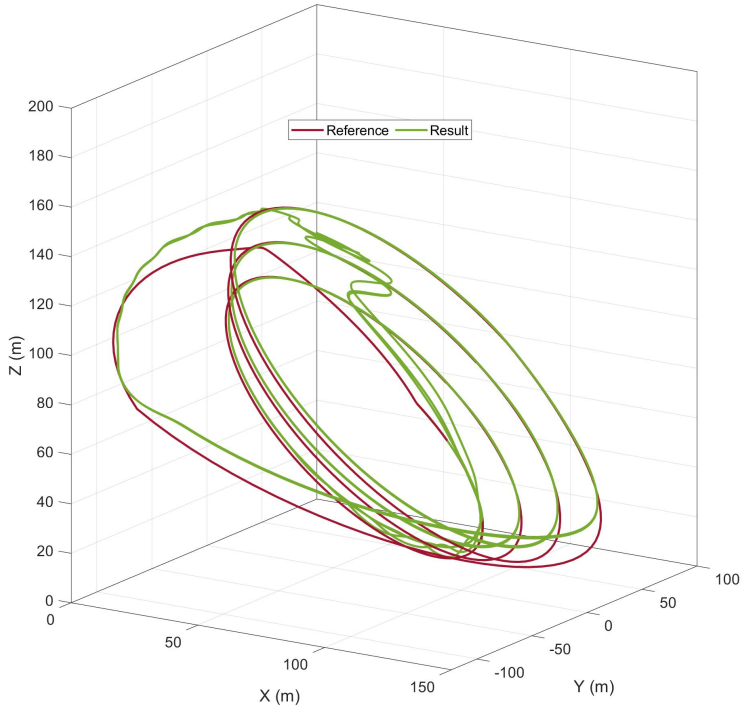

Figure 3.14: Reference and simulation trajectory for pumping mode operation

using the resultant angle of attack profile as an input to the model.

The implemented plane is the Ampyx AP2 with a wing area of 4 m^2 and 36 kg of weight, producing an average traction power of 35 KW which represents 38% of the theoretical power limit from Equation 1.1, while the maximum power is 91% of Loyd's power. Moreover, the AP2 was not designed for power generation but for testing the flight control algorithms. This is demonstrated by the resultant 0.07 KWh of total rated energy of an entire pumping cycle, suggesting that the energy generated during the traction phase is being entirely consumed by the GS to reel in the tether.

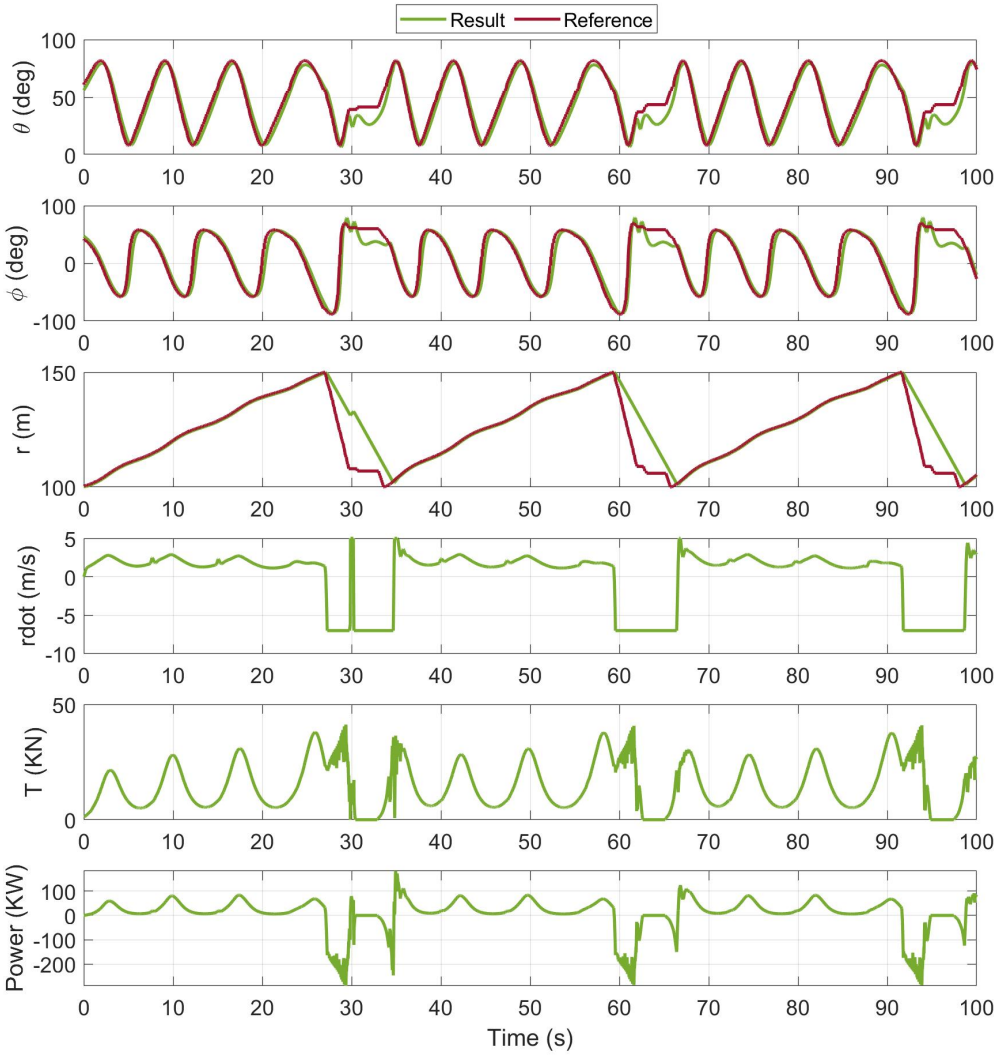

Figure 3.15: Reference and simulation results for pumping mode operation

3.5.2 Optimized trajectory tracking

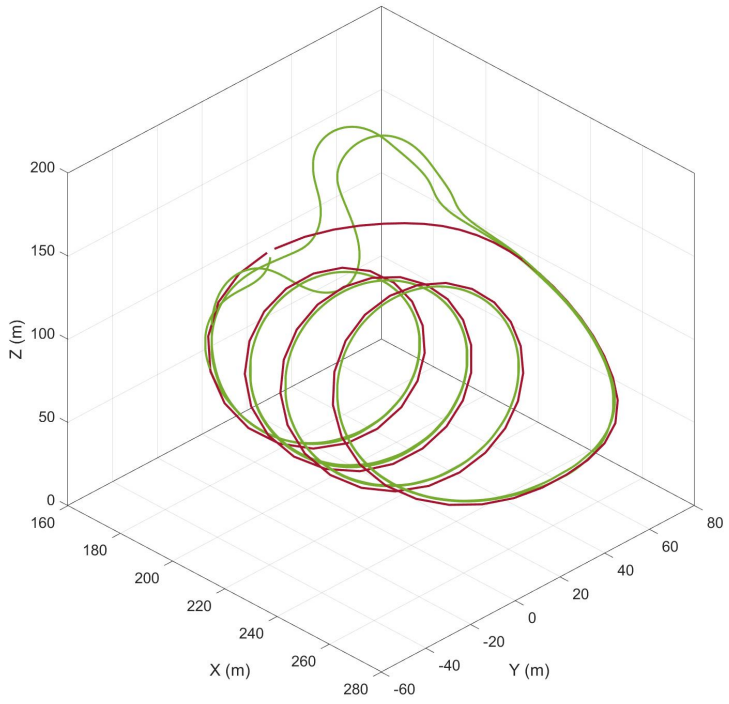

Figure 3.16: `AWEbox` reference trajectory with logarithmic wind profile with 8 m/s reference speed and simulation result

The simulation was performed using the `AWEbox` optimized trajectory as reference for logarithmic wind profile with a reference speed of 8 m/s at 10 meters high. To evaluate the trajectory in power generation the AP2 plane was scaled-up to a wing area and weight of 12 m^2 and 183 kg respectively. For such a device the tether diameter was estimated to be 14 mm with a material density of 970 kg/m^3. The resultant trajectory for two consecutive pumping cycles is presented in Figure 3.16, and detailed simulation results are presented in Figure 3.17. The `AWEbox` reeling speed, tension, and power results (red line) are used as a reference for the simulation results.

During the reel-out or traction phase, the navigation and reeling controller successfully fly the plane along the reference trajectory as seen in the spherical coordinates θ, ϕ, r. However, during the reel-in phase, approximately after 15 seconds, the plane starts to deviate from the trajectory overshooting the azimuth angle and oscillating

around the elevation angle.

Comparing the simulation with the `AWEbox` results, the main discrepancy is in the reeling speed $\dot{r}$, which more than doubles the reference tether speed during reel-in phase. This is a consequence of how the reeling controller is defined, considering the current velocity of the plane to calculate the time it will take getting from the actual position to the target point, finally calculating the reeling speed. If the plane diverges too far off from the trajectory, the resultant reeling speed is increased forcing the plane back into the path, thus generating unwanted tension on the tether and negative power peaks. The reeling speed plot shows how the controller tries to follow the radial position even when the azimuth and elevation angles are off; the results are sudden oscillations in the reeling speed that reach peaks of over 50 m/s.

The traction phase produces similar tension to the `AWEbox` results, and consequently the power production estimated with Equation 3.20 also matches. This leads to conclude that the navigation and reeling control strategy can follow an optimized AWES trajectory without compromising the system power performance. On the other hand, the controllers achieve the retraction and re-integration of the cycle with the trade-off deviating from the reference path.

These results show the challenge of implementing individual controllers to follow a complex high-fidelity trajectory. On the other hand, during the traction phase, the combination of navigation and reeling controller allows the plane to achieve similar power as the optimization result, which leads to conclude that the model may require a different controller strategy for the retraction phase which considers the entire state of the system including plane state and ground station operation.

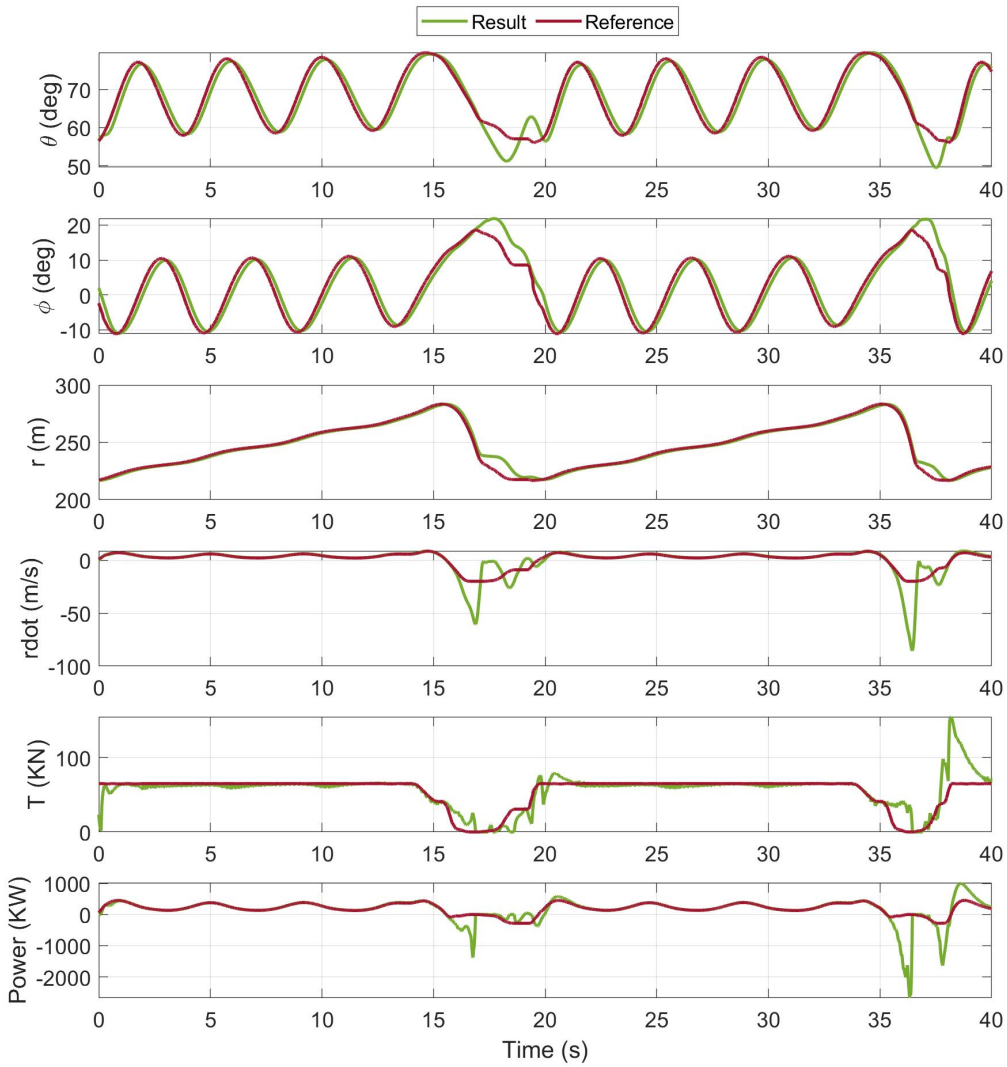

Figure 3.17: `AWEbox` reference results and simulation results for logarithmic wind profile with 8 m/s reference speed

3.6 Conclusion and future work

In this chapter an AWES model was developed using a 3DOF spherical coordinate system. The kite or plane is modeled as a point mass with roll and pitch rotations. The tether is represented as an inelastic rod with drag, weight, and traction forces applied on the plane. The navigation controller provides a roll command that orients the plane toward the target point ahead, the reeling controller provides a tether speed command, and finally, the pitch controller maintains a reference angle of attack during the flight. The results show that the navigation controller can follow a circle or figure-8 trajectory with constant tether length. The reeling controller outputs the appropriate speed to follow a generic variable-length or optimized trajectory. The tension and power resultant from the simulation match the output from the `AWEbox` results for the traction phase while the plane deviates from the trajectory during the retraction reducing the total cycle power, still able to reincorporate the flight path and complete the pumping cycle.

The direct roll control of the airplane does not consider the effect of the control surface deflections and rotational inertias. Such simplified model provides only a quick tool for trajectory tracking evaluation, and power and loads estimation. For hardware implementation, it is required to have a higher fidelity physics and controller model as seen in Chapter 4.

Entirely following the specified trajectory requires that the individual controllers are merged into one controller. This would consider the full and reference state to navigate the plane seamlessly through the specified trajectory. In addition, it is relevant to consider implementing an elastic tether and a ground station model to evaluate the loads generated from the interaction between the ground station and the plane.

Chapter 4

Open-source Autopilot Platform for Airborne Wind Energy System Simulation and Testing

4.1 Introduction

The complexity of Airborne Wind Energy Systems (AWES) is mainly due to the required flight controls. AWES require a robust flight controller that navigates the plane to maximize electricity production while accounting for unexpected events such as change of environmental conditions (wind speed reduction or wind gusts). As a consequence, AWES must match the reliability achieved in the aerospace industry, ensuring the plane safe operation even while producing energy through tethered flight. Automation is a key factor to achieving this goal, as the system must operate without requiring any human intervention. Its autopilot must know when to take-off, where to position itself to generate power, and when to land depending on the wind conditions. When the automation challenge is solved, and the technology becomes robust, reliable, and affordable, then it can be introduced into the energy market.

The previous chapter demonstrated that an AWES model plane can follow a defined trajectory with the implementation of a simple navigation strategy for a simplified model. It also presented the challenge of developing a robust controller that navigates the plane throughout the entire pumping cycle. This chapter focuses on implementing a more realistic flight model to simulate the operation of AWES.

AWES development covers: design, modeling, simulation, testing, and analysis.

The `Ardupilot` platform includes, to some extent, all of the previous aspects, making it an excellent candidate for a prototype development. First, `Ardupilot` is an open-source autopilot that supports a wide range of vehicles [28], allowing the implementation of different plane concepts. The code is flexible in terms of the physical specifications of the airframe, parameters such as stall speed, wing area, and weight are easily defined. Second, the open-source license allows local ownership the source code. By understanding the system's architecture, the physical model and controls can be modified to account for key AWES aspects, such as the tether forces and additional drag. Third, the code is compatible with numerous external tools. It can be compiled and used in a Software-in-Loop (SIL) simulation. This allows the evaluation of the model in a controlled environment. This is highly valuable for testing new models, controllers, and trajectories without the risk of damaging the hardware. Fourth, the vehicle code can be compiled onto firmware and uploaded to a real flight controller. Once the simulation is fine-tuned, it can proceed to hardware implementation. These two complement each other, ultimately matching them would result in a robust and reliable system. Finally, `Ardupilot` provide a data logging system that can easily be converted into a manageable format for post-flight analysis.

4.1.1 Motivation

Given the challenges in flight control presented in Chapter 3, this chapter aims to use a robust autopilot that allows the simulated automation of an entire AWES operation. The `Ardupilot` SIL tool is used to ultimately tune the simulation, obtaining the controller parameters, flight plans, and models, that are best be suited to operate the hardware in further test flights. The specific objectives are as follows:

- Identify the key aspects of the `Ardupilot` platform that enables AWES operation, such as controls, flight plan definition, physics models, and recorded data formats.
- Incorporate a tether model that considers drag, weight, and tension as additional forces on the plane physics model. Resembling a simplified behavior of the actual tether, and considering its physical limitations.
- Enable VTOL on the SIL simulation to evaluate the quadplane operation. This aims to identify the key parameters to consider during a real flight such as, transition speeds, hover throttle, and external forces.

- Tune the quadplane flight controllers for tethered crosswind flight and trajectory tracking. With the goal of obtaining the parameter and mission files to be uploaded to the hardware.
- Evaluate the effects of an ideal winch model in crosswind trajectory tracking. To obtain the torque set-point to be implemented on the ground station winch.
- Evaluate the `Ardupilot` platform for potential power generation with drag and pumping mode approach.

4.2 The `Ardupilot` architecture

The `Ardupilot` allows SIL simulation and hardware implementation. Figure 4.1 show the architecture of the `Ardupilot`. The ground control software provides an user interface to control the plane. It allows mission definition through waypoint planning, parameter visualization and modification, and live visualization of the plane data sent with the telemetry system. The ground control software communicates with the vehicle code with the MAVLink messaging protocol, and sends information such as sensor data, navigation commands, and flight modes. The vehicle code libraries contain the specific vehicle files, shared libraries, and the Hardware Abstraction Layer, which makes the code compatible with different platforms. On the plane specific files, the main file is the `ArduPlane.cpp`. This file runs a series of of sub-functions such as the Altitude Heading Reference System (ahrs_update) that estimates the state of the aircraft using an Extended Kalman Filter (EKF). The vehicle code can be either compiled into the SIL simulation, or the flight controller firmware. On the simulation, the vehicle code uses simulated data obtained from the flight dynamic model. SIL files contain the physics model implemented in the simulation, and thus can be edited to incorporate the tether model and plane aerodynamic specifications. On the other hand, the real flight controller uses the data from sensor measurements (airspeed, accelerometers, GPS, etc.), and decides the output signals from the vehicle code running inside the controller. Either simulation or hardware, the data log files are recorded in a `.bin` format. Which can be either visualized directly on the ground control software, or easily converted into a text or MATLAB file for further analysis.

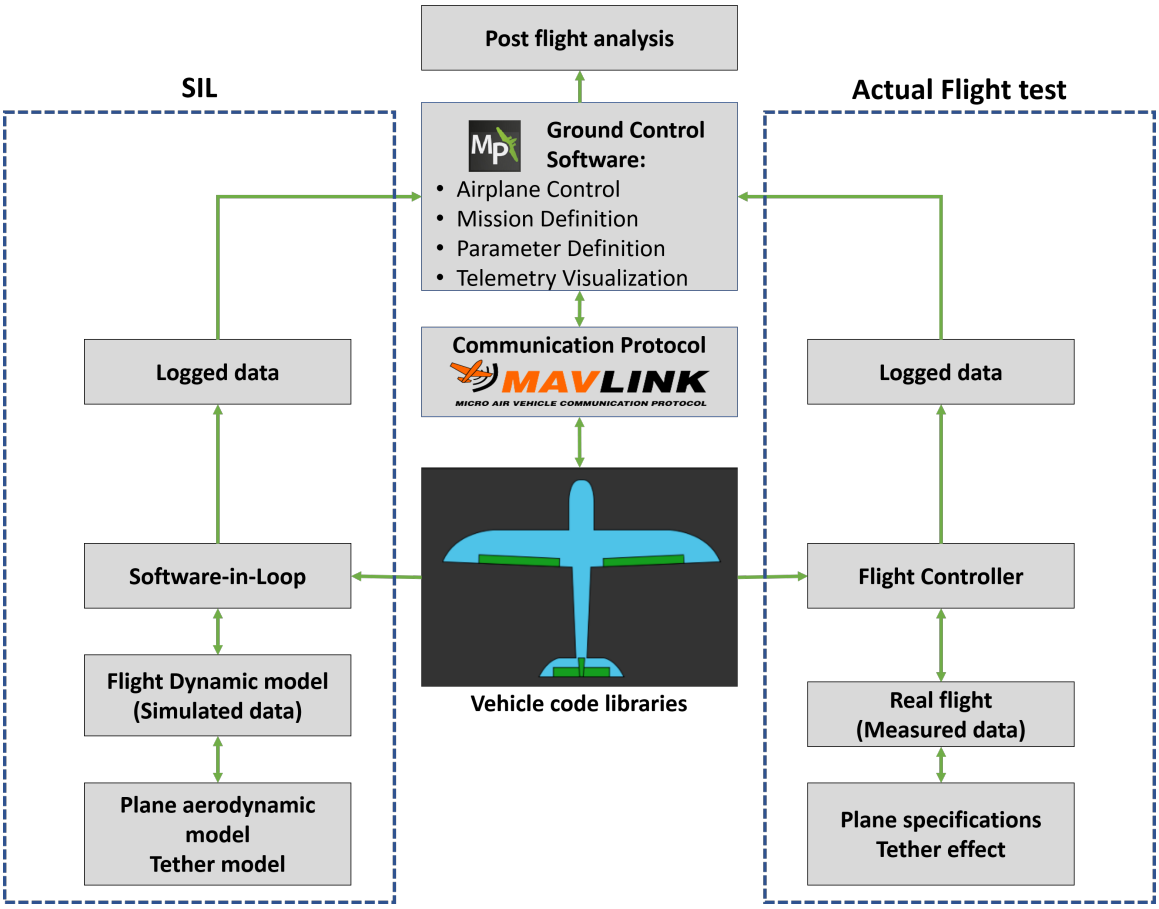

Figure 4.1: `Ardupilot` architecture

.

4.2.1 Flight controller hardware and `Ardupilot` alternative

The Pixhawk 4 flight controller was developed in collaboration with the PX4 team. Similar to the `Ardupilot`, the PX4 is an open-source flight control platform [42]. They both have similar architectures, operate with flight controller parameter definition, can be operated with the same ground control software, and have similar flight modes. However, each platform requires a different servo and motor wiring, and have different configuration procedures. Another main difference is the open-source licences. The Ardupilot oblige whoever uses the platform for commercial purposes to make their modifications open to the public, whereas the PX4 allows the user to own their code modifications and have them closed to the public. Each code has its airframe firmware, both including the quadplane. The main reasons the `Ardupilot` was selected over the PX4 for this project were: First, the AWEsome code has already been developed in the `Ardupilot` platform and it was convenient to have for reference and as a

starting point. Second, the SIL files are more accessible and can be easily modified to incorporate the tether model. Third, the `Ardupilot` provides a data logging system that allows conversion of the files to a convenient post-processing format such as MATLAB, with the `Ardupilot`, the SIL simulation results and flight test results could be easily analyzed and compared. Finally, the flight mission could be defined in a convenient `.txt` file format with a series of waypoints, allowing to easily upload crosswind flight trajectories to the flight controller.

4.3 The `Ardupilot` platform for Airborne Wind Energy operation

The `Ardupilot` code was first used for AWES with a fixed-wing glider in the AWEsome project (Airborne Wind Energy Standardized Open-source Model Environment). It was developed at Bonn University as part of a Master's thesis [27, 43]. The plane code was modified creating fixed-length circular and figure-eight flight paths as new flight modes. The trajectory is geometrically defined and projected into the surface of a sphere that represents the tether length. The reference flight path can be easily changed to the desired dimension (e.g. increase the radius of the circle projected on the sphere), still maintaining constant tether length during flight. While in one of these modes, the plane follows waypoints continuously generated along the path at a rate of 50 Hz. The developed model was validated with an off-the-shelf model RC plane of 1366 mm wingspan reinforced for tethered flight. With the `Ardupilot` code uploaded into the flight controller, the plane was able to complete a fully autonomous tethered figure-8 flight as prescribed in the trajectory. The plane was tethered with a line to a fishing rod that was reeled manually, and during AWES flight mode the tether length was kept constant. The take-off and landing phases were performed manually by a pilot in fixed-wing mode (horizontal take-off). The AWEsome code provided the foundation to allow this project to tackle the remaining challenges: automate the take-off and landing withVTOL hardware, follow any used-defined trajectories, either pumping, or fixed tether length, automate the tether reeling operation with a ground station motor, and fully automate the AWES flight plan.

4.4 Quadplane Flight Controllers

Depending on the quadplane current flight mode it will use the plane or the quadcopter controls. Using either the control surfaces (aileron, elevator, rudder) and front motor, or VTOL motors. A common flight plan involves: vertical take-off, hover, transition to forward flight, crosswind flight, transition into hover, and land vertically. Therefore all controllers will be implemented during flight. The plane has three levels of controls: trajectory tracking and waypoint navigation, speed and height, and attitude control. On the other hand, the quadcopter control is separated into position and attitude controller. Both control architectures work together during the transitions from hovering to forward flight and back.

4.4.1 Fixed-wing trajectory tracking and navigation controller

The L1 navigation controller is based on [38], which names L1 the vector from the aircraft to the reference point. It uses the angle between the plane instantaneous inertial speed and the vector pointing to the reference target point to estimate the lateral acceleration needed to follow a circular reference trajectory as seen in Figure 4.2. Some parameters, such as the waypoint radius (WP_RADIUS), are used to smooth or sharpen the trajectory of the plane. A higher radius will adjust the L1 vector and inform the plane that it has reached the waypoint earlier, turning to align itself with the next target.

4.4.2 Fixed-wing speed and height controller

The speed and height of the aircraft are controlled by the Total Energy Control System (TECS) controller, which calculates the total energy as a sum of potential and kinetic energy based on the actual and demanded speed and height. It provides a throttle and pitch angle command that balances the total energy at all times. A properly tuned TECS controller is essential for accurately following a AWES flight mission. The TECS_SPDWEIGHT parameter, distributes the weight of the speed and height errors for the kinetic and potential energy calculation. This parameter is key for flight missions with highly fluctuating heights (such as crosswind flight). A higher value will ignore the height error causing the plane to glide smoothly instead of diving into the lower altitude waypoints.

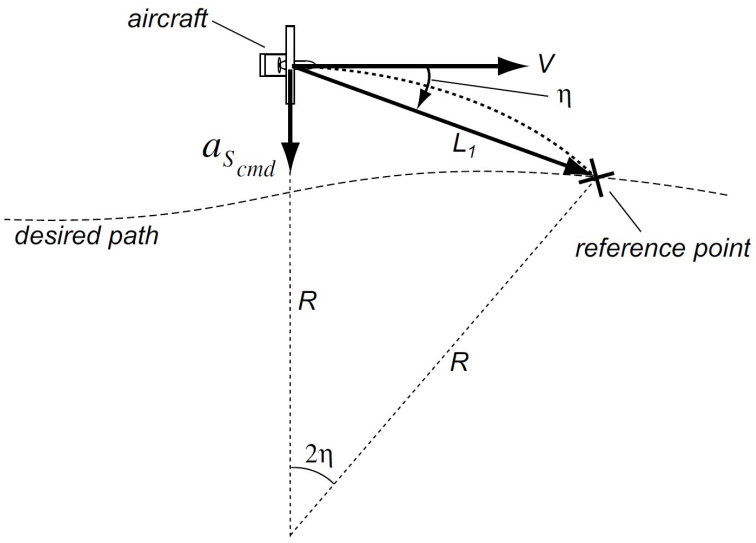

Figure 4.2: `Ardupilot` non-linear guidance logic for trajectory tracking

4.4.3 Fixed-wing attitude controller

The plane roll, pitch, and yaw angles are obtained from the control surfaces actuators aileron, elevator, and rudder respectively. Individual Proportional Integral Derivative (PID) controllers along with additional gains such as turn compensation, airspeed gains, and angle saturation are applied to the error between the commanded and the actual angle, to calculate the control surface deflection as seen in Figure 4.3 [44]. The PID gains can be tuned either manually for specific flight mission and plane specifications, or by using the autonomous flight mode AUTOTUNE, which will record the new gains from commanding limiting angles and evaluating the plane response.

4.4.4 Quadcopter position and attitude controller

The quadcopter control is divided into two levels. The position control on the left block of Figure 4.4 calculates the target roll and pitch angles that the quadcopter would require to move from the current position to the target position. The velocity is calculated from the position error through a proportional controller, and then is compared with the actual velocity. Finally, a PID control is applied to the velocity error to obtain the target angles. Similarly, the attitude controller uses a PID strategy to estimate the required motor output to match the target angles or attitude of the quadcopter. The roll and pitch angular rates are estimated from the angle error

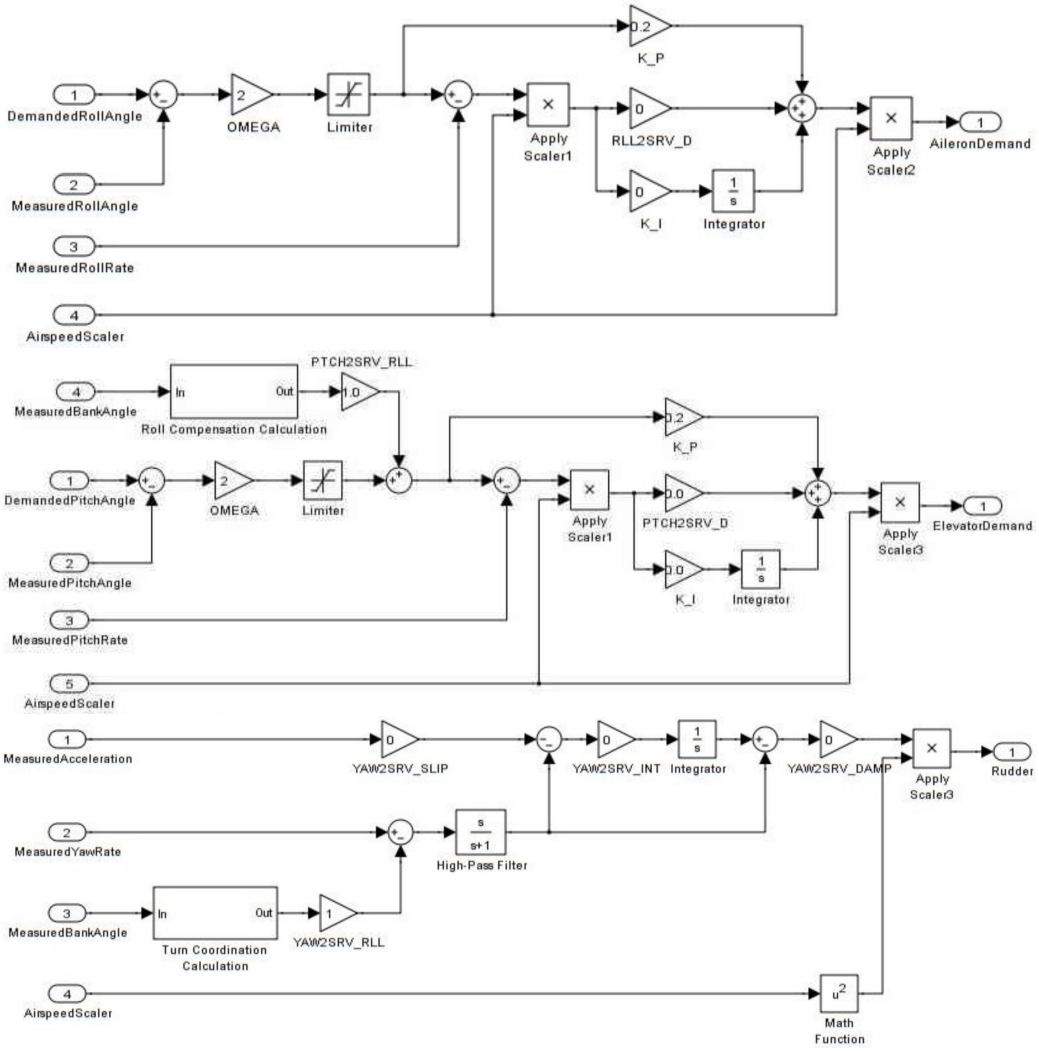

Figure 4.3: Ardupilot roll, pitch, and yaw PID controllers

through a proportional controller, the difference with the actual rates pass through a PID controller resulting in the required motor output.

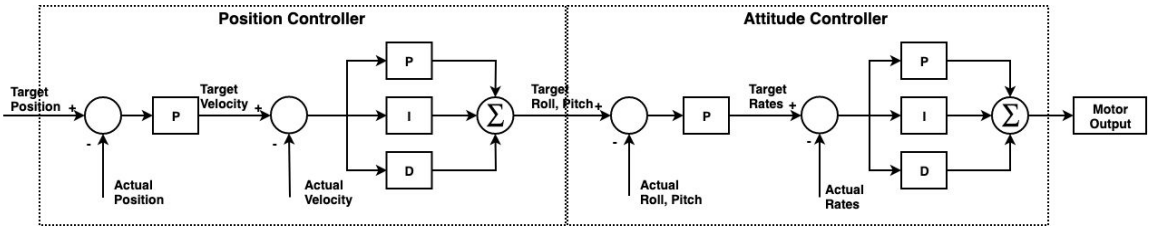

Figure 4.4: Quadcopter flight controller diagram

.

4.4.5 Fixed-wing and quadcopter mode transitions

The transition from quadcopter to plane consists in keeping the plane hovering while the forward motor provides the thrust to reach the minimum transition airspeed. Transitioning back into hover mode provides a downward thrust with the quadcopter motors while slowing down the plane until reaching the transition speed. To achieve a seamless and smooth transitions from hovering to forward flight and back, the plane and quadcopter controls work together to meet a series of transition parameters. Among them is ARSPD_FBW_MIN which defines the transition speed. The Q_ASSIST_SPEED parameter defines the speed limit in which the quadcopter motors will provide thrust assistance while already in plane mode. Another key parameter is the Q_TRANSITION_MS ,which defines the time that the quadcopter motors take to ramp the throttle up/down after reaching the transition speed, this ramping time prevents sudden changes in altitude during the transition.

4.5 Navigation strategy

Autonomous flights consist in setting the plane in specific flight modes, one of them is the AUTO mode which allows the plane to follow a predefined flight mission which can include take-off and landing. Other useful autonomous flight modes are the LOITER, RTL, QHOVER, and QRTL. These commonly used flight modes are listed in Table 4.1. Modes starting with “Q” represent quadplane flight modes and often require the vertical motors for operation. Finally, the modes LOITER_3D and EIGTH_SPHERE represent the circle and figure-8 created in the AWEsome project.

Table 4.1: List of `Ardupilot` common flight modes

Flight mode	**Description**
AUTO	Follow a mission comprised of a set of waypoint and commands
LOITER	Circle arround the point where the mode was entered maintaing the current altitude
RTL	Return to the lauch location and loiter arround it
QHOVER	Maintains the quadplane altitude while still allowing roll and pitch commands
QRTL	Return to the launch location and hover over it maintaining the altitude
QAUTOTUNE	Performs autonomous step rotations in the pitch, roll, and yaw axis to record new PID gains based on the quadplane response.
LOITER_3D	Performs a constant length crosswind ellipse
EIGTH_SPHERE	Performs a constant length crosswind figure-8

To perform a specific AWES flight mission there are two possible approaches. The first option is setting the plane flight mode to one of the AWEsome flight modes available, this will command the plane to follow an inclined ellipse or figure-8. A second option is to define a series of waypoints in terms of latitude, longitude, and altitude. Either way, to automate the process, the flight mission must be defined prior to flying, including the take-off and landing phase. For example, a simple quadplane mission would involve taking-off vertically up to a certain altitude, transition from hovering to forward flight, following a trajectory defined by a series of waypoints, transitions back into hovering, and landing vertically.

Chapter 3 defined as a series of points in the global coordinates (X, Y, Z). Knowing the 3D trajectory allows to convert the points into the format required for the `Ardupilot` mission (lat, lon, alt). To achieve this, the area to be converted is assumed as small enough that the relationship between the geographic angles and flat distance is linear. The change of latitude and longitude can be obtained from a reference distance in kilometers, corresponding to a reference angle in the geographic coordinates.

Two reference points are separated 100 m to the North, and 100 m to the East of the "home" location or origin, the geographic coordinates to these points are compared to the origin obtaining the change in geographic angle. This relation is used to find the change in longitude for a series of points in the X direction, and the change in latitude for a series of points in the Y direction. Considering that the converted area is very small, it can be assumed that the series of points in the Z direction are directly used as the altitude points. This process can convert any 3D trajectory from (X, Y, Z) points to a local (lat, log, alt) coordinates knowing the geographic origin. Table 4.2 present the point to coordinate conversion for a constant tether length circular trajectory. Figure 4.5 shows how the 3D points of the circular trajectory over the surface of the sphere (constant tether length) are converted into geographic coordinates input to the flight mission.

For completion sake, Figure 4.6 represents the 3D trajectory conversion for a pumping mode flight mission.

Table 4.2: Trajectory points to geographic coordinate conversion

X (m)	Y (m)	Z (m)	lat (deg)	lon (deg)	alt (m)
0	0	0	48.56586	-123.39114	0
77.14	50.00	77.14	48.56631	-123.39009	77.14
98.10	40.26	56.17	48.56622	-123.38981	56.17
110.90	14.85	43.38	48.56599	-123.38964	43.38
110.55	-16.35	43.73	48.56571	-123.38964	43.73
97.18	-41.18	57.09	48.56549	-123.38982	57.09
76.01	-49.97	78.26	48.56541	-123.39011	78.26
55.28	-39.30	98.99	48.56551	-123.39039	98.99
43.06	-13.32	111.21	48.56574	-123.39056	111.21
44.11	17.84	110.16	48.56602	-123.39054	110.16
58.02	42.06	96.25	48.56624	-123.39035	96.25

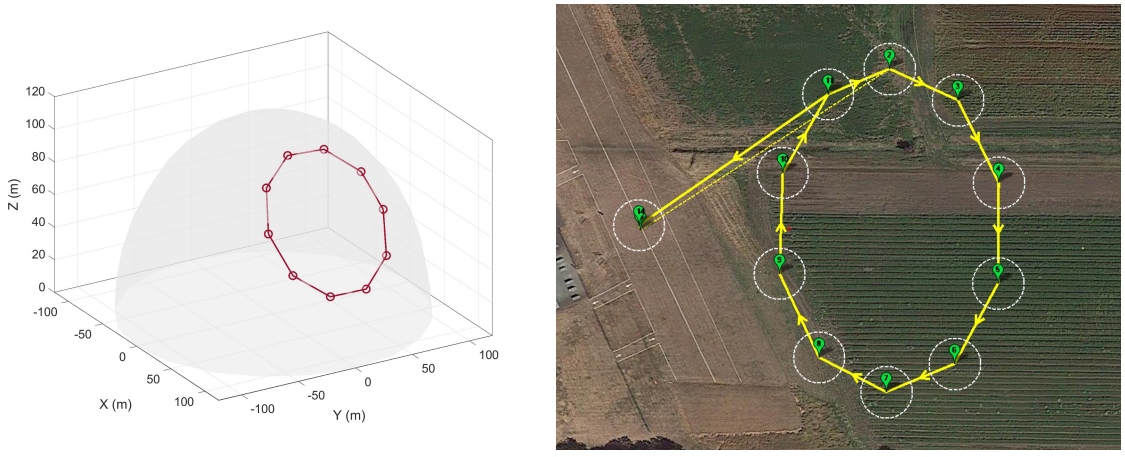

Figure 4.5: Fixed tether length trajectory points and converted geographic coordinates

.

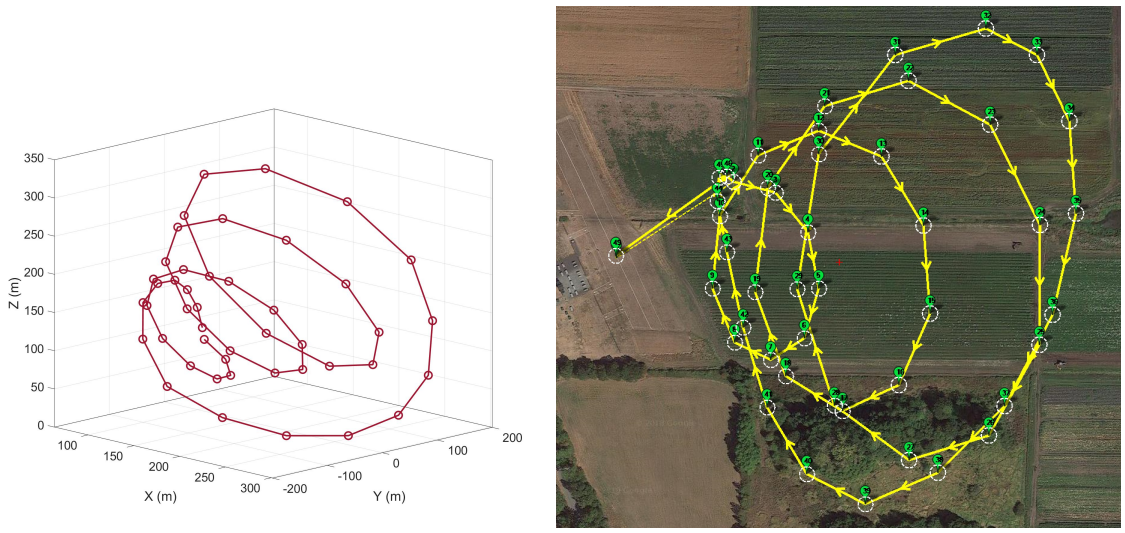

Figure 4.6: Pumping mode trajectory points and converted geographic coordinates
.

4.6 Software-in-Loop Simulation

The Software-in-Loop (SIL) provides an invaluable tool for debugging and troubleshooting the flight code in a simulated environment. It compiles the vehicle code and runs it without requiring any hardware, allowing to verify the plane operation before uploading the code into the hardware. The SIL uses the same messaging protocol as the hardware, therefore it communicates with a ground station software as if the vehicle was connected. The sensor data, such as airspeed, linear and angular accelerations, actuator deflection, GPS, and motor signals, are generated by the flight dynamics model present in the "SITL" file folder under the `Ardupilot` library files. The simulation and plane parameters are defined by MAVLink commands or through the ground station software. Wind speed and direction are set with the SIM_WIND_SPD and SIM_WIND_DIR parameters. A benefit of using the SIL for troubleshooting is that the entire simulation can be sped-up to 3 times faster than a real flight, accelerating the process of trying different parameters and configurations.

The Ardupilot platform allows reviewing the measured and estimated flight data through a log file. During the SIL simulation the data is also recorded as if the plane was performing a real flight. The variables in the log files are separated by identifiers that are written following the order in which they are recorded. Depending on the sensor, the data is recorded at different frequencies. The ground station software provides a tool for directly analyzing the log files. However, to use the data for further post-analysis all the identifiers must be spaced to the same frequency and matched so that the time difference from each record is small enough to be neglected. Table 4.3 presents the variables recorded and the identifiers used the log files.

The ARSP presents the measured data from the airspeed sensor. CTUN and QTUN identifiers provide information about the forward and vertical throttle respectively. GPS records the latitude, longitude, and altitude of the plane. IMU records the linear accelerations and rotational rates. NTUN provides the navigation information such as target latitude, longitude, and altitude. AHRS give the plane's heading orientation. NKF1 correspond to the Extended Kalman Filter and estimates the Euler angles pitch, roll, and yaw, the velocity vector, and the position of the plane in the North-East-Down (NED) reference frame.

Table 4.3: Ardupilot log file variables

Identifier	**Variables**
ARSP	Airspeed, DiffPress
CTUN	ThrOut, ThrDem
GPS	Lat, Lon, Alt
IMU	GyrX, GyrY, GyrZ AccX, AccY, AccZ
NKF1	Roll, Pitch, Yaw VN, VE, VD PN,PE, PD
NTUN	Tlat, Tlon, Talt
QTUN	ThO

The quadplane flight model splits into the rigid-wing plane and quadcopter physics models. During take-off and landing, the quadcopter controls take over commanding the throttle of each of the vertically mounted motors. The pitch, roll, and yaw angles are then achieved by the difference in thrust output from the motors allowing the plane to maneuver while hovering. During forward flight the plane attitude is controlled using the aileron, elevator, and rudder deflection. Either way, the physics model calculates the forces and moments acting on the quadplane, and consequently the state of the vehicle, feeding it into the plane code where the controls algorithms decide the actuator commands. Most of the work regarding tethered flight is performed in the physics model. The tether effect is directly included in the plane dynamics as forces acting on the CG, therefore for the sake of clarification, the body force equations are described in the following sections.

4.6.1 Plane physics model

The plane dynamics are obtained from a linearized 6 DOF aircraft model that implements the stability derivatives to calculate the forces and moments acting on it. The aerodynamic lift in Equation 4.1 behaves linearly for small angles of attack, and drag coefficient in Equation 4.2 is defined with the Oswald efficiency.

$$C_L = C_{L_0} + C_{L_{\alpha 0}}\alpha \tag{4.1}$$

$$C_D = C_{D_0} + \frac{C_L^2}{\pi e_0 AR} \tag{4.2}$$

With the apparent wind speed V_e, and air density ρ the dynamic pressure $\bar{q}$ is calculated with:

$$\bar{q} = \frac{1}{2}\rho V_e^2 \tag{4.3}$$

The rolling, pitching, and yawing moment $(\bar{L}, \bar{M}, \bar{N})$ in Equation 4.4 are a function of the plane rotational rates P, Q, R obtained from the gyroscope measurement, along with the plane parameters (aerodynamic chord c, wingspan b, and wing area S), the control surface deflections (ail, ele, rud), the airspeed V_e, the corresponding stability derivatives, and side-slip angle β.

$$\begin{pmatrix} \bar{L} \\ \bar{M} \\ \bar{N} \end{pmatrix} = \bar{q}S \begin{pmatrix} b\Big(c_{l0} + c_{lb}\beta + \frac{b}{2V_e}\big(c_{lp}P + c_{lr}R\big) + \Delta c_{la}(ail) + \Delta c_{lr}(rud)\Big) \\ c\Big(c_{m0} + c_{ma}\alpha + c_{mq}Q\frac{c}{2V_e} + \Delta c_{me}(ele)\Big) \\ b\Big(c_{n0} + c_{nb}\beta + \frac{b}{2V_e}\big(c_{np}P + c_{nr}R\big) + \Delta c_{na}(ail) + \Delta c_{nr}(rud)\Big) \end{pmatrix} \tag{4.4}$$

The aerodynamic forces acting on the body axis $(\bar{F}_{ax}, \bar{F}_{ay}, and \bar{F}_{az})$ in Equation 4.5 are calculated by rotating the aerodynamic coefficients from the wind axis to the body axis as presented in Equation 4.6. Lastly, the angle between the apparent wind speed and the forward body axis is defined as the angle of attack α.

$$\begin{pmatrix} \bar{F}_{ax} \\ \bar{F}_{ay} \\ \bar{F}_{az} \end{pmatrix} = \bar{q}S \begin{pmatrix} c_{xa} + c_{xq}Q\big(\frac{c}{2V_e}\big) - \Delta C_{D_e}\cos(\alpha)(ele) + \Delta C_{L_e}\sin(\alpha)(ele) \\ c_{y0} + c_{yb}\beta + \frac{b}{2V_e}\big(c_{yp}P + c_{yr}R\big) + \Delta c_{ya}(ail) + \Delta c_{yr}(rud) \\ c_{za} + c_{zq}Q\big(\frac{c}{2V_e}\big) - \Delta C_{D_e}\sin(\alpha)(ele) - \Delta C_{L_e}\cos(\alpha)(ele) \end{pmatrix} \tag{4.5}$$

$$\begin{pmatrix} c_{xa} \\ c_{xq} \\ c_{za} \\ c_{zq} \end{pmatrix} = \begin{pmatrix} -C_D\cos(\alpha) + C_L\sin(\alpha) \\ -C_{D_q}\cos(\alpha) + C_{L_q}\sin(\alpha) \\ -C_D\sin(\alpha) - C_D\cos(\alpha) \\ -C_{D_q}\sin(\alpha) - C_{L_q}\cos(\alpha) \end{pmatrix} \tag{4.6}$$

The thrust depends on the mounting direction of the onboard propulsion. For rigid-wing planes it is aligned with the body x-axis as presented in Equation 4.7

$$\begin{pmatrix} \bar{F}_{Tx} \\ \bar{F}_{Ty} \\ \bar{F}_{Tz} \end{pmatrix} = \begin{pmatrix} Thrust \\ 0 \\ 0 \end{pmatrix} \tag{4.7}$$

Finally, the total forces acting on a tethered plane are given by the sum of aerodynamic, thrust and tether forces.

$$\begin{pmatrix} \bar{F}_x \\ \bar{F}_y \\ \bar{F}_z \end{pmatrix} = \begin{pmatrix} \bar{F}_{ax} + \bar{F}_{Tx} + \bar{F}_{tx} \\ \bar{F}_{ay} + \bar{F}_{Ty} + \bar{F}_{ty} \\ \bar{F}_{az} + \bar{F}_{Tz} + \bar{F}_{tz} \end{pmatrix} \tag{4.8}$$

4.6.2 Tether model

A simplified way to model the effect of the tether on the plane's flight is to represent it as an elastic rod, as seen in similar AWES prototype project [26]. The model is incorporated in the `SIM_plane.cpp` file under the "SITL" folder in the `Ardupilot` libraries folder. The tether force is comprised of the weight, aerodynamic drag, and tension, as presented in Equation 4.9. For the tension, the tether elastic constant K_t changes over time depending on the tether length l_t, elongation at breaking point ϵ_t, and breaking load $F_{t,max}$ (Equation 4.10).

$$\begin{pmatrix} \bar{F}_{tx} \\ \bar{F}_{ty} \\ \bar{F}_{tz} \end{pmatrix} = \begin{pmatrix} \bar{F}_{tension,x} + \bar{F}_{drag,x} + \bar{F}_{W,x} \\ \bar{F}_{tension,y} + \bar{F}_{drag,y} + \bar{F}_{W,y} \\ \bar{F}_{tension,z} + \bar{F}_{drag,z} + \bar{F}_{W,z} \end{pmatrix} \tag{4.9}$$

$$K_t = \frac{F_{t,max}}{\epsilon_t l_t} \tag{4.10}$$

The magnitude of the tether tension force acting on the plane is obtained from Equation 4.11. It is a function of elongation (ΔX), generated from substracting the reference tether length l_t to the actual tether length l_p. The first is known from the programmed length at the GS, and the latter is obtained from the plane's current position in a ground reference frame (X_p, Y_p, Z_p) calculated with Equation 4.12. The tether force also acts as a physical constraint, where for a specific tether length the force will continue to increase as it elongates, to the point where it becomes bigger than the total aerodynamic force pulling the plane towards the GS. On the other hand, if the position of the plane is closer to the GS than the tether length, there is no tension applied to the plane.

$$F_{t,tension} = K_t(l_p - l_t) \tag{4.11}$$

$$l_p = \sqrt{X_p^2 + Y_p^2 + Z_p^2} \tag{4.12}$$

The tether force is applied on the plane's CG always pointing toward the GS location. The magnitude of the force is calculated in the ground reference frame and then rotated to the body reference frame through the rotation matrix R using the plane Euler angles roll (ϕ), pitch (θ), and yaw (ψ).

$$R = \begin{pmatrix} cos(\theta)cos(\psi) & cos(\theta)sin(\psi) & -sin(\theta) \\ -cos(\theta)sin(\psi) + sin(\phi)sin(\theta)cos(\psi) & cos(\phi)cos(\psi) + sin(\phi)sin(\theta)sin(\psi) & sin(\phi)cos(\theta) \\ sin(\phi)sin(\psi) + cos(\phi)sin(\theta)cos(\psi) & -sin(\phi)cos(\psi) + cos(\phi)sin(\theta)sin(\psi) & cos(\phi)cos(\theta) \end{pmatrix} \tag{4.13}$$

The drag force resulting from the tether can be estimated using the total angular momentum of tether, integrating over the entire length, as presented in [45]. The resulting force that generates the momentum is expressed in Equation 4.14, where $C_{D,t}$ is the tether drag coefficient and A_t the tether front projected area.

$$F_{t,drag} = -\frac{\rho C_{D,t} A_t cos(\alpha) |\bar{V_e}|^2}{8} \left(- \frac{\bar{V_e}}{|\bar{V_e}|} \right) \tag{4.14}$$

Lastly, the tether weight is a function of its length L_t with $m_{t,l}$ the tether mass per unit length. This force is always parallel to the Z direction in the NED coordinate system, therefore it requires to be defined in body axes using the rotation matrix.

$$F_{t,W} = m_{t,l} l_t g \tag{4.15}$$

4.6.3 Quadcopter model

The physics model of the quadcopter is relatively simple in comparison to a fixed-wing plane. The flight entirely depends on the thrust generated by the motors when changing their rotational speed. The body forces in Equation 4.16 are a sum of the motor thrust T_M. The moments in Equation 4.17 are the individual thrust multiplied by the arm length L_{arm}. The quadcopter moves in space by rotating along one of its axis which generates a side force when the thrust is decomposed into vertical and horizontal components. Finally, the tether loads described in inertial coordinates are applied as body forces on the CG through the rotation matrix R (Equation 4.13.

$$\begin{pmatrix} F_{qX} \\ F_{qY} \\ F_{qZ} \end{pmatrix} = \begin{pmatrix} 0 \\ 0 \\ T_{M1} + T_{M2} + T_{M3} + T_{M4} \end{pmatrix} \tag{4.16}$$

$$\begin{pmatrix} M_{qX} \\ M_{qY} \\ M_{qZ} \end{pmatrix} = \begin{pmatrix} (T_{M2} + T_{M4})L_{arm} \\ (T_{M1} + T_{M3})L_{arm} \\ M_{M1} + M_{M2} + M_{M3} + M_{M4} \end{pmatrix} \tag{4.17}$$

4.7 Results and Discussion

This section analyzes the results from various SIL simulations performed with different flight missions. First, a VTOL waypoint flight plan is performed to evaluate the tether drag and weight model. Second, the tether tension model is assessed by implementing a figure-8 trajectory for a range of wind speeds. Third, the quadplane trajectory tracking performance is evaluated using an ideal winch model. Lastly, the onboard power consumed is compared with the potential power production for specific crosswind trajectories. The data recorded in the log files is converted into MATLAB format and used for further analysis.

The plane used in the simulation is based on the Skywalker 2013 RC model aircraft. Its general specifications are presented in Table 4.4. Although the specifications are not the same as the hardware in Chapter 2, the `Ardupilot` allows to adapt the plane performance through the parameter file. What is required for the simulation is to describe the plane actual performance specifications such as, stall speed, trim speed, trim throttle, etc. The developed quadplane specifications can't be directly defined in the flight model, as the stability derivatives are not entirely known.

Table 4.4: General specifications of the model plane.

Wing area (m^2)	Wingspan (m)	Chord (m)	Weight (kg)
0.45	1.88	0.24	2

4.7.1 Vertical take-off and landing and tethered flight

Automating the entire simulation is achieved by incorporating a VTOL approach to the flight mission. The throttle profiles in Figure 4.8.a show the three phases of the mission. Between 50 and 100 seconds the quadcopter motors (orange curve) are

constantly active to vertically climb to the reference altitude of 100 m, when reached, the forward motor (blue curve) begins to provide thrust to transition into forward flight. Simultaneously, the quadcopter motors quickly reduce the throttle to zero. Transitioning back into quadcopter mode, the plane and quad propulsion systems work together; reducing and increasing thrust respectively. Finally, when the plane is positioned under the landing point, the quadcopter motors reduce the throttle under the hover throttle to control the descent into landing.

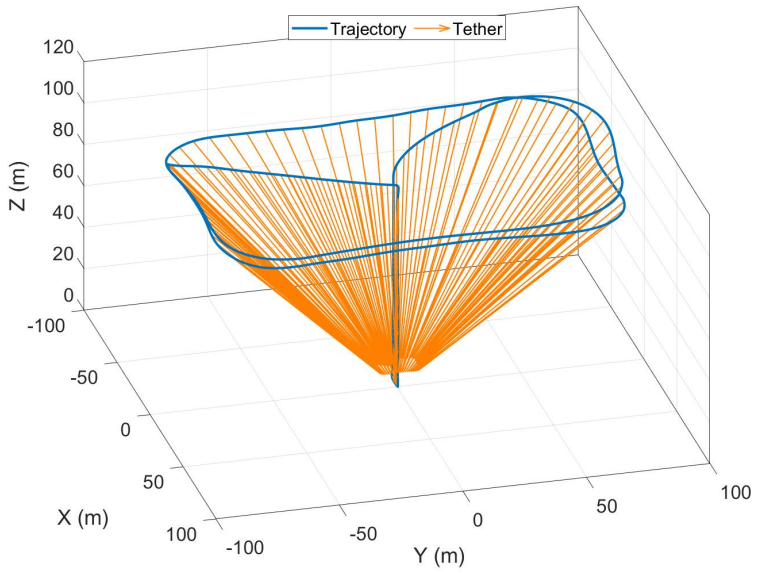

Figure 4.7: Resultant trajectory with representative tether

Throughout the mission, the plane was tethered to the ground station as represented with the orange curve in Figure 4.7, assuming that the winch can spin freely to avoid generating any tension. However, the weight and aerodynamic drag in Figure 4.8.b are present at all times. The apparent airspeed vector required to calculate the tether drag in Equation 4.14 can't be measured directly. However, it is obtained in the NED frame with Equation 4.18, and then rotated to the plane coordinate system with the rotation matrix in Equation 4.13. The resultant apparent wind speed vector is used to apply the drag force on the CG in the appropriate direction, the norm of the drag force is proportional to the airspeed square, and can be verified with the measured airspeed data.

$$\bar{V}_{e,NED} = \bar{V}_{wind} - \bar{V}_{plane,NED} \tag{4.18}$$

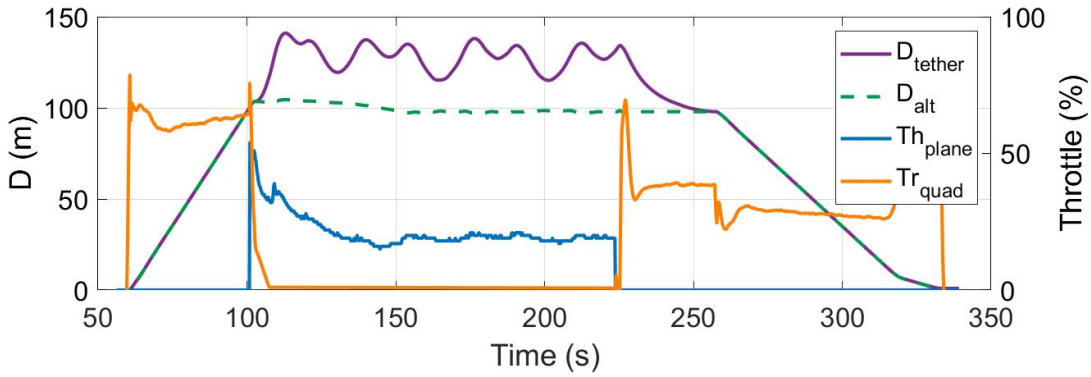

(a) Tether length, plane altitude, plane throttle (forward), and quadcopter throttle (downward).

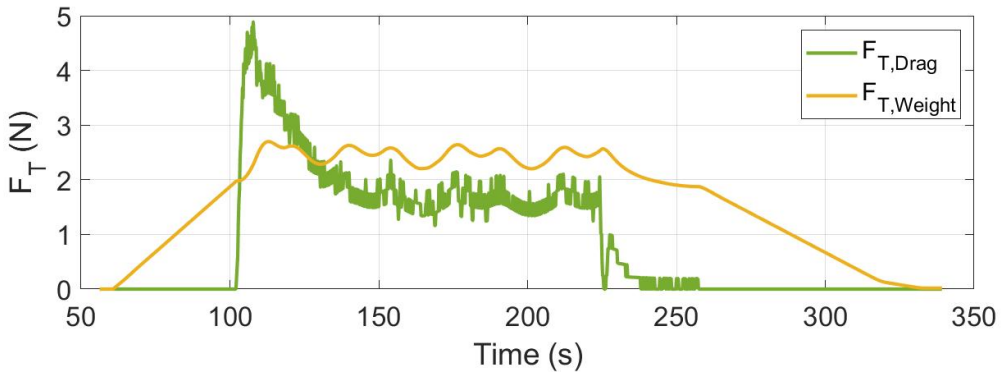

(b) Tether drag and weight forces.

Figure 4.8: Simulation results for tethered VTOL and forward flight with zero wind speed.

A parametric study shows the effect of the wind speeds on the aerodynamic drag generated by a 1.6 mm diameter tether. In Figure 4.9 the plane was set to circle the ground station at a 50 m altitude at a constant ground speed of 10 m/s, varying the wind speed (V_W) from 0 to 8 m/s in the X direction. This flight mission assess the drag of the tether while flying upwind and downwind. The initial drag force peaks represent the transition from hovering to forward flight, while the prolonged higher drag values represents the plane flying against the wind. In some cases, the drag force becomes smaller than the 2 N reference drag at 0 m/s wind speed, indicating that the tether is being pushed while traveling downwind.

For all the following SIL simulations the tether model is included in the flight dynamics. Also, for operational simplicity, all the future missions implement the VTOL approach.

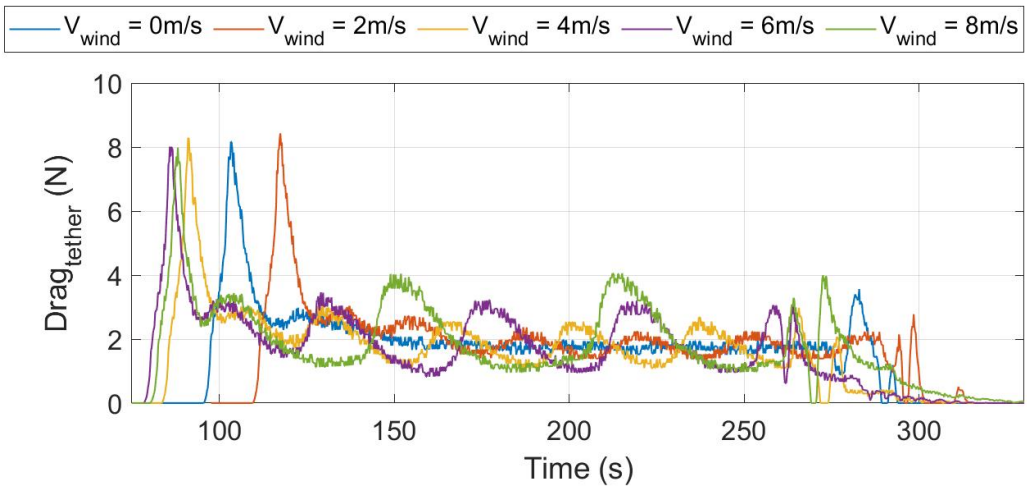

Figure 4.9: Tether drag for wind speeds of 0-8 m/s in the X direction.

4.7.2 Tether tension in crosswind flight

The tether model is evaluated by defining a flight mission that is projected on a sphere with a radius equal to the fixed tether length, and setting a range of wind speeds that allows crosswind flight. The tension applied on the plane is calculated using Equation 4.11 where l_p is the radial position of the plane, l_t is the maximum tether length set to 100 m, and K_t is the tether constant of elasticity which varies depending on the elongation generated by the plane's pull. The resulting tension pulls the plane towards the ground station balancing with the aerodynamic forces generated by the apparent wind speed.

The resulting trajectories from the 0 to 10 m/s wind speeds are presented in Figure 4.10, showing a significant deviation from the reference trajectory in all cases. The plane can enter and maintain crosswind flight for this specified trajectory with wind speeds higher than 4 m/s, maintaining a constant radial distance to the ground station. However, wind speeds higher than 10 m/s will prevent the plane to reach the waypoints along the curves of the figure-8 due to the high wind resistance. Moreover, increased wind speeds force the plane into a stable position with zero ground speed, sustaining flight due to the balance of forces in the tether direction.

The spring model produces tension forces only when the plane's radial distance to the GS is bigger than the maximum tether length. These tension peaks (T_{tether} in Figure 4.11) pull the plane toward the ground station causing a sudden decrease of its radial distance, consequently reducing the tension to zero. In reality, the physical

consequence would be a slack in the tether, that as soon as the plane passes the 100 m length gets taut and generate the high loads, possibly causing the plane to diverge from the reference trajectory. The implementation of a GS tension controller which allows the plane to successfully follow the pre-defined trajectory is investigated in Section 4.7.3.

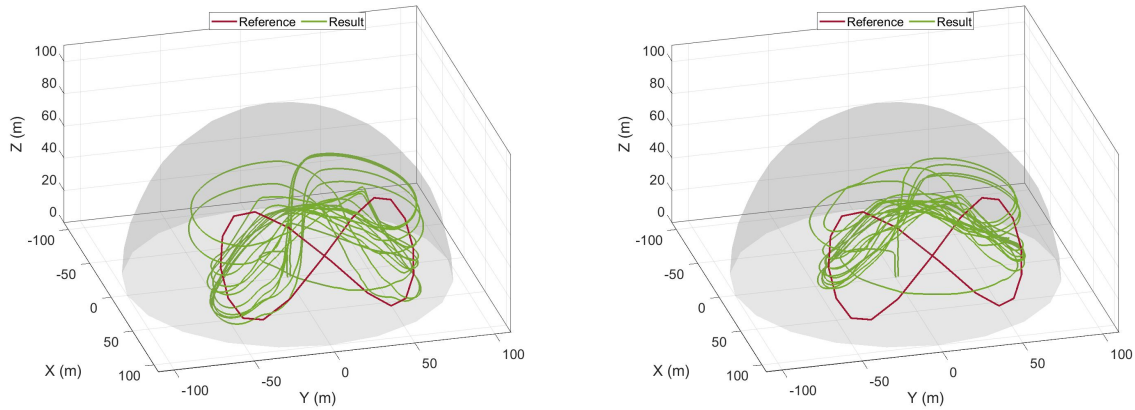

(a) 0 m/s

(b) 2 m/s

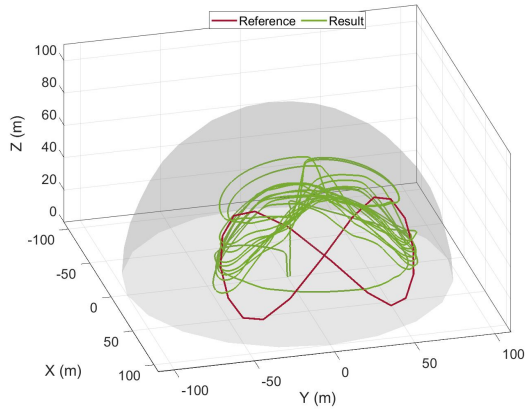

(c) 4 m/s

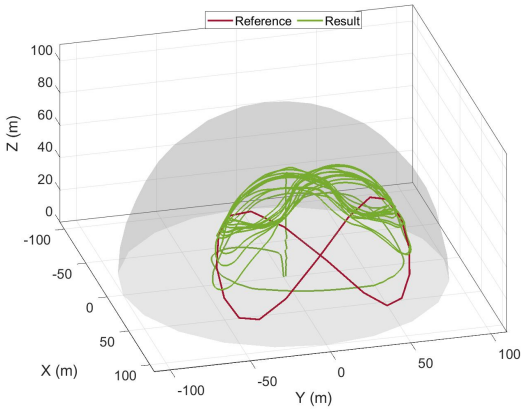

(d) 6 m/s

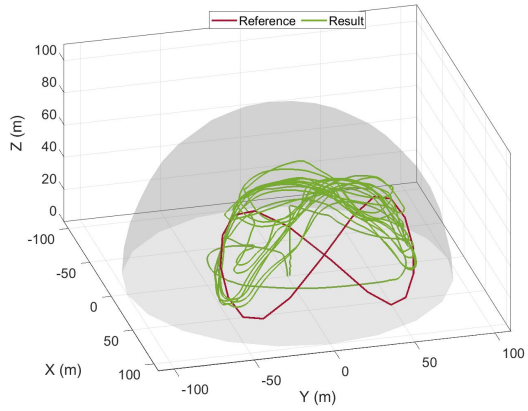

(e) 8 m/s

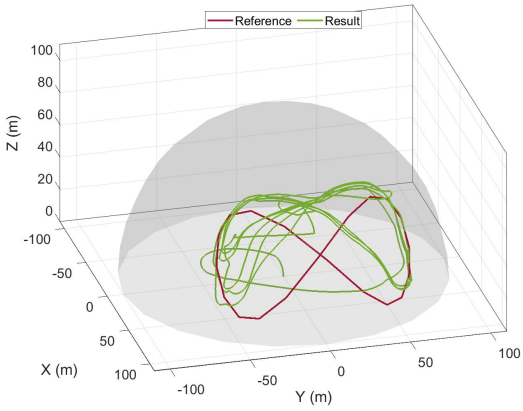

(f) 10 m/s

Figure 4.10: Resultant trajectories for $V_W = (0 - 10, 0, 0)$ m/s and GS at position (0, 0, 0)

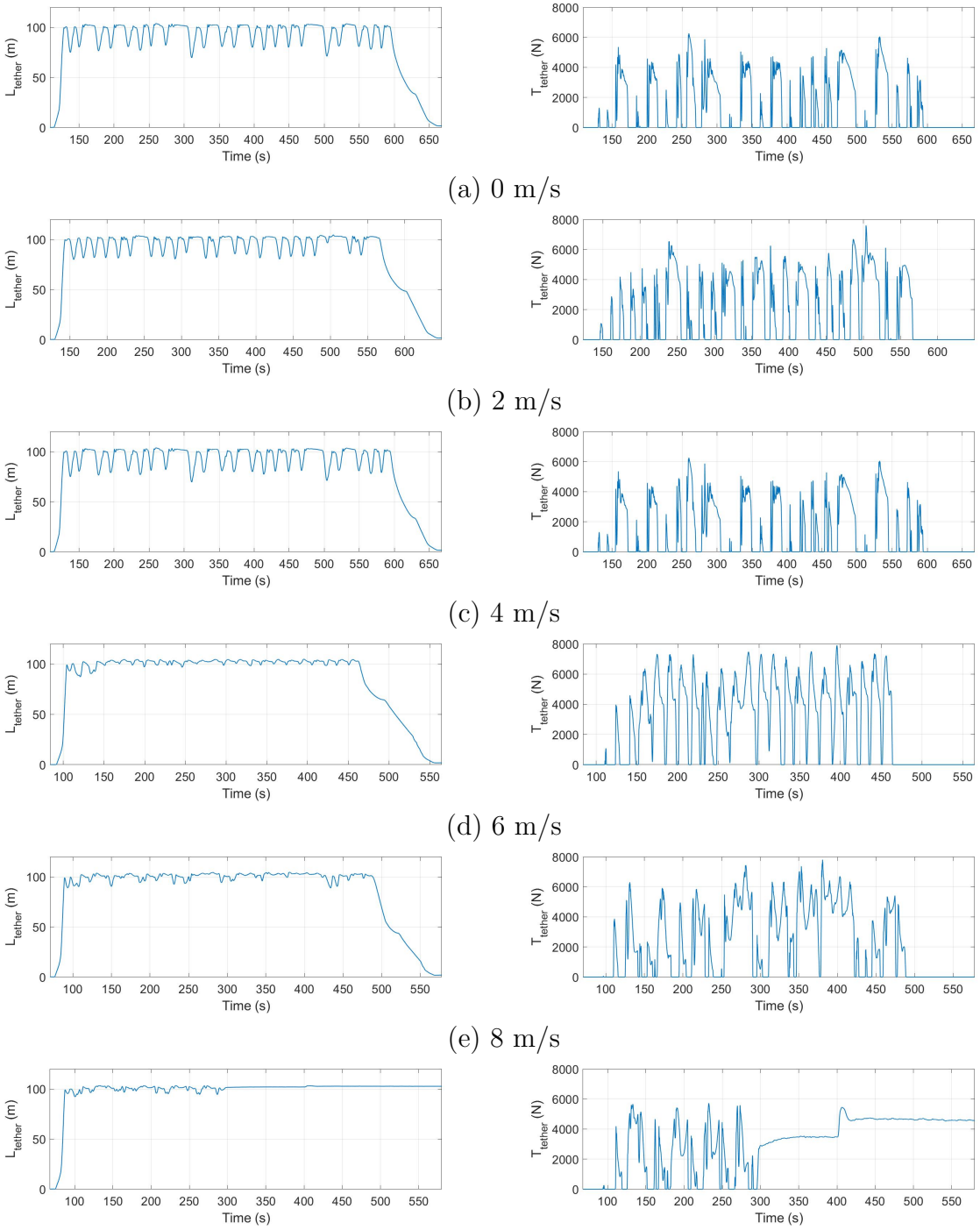

(a) 0 m/s

(b) 2 m/s

(c) 4 m/s

(d) 6 m/s

(e) 8 m/s

(f) 10 m/s

Figure 4.11: Resultant tether length and tension for $V_W = (0 - 10, 0, 0)$ m/s and GS at position (0, 0, 0)

4.7.3 Crosswind flight with ideal reeling control

The flight simulation was performed implementing an ideal ground station controller for following the pre-defined trajectory. AWES power generation depends on the quality of the wind resource since variation in wind speed generates oscillations in the tension, and therefore in the power output. One solution is implementing a reeling control that ensures constant torque on the generator, smoothing the tension peaks. For the circular and figure-8 trajectories, a constant tension of 15 N is continuously applied to the plane, thus, the tether length will no longer be fixed but will be continuously reeled in and out to maintain the tension.

Fixed tether length trajectory following

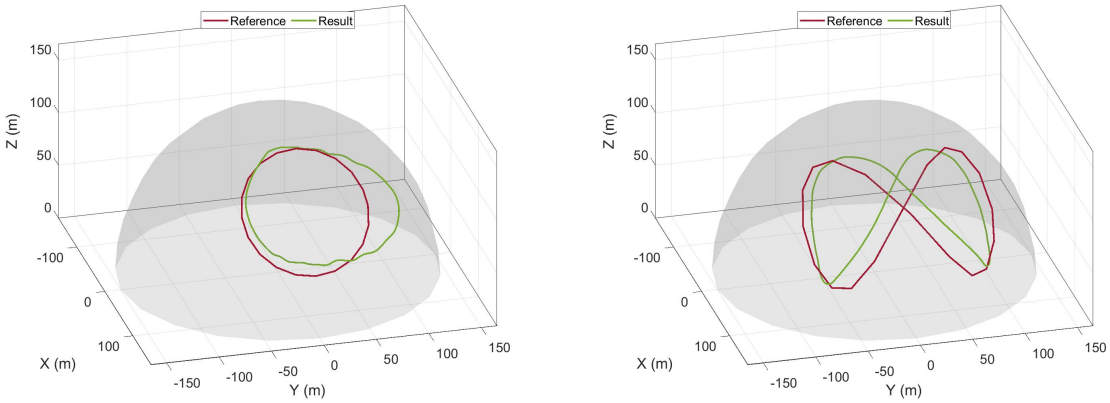

(a) Circle (b) Figure-8

Figure 4.12: Fixed tether length (150 m) trajectories, 7 m/s wind speed in X direction, ideal winch control of 15 N tension

The simulation was set-up with wind speeds of 7 m/s and a trajectory projected on a sphere with a 150 m radius. Figure 4.12 shows the reference trajectory, Figure 4.13 the target waypoints (latitude, longitude, and altitude), and Figure 4.14 the speed, throttle and attitude of the plane for one single loop. From the resultant 3D trajectory, a significant improvement can be noted in contrast to the fixed tether length from the previous section. The reference latitude, longitude, and altitude (red curve) show the waypoint that the flight controllers are targeting. Once the plane (green curve) is within a radius of 25 m from the target, it switches to the next waypoint successfully flying along the reference trajectory. This waypoint distance

allows some degree of relaxation on the flight controller and reduces the attitude change rate. Smaller waypoint radius produced high-frequency oscillations in the pitch and roll angles of the plane, while larger radius ignored the altitude changes.

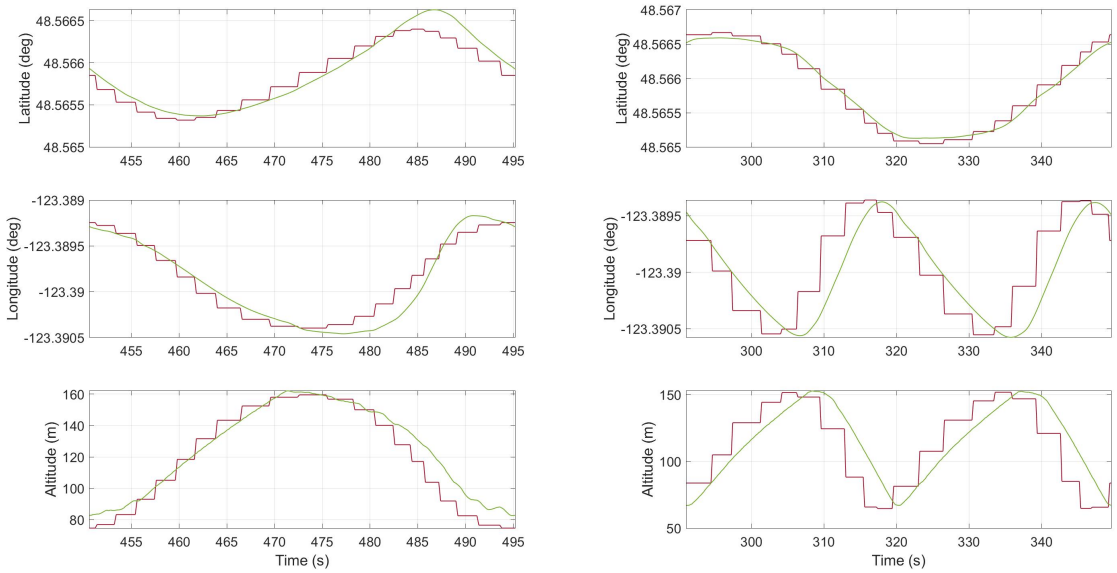

(a) Circle (b) Figure-8

Figure 4.13: Target and actual position in fixed tether length (150 m) trajectories, 7 m/s wind speed in X direction, ideal winch control of 15 N tension

The pitch results for the circular trajectory still presented oscillations while diving for the lower altitude waypoints, causing the navigation control to overshoot the reference latitude and deviate from the trajectory (still within the 25 m radius). This is not the case for the figure-8, where the pitch is roughly constant during climbing and diving switching from 30° to −40° on either case.

The energy efficiency of the cycle can be estimated based on the time that the forward propeller is providing thrust, represented as throttle in 4.14. Where for the circular trajectory the onboard propulsion is constantly providing thrust even on the diving maneuver, whereas for a figure-8 the throttle is completely shut-off for approximately 50% of the cycle. Turning off the throttle provides the opportunity for using the propellers as wind turbines and harness the apparent wind speed, consequently charging the battery or sending the electricity to the ground with a conductive tether.

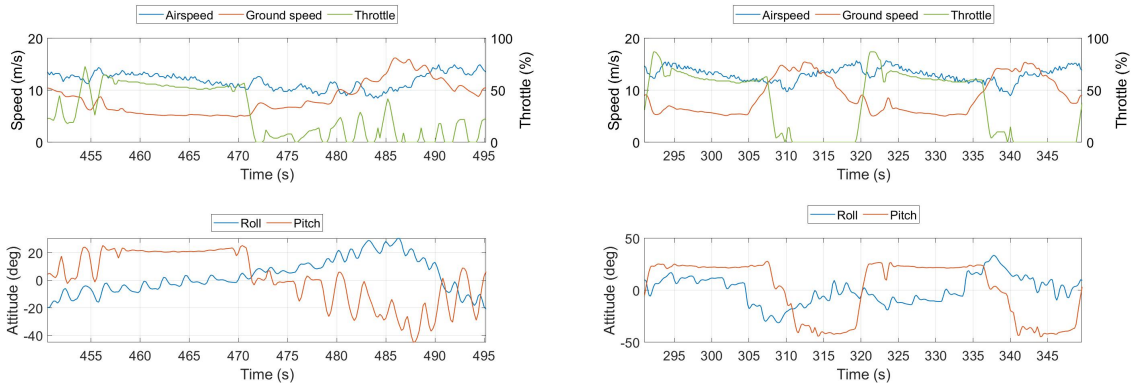

(a) Circle (b) Figure-8

Figure 4.14: Speed, throttle, and attitude in fixed tether length (150 m) trajectories, 7 m/s wind speed in X direction, ideal winch control of 15 N tension

Pumping mode trajectory following

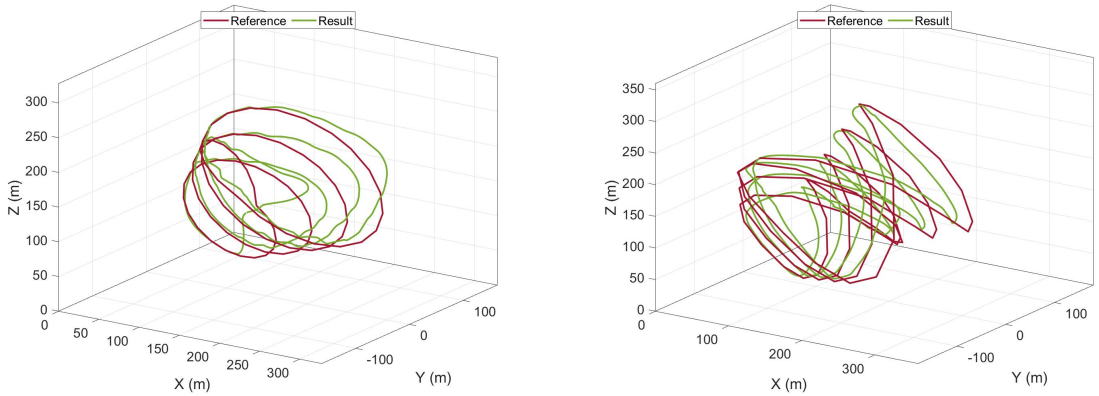

(a) Circle (b) Figure-8

Figure 4.15: Pumping mode trajectories with 7 m/s wind speed in X direction, ideal winch control of 15 N tension

Pumping mode navigation results are similar to the fixed radius trajectory. The main difference is that the plane follows a series of waypoints projected on a sphere that continuously increases its radius. The results in Figure 4.15 show trajectory, Figure 4.16 the target and actual position, and Figure 4.17 the speed and throttle along with tether length and reeling speed for one complete pumping cycle. For each reel-out loop, a similar performance to the fixed radius is presented, where the plane overshoots the latitude coordinate and continues to provide thrust throughout the

circular loop, while the figure-8 achieves to shuts down the propulsion during the diving sections of the loop.

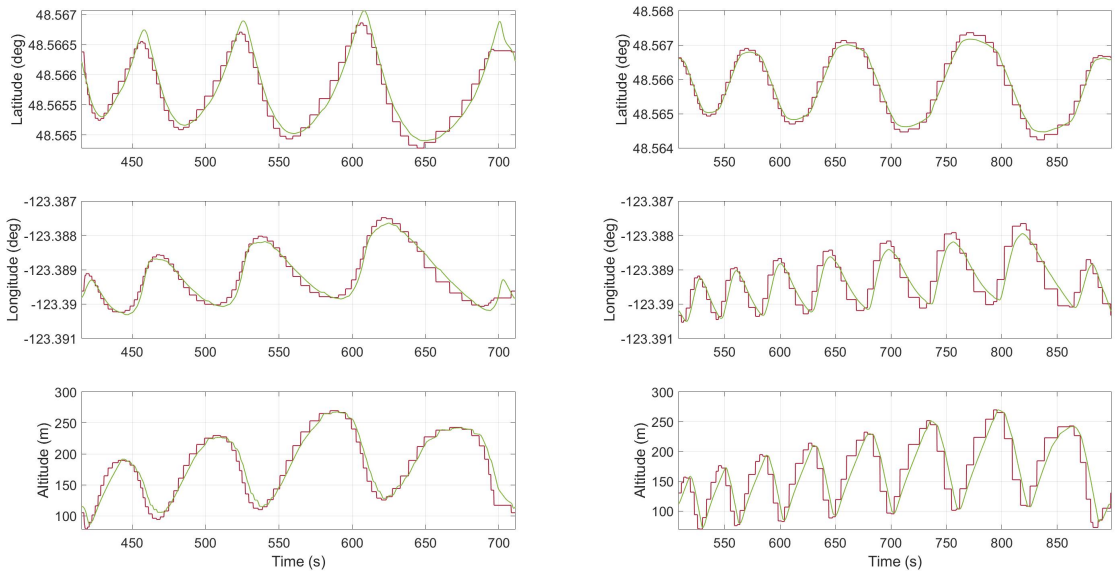

(a) Circle (b) Figure-8

Figure 4.16: Target and actual position in pumping mode with 7 m/s wind speed in X direction, ideal winch control of 15 N tension

To maintain positive power output during the reel-out phase, keeping a continuous positive reeling speed V_{tether} and tether tension is essential. From Figure 4.17, the reeling speed for both circle and figure-8 trajectories change reeling direction during the traction phase. This could be a consequence of low wind speeds, inappropriate tension set-point, un-tuned flight controller, or a combination. Future work should investigate the incorporation of the power generation condition to the TECS controller, where not only the pitch and throttle are regulated to meet the altitude targets, but also to generate enough aerodynamic force to balance the tether force, allowing either constant reel-out speed or constant traction force on the tether.

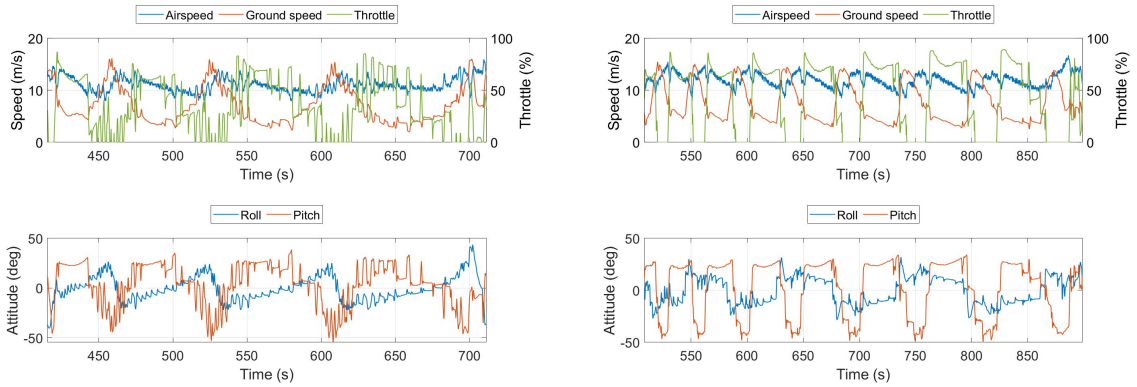

(a) Circle (b) Figure-8

Figure 4.17: Speed, throttle, tether length and reeling speed in pumping mode with 7 m/s wind speed in X direction, ideal winch control of 15 N tension

4.7.4 Power estimation

The plane model implemented for the simulation was not meant to generate power from crosswind flight. The goal is mainly tuning controls, evaluate the tether model, and try different trajectories for AWES operation. However, for the sake of completeness, the total power output of the system can be estimated by the difference in the generated and consumed power. For fixed tether length, the consumed power comes from the commanded throttle to keep the plane in the trajectory, while the generated power is assumed to be obtained from the same propulsion components operating as a turbine rotor. Furthermore, pumping mode generates and consumes power at the ground station depending on the reeling direction, and to the onboard propulsion to follow the defined mission.

$$P_{sys} = P_{gen} - P_{con} \tag{4.19}$$

For drag and pumping modes, the consumed onboard power is modeled as electric power proportional to the commanded throttle. In Equation 4.20, I_{max} represents the maximum current allowed by the motors, $V_{battery}$ is the operating battery voltage assumed constant throughout the flight, and the throttle given as a percentage.

$$P_{onboard} = V_{battery} \cdot I_{max} \cdot Throttle \tag{4.20}$$

Pumping mode power $P_{gen,trac}$ is directly calculated by the tether tension T_{trac} and reeling speed V_{reel} as in Equation 4.21. Maintaining a positive reeling speed during

retraction is critical for obtaining a net positive traction power.

$$P_{gen,trac} = T_{trac} \cdot V_{reel} \tag{4.21}$$

If the plane can to sustain crosswind flight without assistance of the onboard propulsion, meaning that no throttle is applied in the forward motor, it could potentially generate power in drag mode. The onboard motor and propeller system can be used inversely as a wind turbine, driven by the apparent wind speed on the plane. Making this assumption, the drag power generation $P_{gen,turb}$ is estimated using the Momentum Theory presented in Equation 4.22. The apparent wind speed V_e is used instead of the environment wind speed, and the coefficient of power is considered as Betz limit $C_p = 0.67$ for maximum power capture. This onboard generation model is strictly theoretical, as it does not consider the drag generated by the turbines mounted on the plane.

$$P_{gen,turb} = \frac{1}{2}\rho A_{prop} V_e^3 C_p \tag{4.22}$$

A simple control strategy is implemented to evaluate the effect of the tension set-point on the traction power generation ($P_{gen,trac}$) and onboard power consumption ($P_{cons,onb}$). The GS has two different tension values as a function of the reeling direction. The simulation was set up for 30 N of tension set-point when reeling out and a range from 0 to 30 N when reeling in. The same process was repeated with a 20 N tension for reeling-out. The power results are presented on Figure 4.18.

As expected, the plane reduced the onboard consumption with a higher retraction tension set-point due to the winch assist while flying upwind. The tension pulls the plane towards the GS allowing to reach the trim speed without the use of the front motor. However, the gain in onboard power consumption comes at a loss in the traction power generation, meaning that at this scale there is no significant improvement in terms of power production. For simplifying the hardware operation, the winch is set to maintain the same set-point for either reeling-in and out.

Extending these curves would allow obtaining the optimal traction control. However, the simulated plane cannot take any tension load over 30 N without deviating, or not achieving crosswind flight. The scaling of the system will determine if the platform allows net positive power cycles, therefore it's suggested to implement a larger plane with increased mass and wing area.

Figure 4.19 presents the drag power estimate for one loop of the circle (left) and

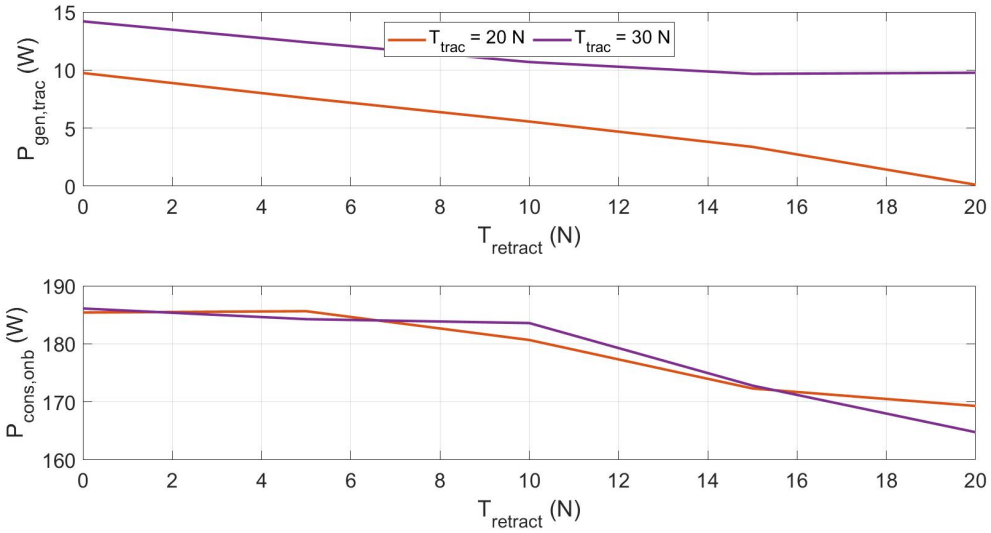

Figure 4.18: Variation of traction power generation and onboard power consumption with retraction tension set-point

figure-8 (right) trajectories, implementing an ideal winch control that can maintain constant tension of 15 N while flying in 7 m/s wind speeds. The onboard consumed power (red curve) is directly proportional to the forward motor output, which is constantly on to follow the trajectory. Small periods with zero throttle allows the propeller to act as a turbine driving the motor as a generator. The theoretical generated power (green curve) is a fraction of the power consumed as a consequence of the amount of energy that any rotor can harness from the wind based on Betz limit. The figure-8 trajectory presents an improvement in the consistency of drag power during the diving sections of the path, as the plane's throttle spends more time shut-off, potentially enabling longer periods of power generation. A suggestion for further development is a model that considers the use of the quadcopter components as onboard turbines. This would require an actuator system that could turn the orientation of the VTOL motors from vertical to horizontal.

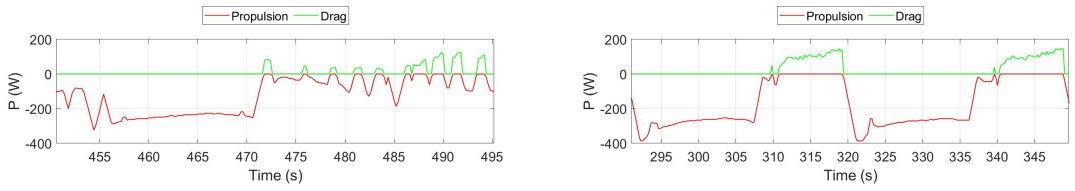

Figure 4.19: Power consumed by onboard propulsion (red) and theoretical power generated by drag mode (green) for circular trajectory (left) and figure-8 (right)

The pumping mode power for one cycle using an ideal winch of 15 N tension set-point and 7 m/s environment wind speeds is presented in Figure 4.20. The results show similarities to the drag mode cycle in terms of throttle required to perform one loop. The generation is now done through the tension and speed at the ground station (green curve), resulting in similar net cycle traction power for the circle (left) and figure-8 (right), still significantly below the required onboard power consumption (red curve) required to follow the trajectory. These results highlight the importance of integrating the plane navigation with a winch control for maximizing the traction power generation, whereas the GS must provide the right tension depending on the plane flight phase.

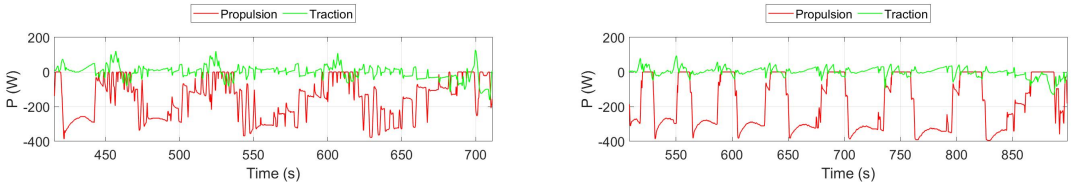

Figure 4.20: Power consumed by onboard propulsion (red) and theoretical power generated by pumping mode (green) for circular trajectory (left) and figure-8 (right)

4.8 Conclusions

This chapter presented the process of using the `Ardupilot` SIL simulation to estimate and tune the performance of the developed hardware. The simulation is used to tackle the challenge of achieving a fully autonomous lab-scale prototype. The general architecture of the `Ardupilot` is described in a comparative approach between the software and the hardware implementation. The simulated and real data can be used to influence each other through evaluation of logged data, and thus, adapt the flight controller parameters. A key aspects of the autopilot is the different control strategies: fixed-wing navigation, speed and height, attitude, and quadcopter position and attitude controllers. Tuning the corresponding parameters allows to better represent the real quadplane performance.

AWES flight plans are defined as waypoint missions, from vertical take-off, transition into crosswind flight, and vertical landing. VTOL is enabled with the incorporation of the quadplane parameters, defined from the hardware specifications. A tether is modeled as an elastic rod in the physics model of the SIL simulation. In-

corporating its drag, weight, and tension as an external force applied to the plane's body axes. Combining VTOL with the tether model, fully autonomous missions are simulated. Fixed tether length simulations allow the plane to enter crosswind flight, but generating high tension peaks due to frequent switching between slack and taut tether, causing a significant deviation from the specified trajectory. This led to the implementation of an ideal winch control that maintains a constant tension. The flight parameters of successful trajectory tracking simulations are saved for further implementation in the real flight controller. During the pumping mode simulations, challenges were encountered in maintaining a steady positive reel-out speed in the traction phase, concluding that the trajectory and pitch controller must be fine-tuned jointly with the objective of achieving positive traction power generation.

Results from the simulation demonstrated that the system can produce relatively small traction power, and theoretical drag power. For this scale, the system still requires energy input to operate. It becomes a hardware limitation in regards of the battery capacity, and thus the available flight time. A system scaling study is suggested to attempt to obtain a net positive power output from the simulation, potentially using the results for developing a scaled-up prototype. This study would assesses the power generation and trajectory tracking with planes with a larger wing area and mass. Therefore, it would require the aerodynamic characterization and re-iteration of the hardware design process.

Chapter 5

Experimental Flight Testing of an Airborne Wind Energy Prototype

5.1 Introduction

Airborne Wind Energy Systems (AWES) complexity in terms of automation in flight control requires that prototypes undergo countless number of experimental tests. Usually, AWES flight tests are classified as high risk operations, whereas a minor failure is very probable to occur and could lead to a total loss of the device due to crashing. On the larger scale, companies like Ampyx Power have adopted the aerospace certification, mitigating the risk of crashing by using thorough methods for failure modes characterization for every component of the aircraft. On the smaller scale, companies and research groups cannot afford such complex and expensive methods, therefore a solution is to reduce the cost related to a potential failure. This is done by developing small-scale devices from off-the-shelf components, still providing valuable operational insight and model validation, but in case of a crash the device could be easily replaced with relatively low investment.

This chapter focus on the flight tests performed by the lab-scale prototype developed with the `Ardupilot` code. Comparing the experimental results to the SIL simulations allows to find the main discrepancies between the actual hardware performance and the model, and further tune the simulation to more accurately resemble the quadplane. Furthermore, preparing and executing the flight tests provides a valuable insight of the legal requirements and regulation that must be assessed before flight.

5.2 Flight regulations in Canada

Aerospace regulations are certainly a limiting factor for AWES systems [46], and small-scale systems are not exempt from the strict regulations. This presents a major challenge in regards to performing experimental flight tests. However, the organization of the appropriate licensing, aircraft registration, permits, and operation documents provided an operational window that allowed the quadplane to be tested.

In terms of operation procedures a detailed Concept of Operations (CONOPS) document was formulated and presented in Appendix B, containing a detailed site survey, emergency procedures, flight operations procedures, aircraft flight and maintenance logs. This process was possible with the assistance of the Center for Aerospace Reseach (CFAR) which provided the appropriate orientation for building the procedures towards a safe and legal operation.

The concept of operation first defines the purpose and objective of the flight operation, which is validating the simulation models with the experimental results, as well as proving the concept of development of a low-investment AWES platform. The site survey describes the flight operation area, detailing the potential hazards, recovery routes, and pre-flight site inspection procedure. Moreover, the roles and responsibilities of the crew are clearly stated. Pre-operation checks and briefings are detailed, along with the estimated vehicle performance specifications. The emergency procedures describe a series of possible emergency scenarios and provide a list of executable actions to countermeasure the potential situation. Furthermore, the document contains a list of the pre-flight check to be performed to the aircraft before each flight. The test flight cards which states the flight test objective, and step-by-step flight actions. Finally, the post-flight checks are presented, including inspections, flight data transfer and analysis.

The flight logs keep track of the flights performed, while the maintenance logs keep track of the modifications made to the aircraft. These documents are required to be on-site during the operation for reference and for complying with the legal requirements.

5.3 Flight Test Campaign

A series of experimental flight tests are performed with increased complexity. Each flight test targets specific objectives for verifying the autopilot performance. Mak-

ing sure that the previous requirements are operating accordingly before each test increases the rate of success and safety of the mission. The flight tests consists in: VTOL controller tuning, non-tethered VTOL, tethered VTOL, non-tethered waypoint tracking in quadcopter modes, manual airspeed sensor calibration wind box, non-tethered waypoint tracking in fixed-wing mode, and tethered waypoint tracking in fixed-wing mode. Each flight has its specific objective with the goal of gradually tune the system to full autonomous crosswind flight. Some specific objectives might involve: attitude control, position hold, throttle evaluation, sensor calibration, effects of tether tension, and waypoint navigation performance.

5.3.1 Vertical take-off and landing controller tuning

Getting Vertical take-off and landing (VTOL) working properly is the most critical part of the operation of the prototype; this allows the plane to go from a parked position to crosswind flight without requiring manual input from a pilot or a large take-off area. A well-tuned operation also allows recovering flight control in case of an unexpected event such as tether rupture or irregular winch operation. The VTOL tuning process consists of finding the best PID gains for the attitude controller described in Chapter 4. Fortunately, the `Ardupilot` platform has the QATOTUNE flight mode that gives step commands to the hovering plane in the pitch, roll, and yaw direction to evaluate its response and estimate the gains.

To enter the QAUTOTUNE flight mode, the plane needs to take-off manually in a semi-autonomous mode such as QHOVER or QSTABILIZE, and then change the mode switch to QAUTOTUNE. Once stable, the plane will commence the tuning process one axis at a time. When finished, the plane should be manually landed and disarmed without switching out of the QAUTOTUNE mode. Figure 5.1.a show the commanded roll angle step and the actual response of the plane during the tuning process, and Figure 5.1.b shows the desired and actual roll rates. This process is repeated for the remaining pitch and yaw axis.

The quadcopter attitude controller applies PID gains to the pitch, roll, and yaw rate errors to find the optimal motor output. Table 5.1 presents the angular rate gains obtained from the test. A more complete list of parameters can be found in the Appendix A. The proportional gain multiplies the rate error, and should be increased as much as possible without causing oscillations. The integral gain attempts to remove the accumulated error over time. It should increase if the desired rate is not being

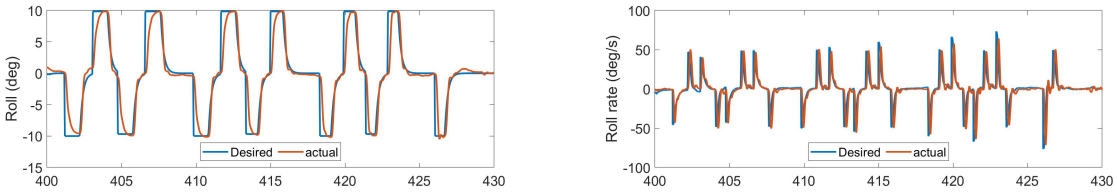

(a) Roll angle (b) Roll rate

Figure 5.1: QAUTOTUNE (a) roll angle and (b) roll rate

met over time. Lastly, the derivative gain dampens the response by considering the error change rate. A derivative gain too high can amplify the noise, while too low overshoots the response.

Table 5.1: QAUTOTUNE rate controller PID gains

PARAMETER	P	I	D
Q_A_RAT_ROLL_	0.33628	0.33628	0.01440
Q_A_RAT_PITCH_	4.5	0.25	0.0036
Q_A_RAT_YAW_	0.18	0.018	0

5.3.2 Autonomous take-off and landing

The first flight test consist in performing a vertical take-off, hover for 60 seconds at an altitude of 3 meters, and finally land. The objective of this test is to evaluate the flight controller performance in terms of (1) meeting and maintaining the altitude target, (2) maintaining the intended hover location, (3) evaluating the required hover throttle, and (4) evaluating the plane attitude during the test.

The flight test results are presented in Figure 5.2 in an orange line, while the simulation results are presented in a blue line. The simulation and experimental times where adjusted to match at the take-off.

The 3D trajectory plot shows the inconsistency of the location in the X axis, which is justified with the accuracy of the GPS measurements. However, once the flight begins, the take-off location is locked and the quadplane will attempt to maintain a consistent location hold in the X and Y coordinates. Remarkably, the actual flight controller achieved a controlled vertical climb while the simulation diverged almost 8 meters before reaching the hover altitude. The GPS measurement error produces a non-zero ground speed, which leads to the active position hold though attitude

variations. In overall, the quadplane was able to successfully hold the desired position and altitude autonomously, allowing to advance into the tethered autonomous VTOL flight.

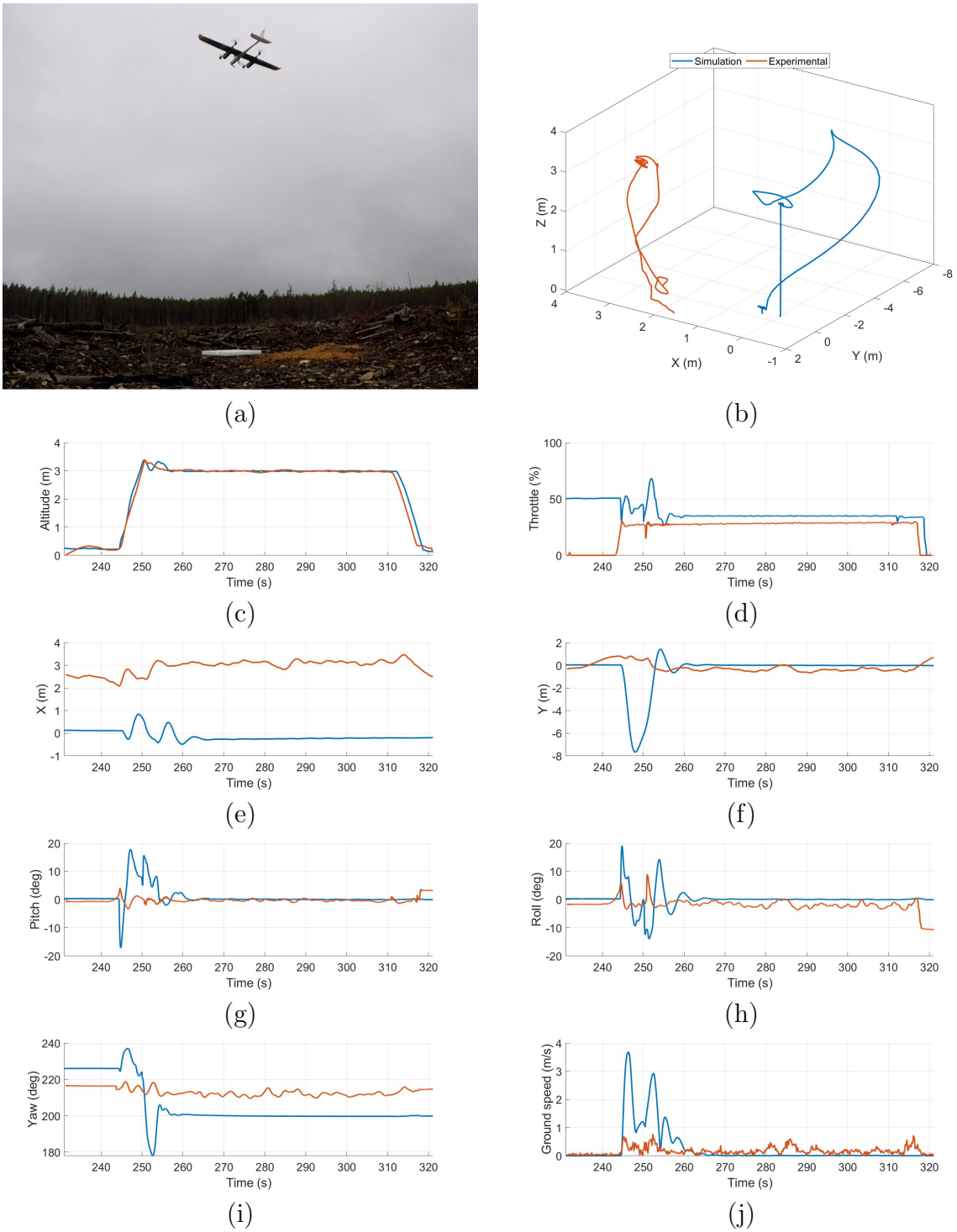

Figure 5.2: Simulation and experimental results for autonomous VTOL and hover: (a) experimental test snapshot, (b) trajectories, (c) altitudes, (d) throttle, (e) X position, (f) Y position, (g) pitch, (h) roll, (i) yaw, and ground speeds.

5.3.3 Autonomous tethered take-off and landing

The following test flight consisted in performing VTOL and hover with the incorporation of the ground station and tether. The plane is commanded to take-off and hover at 3 meters for 10 seconds, where the tether would be manually reeled in until taut. Then the plane is commanded to vertically climb to 10 meters, where it would stay hovering for 2 minutes. Then manual yanks are applied to assess the quadplane stability, and record the tension loads on the ground station as well as the Inertia Measurement Unit (IMU) accelerations.

The ground station was placed 10 meters from the take-off location as shown in Figure 5.3.b. The position results show how the quadplane is able to hold the target waypoint in quadcopter mode even when the tether is being pulled. The ground station tension peaks on Figure 5.3.f were recorded with the tension sensor, and then compared with the body forces resultant from the IMU acceleration measurements. As the tension increases the quadplane is forced towards the ground station, however, the quadcopter motors counteract this tension with additional thrust as in Figure 5.3.d. For the sake of completeness, the tether weight and drag were estimated from the quadplane position and airspeed, resulting in values that can be neglected for the purpose of this flight tests.

In conclusion, the quadplane sucessfully performed the tethered VTOL autonomous flight mission. The manual yanks on the line could be counteracted by the quadcopter motor to continue to hold position and altitude. Finally, the matching forces from the ground station tension measurement and IMU acceleration logs provide an approach for evaluating the interaction between them.

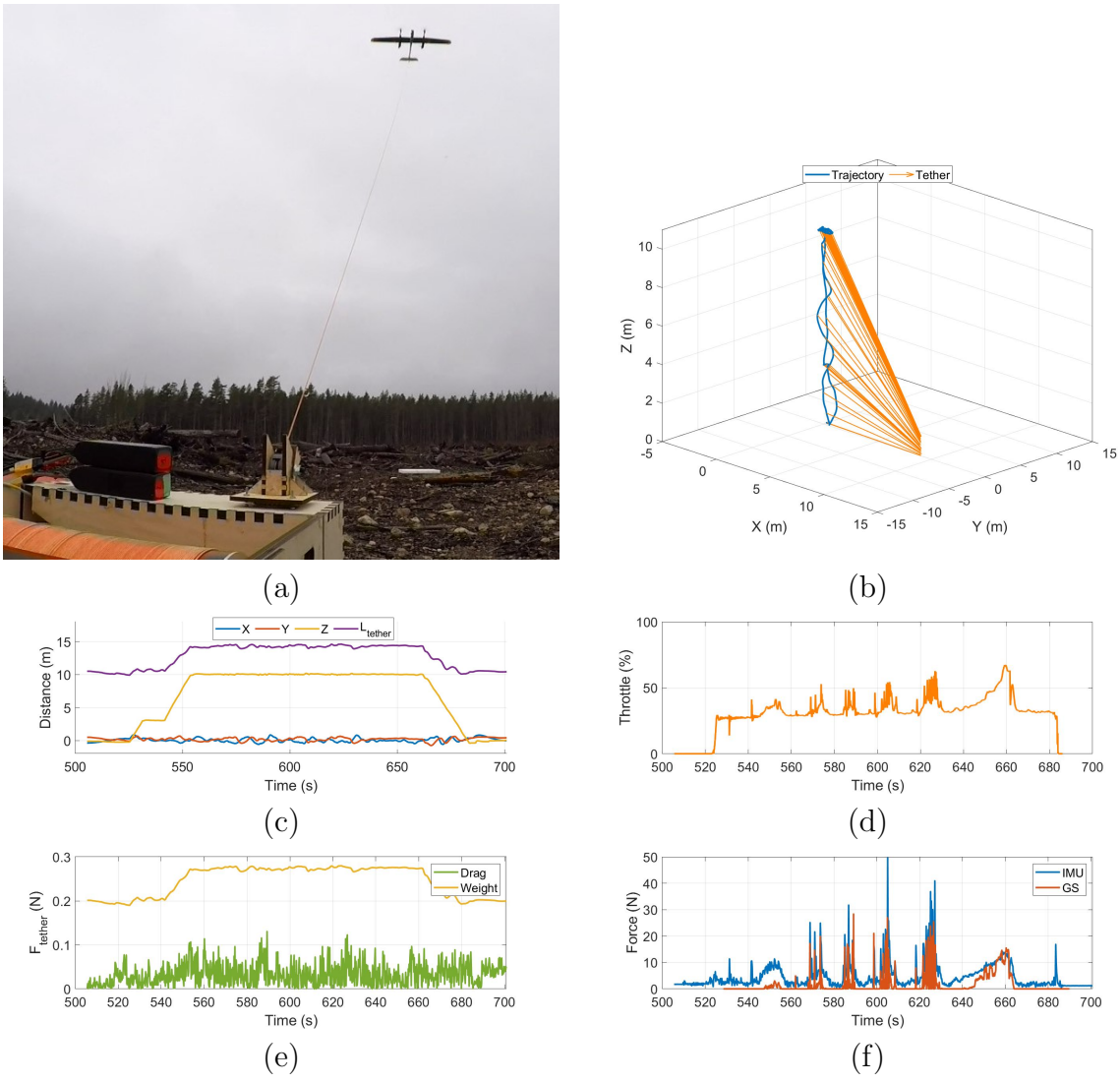

Figure 5.3: Experimental results for autonomous tethered VTOL. (a) Experimental test snapshot, (b) resultant trajectory and tether, (c) distances, (d) quadcopter throttle, (e) tether drag and weight, and (f) ground station and quadplane forces

5.3.4 Autonomous waypoint mission

This test verifies that the real flight controller can navigate the un-tethered quadplane through a series of points. It is performed using the quadcopter motors for vertical lift, while the front motor provides the forward thrust. To avoid transition into forward flight, the maximum forward throttle is limited to 15%, as the airspeed sensor is still not calibrated for fixed-wing modes. The flight test consists in taking-off vertically to an altitude of 10 meters, navigate to the 4 waypoints (3, 4, 5, and 6) in Figure 5.4.a, return to "home", and land. The entire mission is performed autonomously maintaining a constant altitude of 10 meters.

Regardless of the defined controller parameters, such as speeds and throttle limits, the simulated quadplane continued to overshoot the waypoints with flight speeds larger than expected. Therefore, the aerodynamic characteristics of the plane were adjusted by increasing the value of C_{D0} from 0.1 to 1.3. This additional drag represents the quadcopter hardware and the foam blocks used for early testing protection. Once the controller is reliable in forward flight, the blocks could be removed allowing to obtain the appropriate drag coefficient that best resembles the hardware.

Figure 5.4.b show a similar trajectory for the simulation and flight test. The battery voltage became dangerously low approaching the final waypoint, causing the pilot to take manual control of the plane and perform an emergency landing. This specific mission demands high energy consumption, as it requires continuous operation of the VTOL combined with the forward motor. The battery capacity is a major constraint and should be further improved for longer lasting flight tests.

The airspeed sensor is used for a better estimation of the plane speed. However, Figure 5.4.h shows that it still requires calibration before being used for an autonomous transition. The noise in the measurement has a mean deviation of 2 m/s, potentially failing to recognize the critical speed values such as trim speed, stall speed, and most importantly, the quadcopter assist speed. A manual flight test is suggested for sensor calibration performing a wind box using the GPS ground speed as reference.

Distance plots in Figure 5.4 show that the simulated mission is finished in less time. This is caused by the drop in ground speed during the segment 4 to 5, possibly a consequence of unmeasured wind gusts coming from the East direction (towards negative Y in Figure 5.4.b). This leads to conclude that an appropriate airspeed sensor calibration is indispensable for advancing the testing to fixed-wing flight modes.

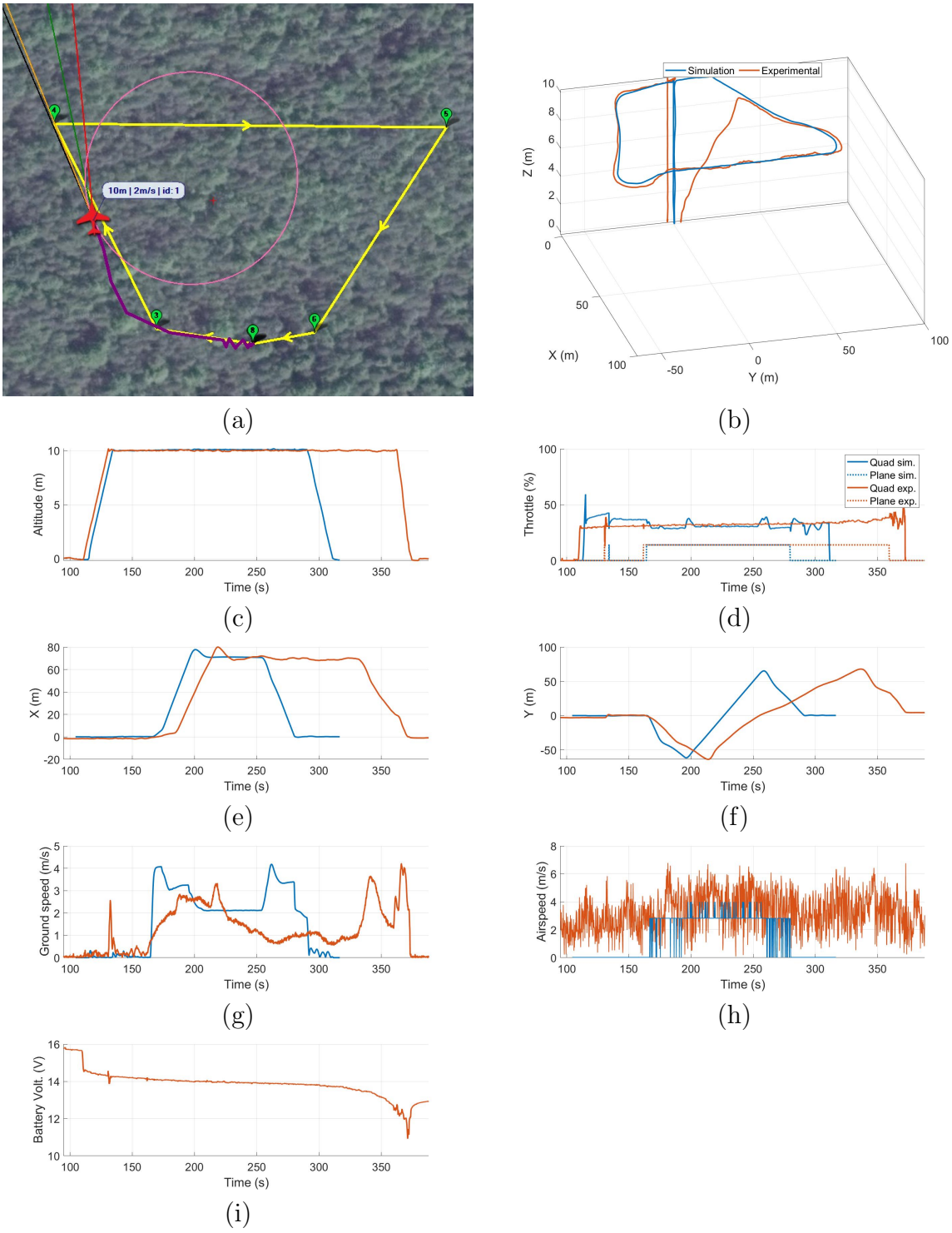

Figure 5.4: Simulation and experimental results for autonomous VTOL and waypoint tracking. (a) Flight mission waypoints snapshot, (b) resultant trajectories, (c) altitudes, (d) throttle, (e) X position, (f) Y position, (g) ground speed, (h) airspeed, and (i) battery voltage.

5.3.5 Future flight tests

Flight testing takes an unforeseen amount of time. Once the hardware is ready, other components have to be organized in order to properly, safely, and legally perform the flight tests. First, the right documentation previously described must be completed. Second, the appropriate flight testing location that complies with the regulations has to be defined, surveyed, and approved by the crew. Lastly, the flight test crew need to be organized. This involves finding an experienced pilot that could perform the manual tests and be on standby for taking over control on an autonomous mission.

The testing phase is still ongoing. The future scheduled tests are described in the Concept of Operations document in Appendix B. Ultimately, the goal is to achieve crosswind flight with fixed tether length and pumping mode. The tests flight to reach that stage are presented as follows:

- Manual airspeed sensor calibration (reference CONOPS).
- Autonomous non-tethered VTOL and waypoint tracking in fixed-wing mode at constant altitude (reference CONOPS).
- Autonomous non-tethered VTOL and waypoint tracking in fixed-wing mode at variable altitude (reference CONOPS).
- Autonomous tethered VTOL and circular waypoint trajectory tracking in fixed-wing mode. Performed at constant altitude and fixed tether length (to be defined).
- Circular crosswind flight in fixed tether length. Autonomous tethered VTOL and circular waypoint trajectory tracking in fixed-wing mode. Performed at variable altitude and fixed tether length (to be defined)
- Figure-8 crosswind flight in fixed tether length. Autonomous tethered VTOL and figure-8 waypoint trajectory tracking in fixed-wing mode. Performed at variable altitude and fixed tether length (to be defined)
- Circular crosswind flight in pumping mode. Autonomous tethered VTOL and circular waypoint trajectory tracking in fixed-wing mode. Performed at variable altitude and variable tether length (to be defined)

- Figure-8 crosswind flight in pumping mode. Autonomous tethered VTOL and figure-8 waypoint trajectory tracking in fixed-wing mode. Performed at variable altitude and variable tether length (to be defined)

5.4 Conclusions

Flight tests are currently ongoing. So far the prototype has been able to perform VTOL controller calibration, autonomous tethered and non-tethered flight, and VTOL mode waypoint trajectory tracking. The controller calibration provided the appropriate PID gains that allowed the next tests to be performed successfully. The quadplane is able to autonomously hold position and altitude, vertically climb with applied tether tension, and manage to keep stable while performing manual tension peaks. The defined waypoint mission was followed successfully. However, the real flight took longer time to complete than the simulation. This could be due to an uncalibrated airspeed sensor, additional drag from the temporally protective equipment, and unaccounted wind speeds during the operation. The tests confirmed the battery capacity and flight time limitation, and its suggested for further studies to increase the autonomy of the quadplane.

Chapter 6

Conclusions

6.1 Overview of software and hardware integration for flight testing

This thesis developed a lab-scale AWES prototype using the `Ardupilot` open-source autopilot platform. The goal is to provide initial insight into the overall system, gather preliminary flight data, and get real-world experience in AWES operation. The quadplane developed consists of a hybrid between a fixed-wing plane and quadcopter. This airframe configuration was selected for ease of operation through its VTOL approach and potential to automate the entire flight mission. The hardware was characterized through static studies of the quadplane. Parameters such as trim speed and throttle, stall and maximum speed, hover thrust, and maximum vertical speeds are identified and input to the SIL simulation. The quadplane was simulated in the `Ardupilot` SIL simulation using the hardware parameters. To account for AWES operation, an elastic tether model was incorporated into the plane physics model as external drag, weight, and tension forces applied to the CG. The simulation flight controllers were tuned using autonomous flight missions that involve VTOL and crosswind flight, obtaining the most appropriate controller parameters that can further be integrated to the hardware controller. Preliminary flight tests were performed to continue tuning the controllers and provide feedback to the simulation. In overview, iterating between the hardware operation and SIL simulations allows convergence of the system parameters and provides a better estimation of its performance.

6.2 Conclusions

A 2-meter wingspan commercial model RC plane was structurally reinforced for tethered flight by replacing the original aluminum wing spars with carbon fiber tubes. VTOL was enabled through the integration of a quadcopter frame to the fixed-wing structure. Autopilot operation was enabled with the incorporation of the `Ardupilot` compatible hardware (Pixhawk flight controller), GPS module, airspeed sensor, and radio and telemetry systems. The motor sizing and quadcopter frame had to be iterated to allow sufficient lifting capabilities. A ground station was developed in collaboration with 4th year Mechanical Engineering students as part of their program requirements. The ground station is self-contained and designed for portability. It manages the tether into a spool through a linear actuator mechanism, and allows tether tension measurements.

A 3 DOF flight model was developed in spherical coordinates for controller tuning, load estimation, and trajectory tracking. It was used to verify that a simple navigation controller, similar to the `Ardupilot` controller, can achieve AWES trajectory tracking. Overall, the model provides a tool for evaluating different system dimensions, wind profiles, and trajectories.

The developed hardware was tuned using the `Ardupilot` SIL tool. The key controller parameters were obtained from running simulations that would later become flight tests. The simulations allowed evaluating the performance of the tether model, the VTOL components, trajectory tracking controllers, and assess the system's power generation. The tether model is a physical constraint that prevents the plane flying any further than the tether length. The VTOL components simplify the take-off and landing phases and allows automation of the entire mission. The navigation controllers successfully manage to follow the specified trajectory when implementing an ideal winch model. The power analysis shows that there is potential for power generation, and suggest studying larger-scale systems where the power output could be increased with the wing area.

An incremental flight test campaign was defined to gradually get testing experience and collect flight data. Initial test flights were performed to physically tune the VTOL controller through an `Ardupilot` autonomous flight mode. The new PID gains are then used in autonomous VTOL flights tests such as, position and altitude hold, tether load assessment, and waypoint navigation. More flight tests are being scheduled with the goal of achieving a fully autonomous AWES crosswind flight.

6.3 Lessons Learned

Aerospace design and development is an iterative process. The aircraft subsystems including, aerodynamics, propulsion, controls, and structure design, have their individual challenges, while they are also dependent of each other. Selecting an off-the-shelf model plane constrained the design specifications, such as wing area, fuselage space, and structural strength. The selection of the quadcopter propulsion system is a component that should be prioritized in this type of prototype. In general, the thrust to weight ratio should be greater than 2 to allow hovering at 50% thrust. However, being AWES highly maneuverable and required to carry a tether, it is suggested to target higher thrust to weight ratios. Additionally, the plane wing area should be selected or designed to account for the extra weight from the VTOL components. Furthermore, the relation between wing area, total weight, vertical thrust should be optimized for increasing the autonomy of the aircraft through the battery selection.

Robustly controlling AWES is not trivial. This might be one of the reasons why the industry hasn't reached commercialization yet. The incorporation of the tether increases the complexity level of any flight control system. The control challenge is recognized through the development of a simple controller for a 3DOF model. Even though this is a highly idealized model, the flight controller is not entirely robust. Advancing into realistic 6DOF flight models, would then require advanced flight controllers that increase the system's operation reliability, and require to coordinate the plane operation with the ground station tether control.

The `Ardupilot` code is a extensive repository containing many libraries, main files, headers, functions, etc. Tackling the code for the first time could be overwhelming. Therefore, it is suggested to take additional time in understanding the system's architecture, and how subsystems work and are linked to each other. The `Ardupilot` website is well-supported and contains all this information, also, the community blogs are an excellent tool to use for getting additional help code development. Moreover, the `Ardupilot` platform is in C++ programming language, which has a steep learning curve. Modifying the code presented a challenge no only because of its complexity and numerous functions, but because there is no way of troubleshoot the edits performed in the SIL library files.

Flight tests took an unforeseen amount of preparation. The experimental quadplane falls into drone regulations, and require a number of legal documents, permits, and certifications to legally operate for research purposes. A suggestion to improve

this process, is to invest time in preparing the documents from the beginning of the project, as some might take longer than expected and could delay the entire project. The first flights must be performed manually before implementing the autopilot, therefore another challenge is finding an experienced and certified pilot. Overall, flight testing should involve a group of people that take different roles, and expanding the project to collaborate with local aerospace student and research groups is recommended.

6.4 Future work

Immediate future work consists in completing the integration of the electric and power components to the mechanical part of the ground station, enabling its full autonomous operation. The testing campaign is ongoing with the goal of achieving autonomous crosswind flight. Future flight tests will perform the simulated missions to further tune the flight controller parameters. Furthermore, it is suggested to reevaluate the onboard battery system, as the flight time is the main limitation for the flight tests.

The continuation of the AWES-`Ardupilot` project could be done by assessing larger-scale devices for energy generation. A scaled-up version of the quadplane could be implemented in the simulation to assess the net power output. Following the building process, a larger device with better aerodynamic performance could be developed taking into consideration the challenges and limitations encountered presented in this thesis.

Bibliography

[1] "The paris agreement," https://unfccc.int/process-and-meetings/the-paris-agreement/the-paris-agreement, accessed: 2019-11-24.

[2] T. A. Boden, G. Marland, and R. J. Andres, "Global, regional, and national fossil-fuel co2 emissions," *Carbon Dioxide Information Analysis Center, Oak Ridge National Laboratory, US Department of Energy, Oak Ridge, Tenn., USA doi*, vol. 10, 2009.

[3] M. L. Loyd, "Crosswind kite power (for large-scale wind power production)," *Journal of energy*, vol. 4, no. 3, pp. 106–111, 1980.

[4] "Skydio," https://www.skydio.com/, accessed: 2019-07-1.

[5] U. Zillmann and P. Bechtle, "Emergence and economic dimension of airborne wind energy," in *Airborne Wind Energy*. Springer, 2018, pp. 1–25.

[6] C. Archer and K. Caldeira, "Global assessment of high-altitude wind power," *Energies*, vol. 2, no. 2, pp. 307–319, 2009.

[7] "Enercon E-126 wind turbine," https://www.enercon.de/en/products/ep-8/e-126/, accessed: 2019-06-30.

[8] D. Vander Lind, "Analysis and flight test validation of high performance airbornewind turbines," in *Airborne Wind Energy*. Springer, 2013, pp. 473–490.

[9] "Makani airborne wind energy," https://makanipower.com/, accessed: 2019-06-30.

[10] U. Ahrens, M. Diehl, and R. Schmehl, *Airborne wind energy*. Springer Science & Business Media, 2013.

[11] M. I. Hoffert, K. Caldeira, A. K. Jain, E. F. Haites, L. D. Harvey, S. D. Potter, M. E. Schlesinger, S. H. Schneider, R. G. Watts, T. M. Wigley *et al.*, "Energy implications of future stabilization of atmospheric co 2 content," *Nature*, vol. 395, no. 6705, p. 881, 1998.

[12] M. Sommerfeld, C. Crawford, G. Steinfeld, and M. Dörenkämper, "Improving mid-altitude mesoscale wind speed forecasts using lidar-based observation nudging for airborne wind energy systems."

[13] A. Cherubini, A. Papini, R. Vertechy, and M. Fontana, "Airborne wind energy systems: A review of the technologies," *Renewable and Sustainable Energy Reviews*, vol. 51, pp. 1461–1476, 2015.

[14] L. Fagiano and S. Schnez, "On the take-off of airborne wind energy systems based on rigid wings," *Renewable energy*, vol. 107, pp. 473–488, 2017.

[15] M. Erhard and H. Strauch, "Flight control of tethered kites in autonomous pumping cycles for airborne wind energy," *Control Engineering Practice*, vol. 40, pp. 13–26, 2015.

[16] R. Luchsinger, D. Aregger, F. Bezard, D. Costa, C. Galliot, F. Gohl, J. Heilmann, H. Hesse, C. Houle, T. A. Wood *et al.*, "Pumping cycle kite power with twings," in *Airborne Wind Energy*. Springer, 2018, pp. 603–621.

[17] A. Bormann, M. Ranneberg, P. Kövesdi, C. Gebhardt, and S. Skutnik, "Development of a three-line ground-actuated airborne wind energy converter," in *Airborne wind energy*. Springer, 2013, pp. 427–436.

[18] L. Fagiano, A. U. Zgraggen, M. Morari, and M. Khammash, "Automatic crosswind flight of tethered wings for airborne wind energy: Modeling, control design, and experimental results," *IEEE Transactions on Control Systems Technology*, vol. 22, no. 4, pp. 1433–1447, 2013.

[19] "Could high-flying drones power your home one day?" https://www.bbc.com/news/business-48132021?ocid=wsnews.chat-apps.in-app-msg.whatsapp.trial.link1_.auin, accessed: 2019-07-1.

[20] "Ampyx Power," https://www.ampyxpower.com/, accessed: 2019-07-1.

[21] "Kitemill," http://www.kitemill.com/, accessed: 2019-07-1.

[22] "Kite Power," https://kitepower.nl/, accessed: 2019-07-1.

[23] "Twingtec," http://twingtec.ch/, accessed: 2019-07-1.

[24] "Enerkite," https://www.enerkite.de/en/, accessed: 2019-07-1.

[25] K. Geebelen, H. Ahmad, M. Vukov, S. Gros, J. Swevers, and M. Diehl, "An experimental test set-up for launch/recovery of an airborne wind energy (awe) system," in *2012 American Control Conference (ACC)*. IEEE, 2012, pp. 4405–4410.

[26] L. Fagiano, E. Nguyen-Van, F. Rager, S. Schnez, and C. Ohler, "A small-scale prototype to study the takeoff of tethered rigid aircrafts for airborne wind energy," *IEEE/ASME Transactions on Mechatronics*, vol. 22, no. 4, pp. 1869–1880, 2017.

[27] P. Bechtle, T. Gehrmann, C. Sieg, and U. Zillmann, "Awesome: An open-source test platform for airborne wind energy systems," *arXiv preprint arXiv:1704.08695*, 2017.

[28] "Ardupilot," http://ardupilot.org/, accessed: 2019-07-4.

[29] J. Baker, "Airborne wind energy system," Undergraduate Honours Thesis, University of Victoria, 2019.

[30] "XFLR5," http://www.xflr5.tech/xflr5.htm, accessed: 2019-09-06.

[31] T. C. Corke, *Design of aircraft*. Prentice Hall Englewood Cliffs, NJ, 2003.

[32] L. Fagiano, E. Nguyen-Van, F. Rager, S. Schnez, and C. Ohler, "Autonomous takeoff and flight of a tethered aircraft for airborne wind energy," *IEEE Transactions on Control Systems Technology*, vol. 26, no. 1, pp. 151–166, 2017.

[33] M. Clinckemaillie, K. Geebelen, M. Diehl, and D. Vandepitte, "An experimental set-up for energy generation using balanced kites," Masters thesis, KU Leuven, 2012.

[34] A. Luo, A. Polglase, Z. Scaife, K. Sprague, and T. Stochmal, "Airborne wind energy system final report," MECH 400 Report, University of Victoria, 2019.

[35] S. Samuel, "Airborne wind energy ground station," Undergraduate Honours Thesis, University of Victoria, 2019.

[36] M. Canale, L. Fagiano, and M. Milanese, "High altitude wind energy generation using controlled power kites," *IEEE Transactions on Control Systems Technology*, vol. 18, no. 2, pp. 279–293, 2009.

[37] G. B. da Silva, "Airborne wind energy systems: Modelling, simulation and trajectory control," 2018.

[38] S. Park, J. Deyst, and J. How, "A new nonlinear guidance logic for trajectory tracking," in *AIAA guidance, navigation, and control conference and exhibit*, 2004, p. 4900.

[39] R. H. Luchsinger, "Pumping cycle kite power," in *Airborne wind energy*. Springer, 2013, pp. 47–64.

[40] M. Sommerfeld, C. Crawford, G. Steinfeld, and M. Dörenkämper, "Improving mid-altitude mesoscale wind speed forecasts using lidar-based observation nudging for airborne wind energy systems," *Wind Energy Sci Discuss*, pp. 1–30, 2019.

[41] "`AWEbox`: Modelling and optimal control of multiple-kite systems for airborne wind energy," https://github.com/awebox/awebox, accessed: 2019-11-12.

[42] "Px4," https://px4.io/, accessed: 2019-11-24.

[43] T. Gehrmann, "A development of an open-source wind drone," Master thesis, University of Bonn, 2016.

[44] "Ardupilot pid tuning guide," http://ardupilot.org/plane/docs/roll-pitch-controller-tuning.html, accessed: 2019-11-12.

[45] B. Houska and M. Diehl, "Optimal control for power generating kites," in *2007 European Control Conference (ECC)*. IEEE, 2007, pp. 3560–3567.

[46] V. Salma, R. Ruiterkamp, M. Kruijff, M. R. van Paassen, and R. Schmehl, "Current and expected airspace regulations for airborne wind energy systems," in *Airborne Wind Energy*. Springer, 2018, pp. 703–725.

Appendix A

`Ardupilot` parameter list

ACRO_LOCKING	0	BATT_AMP_OFFSET	0	BRD_OPTIONS	1
ACRO_PITCH_RATE	180	BATT_AMP_PERVLT	36.364	BRD_PWM_COUNT	8
ACRO_ROLL_RATE	180	BATT_ARM_MAH	0	BRD_RTC_TYPES	1
ADSB_ENABLE	0	BATT_ARM_VOLT	0	BRD_RTC_TZ_MIN	0
AFS_ENABLE	0	BATT_CAPACITY	5000	BRD_SAFETY_MASK	0
AHRS_COMP_BETA	0.1	BATT_CRT_MAH	0	BRD_SAFETYENABLE	1
AHRS_CUSTOM_PIT	0	BATT_CRT_VOLT	0	BRD_SAFETYOPTION	3
AHRS_CUSTOM_ROLL	0	BATT_CURR_PIN	1	BRD_SBUS_OUT	0
AHRS_CUSTOM_YAW	0	BATT_FS_CRT_ACT	0	BRD_SD_SLOWDOWN	0
AHRS_EKF_TYPE	2	BATT_FS_LOW_ACT	0	BRD_SER1_RTSCTS	0
AHRS_GPS_GAIN	1	BATT_FS_VOLTSRC	0	BRD_SER2_RTSCTS	0
AHRS_GPS_MINSATS	6	BATT_LOW_MAH	0	BRD_SERIAL_NUM	0
AHRS_GPS_USE	1	BATT_LOW_TIMER	10	BRD_TYPE	24
AHRS_ORIENTATION	0	BATT_LOW_VOLT	0	BRD_VBUS_MIN	4.3
AHRS_RP_P	0.2	BATT_MONITOR	3	BRD_VSERVO_MIN	0
AHRS_TRIM_X	-0.02200774	BATT_SERIAL_NUM	-1	BTN_ENABLE	0
AHRS_TRIM_Y	0.05320392	BATT_VOLT_MULT	18.182	CAM_AUTO_ONLY	0
AHRS_TRIM_Z	0	BATT_VOLT_PIN	0	CAM_DURATION	10
AHRS_WIND_MAX	0	BATT_WATT_MAX	0	CAM_FEEDBACK_PIN	-1
AHRS_YAW_P	0.2	BATT2_AMP_OFFSET	0	CAM_FEEDBACK_POL	1
ALT_CTRL_ALG	0	BATT2_AMP_PERVLT	36.364	CAM_MAX_ROLL	0
ALT_HOLD_FBWCM	0	BATT2_ARM_MAH	0	CAM_MIN_INTERVAL	0
ALT_HOLD_RTL	10000	BATT2_ARM_VOLT	0	CAM_RELAY_ON	1
ALT_OFFSET	0	BATT2_CAPACITY	3300	CAM_SERVO_OFF	1100
ARMING_ACCTHRESH	0.75	BATT2_CRT_MAH	0	CAM_SERVO_ON	1300
ARMING_CHECK	1	BATT2_CRT_VOLT	0	CAM_TRIGG_DIST	0
ARMING_MIS_ITEMS	0	BATT2_CURR_PIN	1	CAM_TRIGG_TYPE	0
ARMING_REQUIRE	1	BATT2_FS_CRT_ACT	0	CAM_TYPE	0
ARMING_RUDDER	2	BATT2_FS_LOW_ACT	0	CAN_D1_PROTOCOL	1
ARSPD_AUTOCAL	0	BATT2_FS_VOLTSRC	0	CAN_D2_PROTOCOL	1
ARSPD_BUS	1	BATT2_LOW_MAH	0	CAN_P1_DRIVER	0
ARSPD_FBW_MAX	25	BATT2_LOW_TIMER	10	CAN_P2_DRIVER	0
ARSPD_FBW_MIN	18	BATT2_LOW_VOLT	0	CAN_SLCAN_CPORT	0
ARSPD_OFFSET	66.18175	BATT2_MONITOR	3	CAN_SLCAN_SERNUM	-1
ARSPD_OPTIONS	0	BATT2_SERIAL_NUM	-1	CAN_SLCAN_TIMOUT	0
ARSPD_PIN	15	BATT2_VOLT_MULT	18.182	CHUTE_CHAN	0
ARSPD_PRIMARY	0	BATT2_VOLT_PIN	0	CHUTE_ENABLED	0
ARSPD_PSI_RANGE	1	BATT2_WATT_MAX	0	COMPASS_AUTO_ROT	2
ARSPD_RATIO	1.9936	BATT3_MONITOR	0	COMPASS_AUTODEC	1
ARSPD_SKIP_CAL	0	BATT4_MONITOR	0	COMPASS_CAL_FIT	16
ARSPD_TUBE_ORDER	2	BATT5_MONITOR	0	COMPASS_DEC	0.293615
ARSPD_TYPE	1	BATT6_MONITOR	0	COMPASS_DEV_ID	658953
ARSPD_USE	1	BATT7_MONITOR	0	COMPASS_DEV_ID2	658945
ARSPD2_TYPE	0	BATT8_MONITOR	0	COMPASS_DEV_ID3	0
AUTO_FBW_STEER	0	BATT9_MONITOR	0	COMPASS_DIA_X	1.004541
AUTOTUNE_LEVEL	6	BRD_BOOT_DELAY	0	COMPASS_DIA_Y	0.920237
AVD_ENABLE	0	BRD_IO_ENABLE	1	COMPASS_DIA_Z	1.069608

COMPASS_DIA2_X	0.9804512	COMPASS_PMOT_EN	0	EK2_MAGE_P_NSE	0.001
COMPASS_DIA2_Y	1.047837	COMPASS_PRIMARY	0	EK2_MAX_FLOW	2.5
COMPASS_DIA2_Z	0.9699239	COMPASS_TYPEMASK	0	EK2_NOAID_M_NSE	10
COMPASS_DIA3_X	1	COMPASS_USE	1	EK2_OGN_HGT_MASK	0
COMPASS_DIA3_Y	1	COMPASS_USE2	1	EK2_POS_I_GATE	500
COMPASS_DIA3_Z	1	COMPASS_USE3	0	EK2_POSNE_M_NSE	1
COMPASS_ENABLE	1	CRASH_ACC_THRESH	0	EK2_RNG_I_GATE	500
COMPASS_EXP_DID	-1	CRASH_DETECT	0	EK2_RNG_M_NSE	0.5
COMPASS_EXP_DID2	-1	DSPOILER_AILMTCH	100	EK2_RNG_USE_HGT	-1
COMPASS_EXP_DID3	-1	DSPOILER_CROW_W1	0	EK2_RNG_USE_SPD	2
COMPASS_EXTERN2	0	DSPOILER_CROW_W2	0	EK2_TAU_OUTPUT	25
COMPASS_EXTERN3	0	DSPOILER_OPTS	3	EK2_TERR_GRAD	0.1
COMPASS_EXTERNAL	1	DSPOILR_RUD_RATE	100	EK2_VEL_I_GATE	500
COMPASS_FLTR_RNG	0	EFI_TYPE	0	EK2_VELD_M_NSE	0.7
COMPASS_LEARN	0	EK2_ABIAS_P_NSE	0.005	EK2_VELNE_M_NSE	0.5
COMPASS_MOT_X	0	EK2_ACC_P_NSE	0.6	EK2_WIND_P_NSE	0.1
COMPASS_MOT_Y	0	EK2_ALT_M_NSE	3	EK2_WIND_PSCALE	0.5
COMPASS_MOT_Z	0	EK2_ALT_SOURCE	0	EK2_YAW_I_GATE	300
COMPASS_MOT2_X	0	EK2_BCN_DELAY	50	EK2_YAW_M_NSE	0.5
COMPASS_MOT2_Y	0	EK2_BCN_I_GTE	500	EK3_ENABLE	0
COMPASS_MOT2_Z	0	EK2_BCN_M_NSE	1	FBWA_TDRAG_CHAN	0
COMPASS_MOT3_X	0	EK2_CHECK_SCALE	150	FBWB_CLIMB_RATE	2
COMPASS_MOT3_Y	0	EK2_EAS_I_GATE	400	FBWB_ELEV_REV	0
COMPASS_MOT3_Z	0	EK2_EAS_M_NSE	1.4	FENCE_ACTION	0
COMPASS_MOTCT	0	EK2_ENABLE	1	FENCE_AUTOENABLE	0
COMPASS_ODI_X	0.1281756	EK2_EXTNAV_DELAY	10	FENCE_CHANNEL	0
COMPASS_ODI_Y	-0.005994271	EK2_FLOW_DELAY	10	FENCE_MAXALT	0
COMPASS_ODI_Z	0.05429669	EK2_FLOW_I_GATE	500	FENCE_MINALT	0
COMPASS_ODI2_X	0.000913646	EK2_FLOW_M_NSE	0.15	FENCE_RET_RALLY	0
COMPASS_ODI2_Y	-0.0237913	EK2_FLOW_USE	2	FENCE_RETALT	0
COMPASS_ODI2_Z	-0.01359636	EK2_GBIAS_P_NSE	0.0001	FENCE_TOTAL	0
COMPASS_ODI3_X	0	EK2_GLITCH_RAD	25	FLAP_1_PERCNT	0
COMPASS_ODI3_Y	0	EK2_GPS_CHECK	31	FLAP_1_SPEED	0
COMPASS_ODI3_Z	0	EK2_GPS_TYPE	0	FLAP_2_PERCNT	0
COMPASS_OFFS_MAX	1800	EK2_GSCL_P_NSE	0.0005	FLAP_2_SPEED	0
COMPASS_OFS_X	-26.19787	EK2_GYRO_P_NSE	0.03	FLAP_IN_CHANNEL	0
COMPASS_OFS_Y	20.77122	EK2_HGT_DELAY	60	FLAP_SLEWRATE	75
COMPASS_OFS_Z	55.96817	EK2_HGT_I_GATE	500	FLIGHT_OPTIONS	0
COMPASS_OFS2_X	-2.724532	EK2_HRT_FILT	2	FLOW_ADDR	0
COMPASS_OFS2_Y	-9.028031	EK2_IMU_MASK	3	FLOW_FXSCALER	0
COMPASS_OFS2_Z	-25.02127	EK2_LOG_MASK	1	FLOW_FYSCALER	0
COMPASS_OFS3_X	0	EK2_MAG_CAL	0	FLOW_ORIENT_YAW	0
COMPASS_OFS3_Y	0	EK2_MAG_EF_LIM	50	FLOW_POS_X	0
COMPASS_OFS3_Z	0	EK2_MAG_I_GATE	300	FLOW_POS_Y	0
COMPASS_ORIENT	0	EK2_MAG_M_NSE	0.05	FLOW_POS_Z	0
COMPASS_ORIENT2	0	EK2_MAG_MASK	0	FLOW_TYPE	0
COMPASS_ORIENT3	0	EK2_MAGB_P_NSE	0.0001	FLTMODE_CH	6

FLTMODE1	18	GPS_SBP_LOGMASK	-256	INS_GYRO_FILTER	20
FLTMODE2	18	GPS_TYPE	1	INS_GYROFFS_X	0.01856
FLTMODE3	19	GPS_TYPE2	0	INS_GYROFFS_Y	-0.01048
FLTMODE4	19	GRIP_ENABLE	0	INS_GYROFFS_Z	0.000707
FLTMODE5	10	GROUND_STEER_ALT	0	INS_HNTCH_ENABLE	0
FLTMODE6	10	GROUND_STEER_DPS	90	INS_LOG_BAT_CNT	1024
FORMAT_VERSION	13	HIL_ERR_LIMIT	5	INS_LOG_BAT_LGCT	32
FS_GCS_ENABL	0	HIL_MODE	0	INS_LOG_BAT_LGIN	20
FS_LONG_ACTN	0	HIL_SERVOS	0	INS_LOG_BAT_MASK	0
FS_LONG_TIMEOUT	5	HOME_RESET_ALT	0	INS_LOG_BAT_OPT	0
FS_SHORT_ACTN	0	ICE_ENABLE	0	INS_NOTCH_ENABLE	0
FS_SHORT_TIMEOUT	1.5	INITIAL_MODE	0	INS_POS1_X	0
GCS_PID_MASK	0	INS_ACC_BODYFIX	2	INS_POS1_Y	0
GLIDE_SLOPE_MIN	15	INS_ACC_ID	2621706	INS_POS1_Z	0
GLIDE_SLOPE_THR	5	INS_ACC2_ID	2688010	INS_POS2_X	0
GND_ABS_PRESS	100290.5	INS_ACC2OFFS_X	0.797409	INS_POS2_Y	0
GND_ABS_PRESS2	0	INS_ACC2OFFS_Y	0.020527	INS_POS2_Z	0
GND_ABS_PRESS3	0	INS_ACC2OFFS_Z	0.50325	INS_POS3_X	0
GND_ALT_OFFSET	0	INS_ACC2SCAL_X	0.991268	INS_POS3_Y	0
GND_EXT_BUS	-1	INS_ACC2SCAL_Y	0.984899	INS_POS3_Z	0
GND_FLTR_RNG	0	INS_ACC2SCAL_Z	0.972509	INS_STILL_THRESH	0.1
GND_PRIMARY	0	INS_ACC3_ID	0	INS_TRIM_OPTION	1
GND_PROBE_EXT	0	INS_ACC3OFFS_X	0	INS_USE	1
GND_TEMP	0	INS_ACC3OFFS_Y	0	INS_USE2	1
GPS_AUTO_CONFIG	1	INS_ACC3OFFS_Z	0	INS_USE3	1
GPS_AUTO_SWITCH	1	INS_ACC3SCAL_X	0	KFF_RDDRMIX	0.5
GPS_BLEND_MASK	5	INS_ACC3SCAL_Y	0	KFF_THR2PTCH	0
GPS_BLEND_TC	10	INS_ACC3SCAL_Z	0	LAND_ABORT_DEG	0
GPS_DELAY_MS	0	INS_ACCEL_FILTER	20	LAND_ABORT_THR	0
GPS_DELAY_MS2	0	INS_ACCOFFS_X	-0.21077	LAND_DISARMDELAY	20
GPS_GNSS_MODE	0	INS_ACCOFFS_Y	0.200316	LAND_DS_ABORTALT	0
GPS_GNSS_MODE2	0	INS_ACCOFFS_Z	-0.11856	LAND_DS_AIL_SCL	1
GPS_INJECT_TO	127	INS_ACCSCAL_X	0.997713	LAND_DS_APP_EXT	50
GPS_MIN_DGPS	100	INS_ACCSCAL_Y	0.997713	LAND_DS_ARSP_MAX	15
GPS_MIN_ELEV	-100	INS_ACCSCAL_Z	0.984499	LAND_DS_ARSP_MIN	10
GPS_NAVFILTER	8	INS_ENABLE_MASK	127	LAND_DS_D	0
GPS_POS1_X	0	INS_FAST_SAMPLE	1	LAND_DS_ELEV_PWM	1500
GPS_POS1_Y	0	INS_GYR_CAL	1	LAND_DS_I	0
GPS_POS1_Z	0	INS_GYR_ID	2621706	LAND_DS_IMAX	0
GPS_POS2_X	0	INS_GYR2_ID	2687754	LAND_DS_L1	30
GPS_POS2_Y	0	INS_GYR2OFFS_X	0.00092	LAND_DS_L1_I	0
GPS_POS2_Z	0	INS_GYR2OFFS_Y	-0.00153	LAND_DS_L1_TCON	0.4
GPS_RATE_MS	200	INS_GYR2OFFS_Z	-0.00098	LAND_DS_P	0
GPS_RATE_MS2	200	INS_GYR3_ID	0	LAND_DS_SLEW_SPD	0.5
GPS_RAW_DATA	0	INS_GYR3OFFS_X	0	LAND_DS_SLOPE_A	1
GPS_SAVE_CFG	2	INS_GYR3OFFS_Y	0	LAND_DS_SLOPE_B	1
GPS_SBAS_MODE	2	INS_GYR3OFFS_Z	0	LAND_DS_V_DWN	2

LAND_DS_V_FWD	1	MNT_LEAD_PTCH	0	Q_A_ANGLE_BOOST	1
LAND_DS_YAW_LIM	10	MNT_LEAD_RLL	0	Q_A_INPUT_TC	0.2
LAND_FLAP_PERCNT	0	MNT_NEUTRAL_X	0	Q_A_RAT_PIT_D	0.0036
LAND_FLARE_ALT	3	MNT_NEUTRAL_Y	0	Q_A_RAT_PIT_FF	0
LAND_FLARE_SEC	2	MNT_NEUTRAL_Z	0	Q_A_RAT_PIT_FLTD	10
LAND_PF_ALT	10	MNT_RC_IN_PAN	0	Q_A_RAT_PIT_FLTE	0
LAND_PF_ARSPD	0	MNT_RC_IN_ROLL	0	Q_A_RAT_PIT_FLTT	20
LAND_PF_SEC	6	MNT_RC_IN_TILT	0	Q_A_RAT_PIT_I	0.25
LAND_PITCH_CD	0	MNT_RETRACT_X	0	Q_A_RAT_PIT_IMAX	0.5
LAND_SLOPE_RCALC	2	MNT_RETRACT_Y	0	Q_A_RAT_PIT_P	0.25
LAND_THEN_NEUTRL	0	MNT_RETRACT_Z	0	Q_A_RAT_RLL_D	0.014396
LAND_THR_SLEW	0	MNT_STAB_PAN	0	Q_A_RAT_RLL_FF	0
LAND_TYPE	0	MNT_STAB_ROLL	0	Q_A_RAT_RLL_FLTD	10
LEVEL_ROLL_LIMIT	5	MNT_STAB_TILT	0	Q_A_RAT_RLL_FLTE	0
LGR_DEPLOY_ALT	0	MNT_TYPE	0	Q_A_RAT_RLL_FLTT	20
LGR_DEPLOY_PIN	-1	NAV_CONTROLLER	1	Q_A_RAT_RLL_I	0.336277
LGR_DEPLOY_POL	0	NAVL1_DAMPING	0.75	Q_A_RAT_RLL_IMAX	0.5
LGR_RETRACT_ALT	0	NAVL1_LIM_BANK	0	Q_A_RAT_RLL_P	0.336277
LGR_STARTUP	0	NAVL1_PERIOD	17	Q_A_RAT_YAW_D	0
LGR_WOW_PIN	-1	NAVL1_XTRACK_I	0.02	Q_A_RAT_YAW_FF	0
LGR_WOW_POL	0	NTF_BUZZ_ENABLE	1	Q_A_RAT_YAW_FLTD	0
LIM_PITCH_MAX	2000	NTF_BUZZ_ON_LVL	1	Q_A_RAT_YAW_FLTE	2.5
LIM_PITCH_MIN	-2500	NTF_BUZZ_PIN	0	Q_A_RAT_YAW_FLTT	20
LIM_ROLL_CD	4500	NTF_BUZZ_VOLUME	100	Q_A_RAT_YAW_I	0.018
LOG_BACKEND_TYPE	1	NTF_DISPLAY_TYPE	0	Q_A_RAT_YAW_IMAX	0.5
LOG_BITMASK	65535	NTF_LED_BRIGHT	3	Q_A_RAT_YAW_P	0.18
LOG_DISARMED	0	NTF_LED_OVERRIDE	0	Q_A_RATE_FF_ENAB	1
LOG_FILE_BUFSIZE	50	NTF_LED_TYPES	199	Q_A_RATE_P_MAX	0
LOG_FILE_DSRMROT	0	NTF_OREO_THEME	0	Q_A_RATE_R_MAX	0
LOG_FILE_TIMEOUT	5	OVERRIDE_CHAN	0	Q_A_RATE_Y_MAX	0
LOG_MAV_BUFSIZE	8	OVERRIDE_SAFETY	1	Q_A_SLEW_YAW	6000
LOG_REPLAY	0	PTCH2SRV_D	0.04	Q_A_THR_MIX_MAN	0.1
MANUAL_RCMASK	0	PTCH2SRV_FF	0	Q_A_THR_MIX_MAX	0.5
MIN_GNDSPD_CM	0	PTCH2SRV_I	0.3	Q_A_THR_MIX_MIN	0.1
MIS_OPTIONS	0	PTCH2SRV_IMAX	3000	Q_ACCEL_Z	250
MIS_RESTART	0	PTCH2SRV_P	1	Q_ACRO_PIT_RATE	180
MIS_TOTAL	6	PTCH2SRV_RLL	1	Q_ACRO_RLL_RATE	360
MIXING_GAIN	0.5	PTCH2SRV_RMAX_DN	0	Q_ACRO_YAW_RATE	90
MIXING_OFFSET	0	PTCH2SRV_RMAX_UP	0	Q_ANGLE_MAX	3000
MNT_ANGMAX_PAN	4500	PTCH2SRV_TCONST	0.5	Q_ASSIST_ALT	0
MNT_ANGMAX_ROL	4500	Q_A_ACCEL_P_MAX	110000	Q_ASSIST_ANGLE	30
MNT_ANGMAX_TIL	4500	Q_A_ACCEL_R_MAX	38530.14	Q_ASSIST_SPEED	20
MNT_ANGMIN_PAN	-4500	Q_A_ACCEL_Y_MAX	27000	Q_AUTOTUNE_AGGR	0.1
MNT_ANGMIN_ROL	-4500	Q_A_ANG_LIM_TC	1	Q_AUTOTUNE_AXES	4
MNT_ANGMIN_TIL	-4500	Q_A_ANG_PIT_P	4.5	Q_AUTOTUNE_MIN_D	0.001
MNT_DEFLT_MODE	3	Q_A_ANG_RLL_P	6.926874	Q_ENABLE	1
MNT_JSTICK_SPD	0	Q_A_ANG_YAW_P	4.5	Q_ESC_CAL	0

Q_FRAME_CLASS	1	Q_P_POSZ_P	1	Q_WVANE_GAIN	0
Q_FRAME_TYPE	1	Q_P_VELXY_D	0.35	Q_WVANE_MINROLL	1
Q_FW_LND_APR_RAD	0	Q_P_VELXY_D_FILT	5	Q_YAW_RATE_MAX	100
Q_GUIDED_MODE	1	Q_P_VELXY_FILT	5	RALLY_INCL_HOME	0
Q_LAND_FINAL_ALT	6	Q_P_VELXY_I	0.7	RALLY_LIMIT_KM	5
Q_LAND_ICE_CUT	1	Q_P_VELXY_IMAX	1000	RALLY_TOTAL	0
Q_LAND_SPEED	50	Q_P_VELXY_P	1.4	RC_OPTIONS	0
Q_LOIT_ACC_MAX	250	Q_P_VELZ_P	5	RC_OVERRIDE_TIME	3
Q_LOIT_ANG_MAX	15	Q_RC_SPEED	490	RC1_DZ	30
Q_LOIT_BRK_ACCEL	50	Q_RTL_ALT	15	RC1_MAX	1919
Q_LOIT_BRK_DELAY	1	Q_RTL_MODE	0	RC1_MIN	1070
Q_LOIT_BRK_JERK	250	Q_TAILSIT_ANGLE	45	RC1_OPTION	0
Q_LOIT_SPEED	500	Q_TAILSIT_INPUT	0	RC1_REVERSED	0
Q_M_BAT_CURR_MAX	0	Q_TAILSIT_MASK	0	RC1_TRIM	1494
Q_M_BAT_CURR_TC	5	Q_TAILSIT_MASKCH	0	RC10_DZ	0
Q_M_BAT_IDX	0	Q_TAILSIT_MOTMX	0	RC10_MAX	1900
Q_M_BAT_VOLT_MAX	0	Q_TAILSIT_RLL_MX	0	RC10_MIN	1100
Q_M_BAT_VOLT_MIN	0	Q_TAILSIT_THSCMX	5	RC10_OPTION	0
Q_M_BOOST_SCALE	0	Q_TAILSIT_VFGAIN	0	RC10_REVERSED	0
Q_M_HOVER_LEARN	2	Q_TAILSIT_VHGAIN	0.5	RC10_TRIM	0
Q_M_PWM_MAX	0	Q_TAILSIT_VHPOW	2.5	RC11_DZ	0
Q_M_PWM_MIN	0	Q_THR_MAX_PWM	2000	RC11_MAX	1900
Q_M_PWM_TYPE	0	Q_THR_MIN_PWM	1000	RC11_MIN	1100
Q_M_SAFE_DISARM	0	Q_THROTTLE_EXPO	0.2	RC11_OPTION	0
Q_M_SAFE_TIME	1	Q_TILT_MASK	0	RC11_REVERSED	0
Q_M_SLEW_DN_TIME	0	Q_TILT_MAX	45	RC11_TRIM	0
Q_M_SLEW_UP_TIME	0	Q_TILT_RATE_DN	0	RC12_DZ	0
Q_M_SPIN_ARM	0.12	Q_TILT_RATE_UP	40	RC12_MAX	1900
Q_M_SPIN_MAX	0.95	Q_TILT_TYPE	0	RC12_MIN	1100
Q_M_SPIN_MIN	0.15	Q_TILT_YAW_ANGLE	0	RC12_OPTION	0
Q_M_SPOOL_TIME	0.25	Q_TKOFF_ARSP_LIM	0	RC12_REVERSED	0
Q_M_THST_EXPO	0.65	Q_TKOFF_FAIL_SCL	0	RC12_TRIM	0
Q_M_THST_HOVER	0.3059293	Q_TRAN_PIT_MAX	3	RC13_DZ	0
Q_M_YAW_HEADROOM	200	Q_TRANS_DECEL	2	RC13_MAX	1900
Q_MAV_TYPE	0	Q_TRANS_FAIL	0	RC13_MIN	1100
Q_OPTIONS	0	Q_TRANSITION_MS	5000	RC13_OPTION	0
Q_P_ACC_XY_FILT	2	Q_TRIM_PITCH	0	RC13_REVERSED	0
Q_P_ACCZ_D	0	Q_VELZ_MAX	250	RC13_TRIM	0
Q_P_ACCZ_FF	0	Q_VFWD_ALT	0	RC14_DZ	0
Q_P_ACCZ_FLTD	0	Q_VFWD_GAIN	0	RC14_MAX	1900
Q_P_ACCZ_FLTE	10	Q_WP_ACCEL	100	RC14_MIN	1100
Q_P_ACCZ_FLTT	0	Q_WP_ACCEL_Z	100	RC14_OPTION	0
Q_P_ACCZ_I	1	Q_WP_RADIUS	50	RC14_REVERSED	0
Q_P_ACCZ_IMAX	800	Q_WP_RFND_USE	1	RC14_TRIM	0
Q_P_ACCZ_P	0.3	Q_WP_SPEED	100	RC15_DZ	0
Q_P_ANGLE_MAX	0	Q_WP_SPEED_DN	50	RC15_MAX	1900
Q_P_POSXY_P	1	Q_WP_SPEED_UP	50	RC15_MIN	1100

RC15_OPTION	0	RC8_MIN	1085	RNGFND2_GNDCLEAR	10
RC15_REVERSED	0	RC8_OPTION	0	RNGFND2_MAX_CM	700
RC15_TRIM	0	RC8_REVERSED	0	RNGFND2_MIN_CM	20
RC16_DZ	0	RC8_TRIM	1919	RNGFND2_OFFSET	0
RC16_MAX	1900	RC9_DZ	0	RNGFND2_ORIENT	25
RC16_MIN	1100	RC9_MAX	1900	RNGFND2_PIN	-1
RC16_OPTION	0	RC9_MIN	1100	RNGFND2_POS_X	0
RC16_REVERSED	0	RC9_OPTION	0	RNGFND2_POS_Y	0
RC16_TRIM	0	RC9_REVERSED	0	RNGFND2_POS_Z	0
RC2_DZ	30	RC9_TRIM	0	RNGFND2_PWRRNG	0
RC2_MAX	1917	RCMAP_PITCH	2	RNGFND2_RMETRIC	1
RC2_MIN	1070	RCMAP_ROLL	1	RNGFND2_SCALING	3
RC2_OPTION	0	RCMAP_THROTTLE	3	RNGFND2_STOP_PIN	-1
RC2_REVERSED	1	RCMAP_YAW	4	RNGFND2_TYPE	0
RC2_TRIM	1494	RELAY_DEFAULT	0	RNGFND3_ADDR	0
RC3_DZ	30	RELAY_PIN	-1	RNGFND3_FUNCTION	0
RC3_MAX	1916	RELAY_PIN2	-1	RNGFND3_GNDCLEAR	10
RC3_MIN	1072	RELAY_PIN3	-1	RNGFND3_MAX_CM	700
RC3_OPTION	0	RELAY_PIN4	-1	RNGFND3_MIN_CM	20
RC3_REVERSED	0	RELAY_PIN5	-1	RNGFND3_OFFSET	0
RC3_TRIM	1080	RELAY_PIN6	-1	RNGFND3_ORIENT	25
RC4_DZ	30	RLL2SRV_D	0.08	RNGFND3_PIN	-1
RC4_MAX	1916	RLL2SRV_FF	0	RNGFND3_POS_X	0
RC4_MIN	1069	RLL2SRV_I	0.3	RNGFND3_POS_Y	0
RC4_OPTION	0	RLL2SRV_IMAX	3000	RNGFND3_POS_Z	0
RC4_REVERSED	0	RLL2SRV_P	1	RNGFND3_PWRRNG	0
RC4_TRIM	1493	RLL2SRV_RMAX	0	RNGFND3_RMETRIC	1
RC5_DZ	0	RLL2SRV_TCONST	0.5	RNGFND3_SCALING	3
RC5_MAX	1919	RNGFND_LANDING	0	RNGFND3_STOP_PIN	-1
RC5_MIN	1070	RNGFND1_ADDR	0	RNGFND3_TYPE	0
RC5_OPTION	41	RNGFND1_FUNCTION	0	RNGFND4_ADDR	0
RC5_REVERSED	0	RNGFND1_GNDCLEAR	10	RNGFND4_FUNCTION	0
RC5_TRIM	1070	RNGFND1_MAX_CM	700	RNGFND4_GNDCLEAR	10
RC6_DZ	0	RNGFND1_MIN_CM	20	RNGFND4_MAX_CM	700
RC6_MAX	1848	RNGFND1_OFFSET	0	RNGFND4_MIN_CM	20
RC6_MIN	1070	RNGFND1_ORIENT	25	RNGFND4_OFFSET	0
RC6_OPTION	0	RNGFND1_PIN	-1	RNGFND4_ORIENT	25
RC6_REVERSED	0	RNGFND1_POS_X	0	RNGFND4_PIN	-1
RC6_TRIM	1071	RNGFND1_POS_Y	0	RNGFND4_POS_X	0
RC7_DZ	0	RNGFND1_POS_Z	0	RNGFND4_POS_Y	0
RC7_MAX	1919	RNGFND1_PWRRNG	0	RNGFND4_POS_Z	0
RC7_MIN	1070	RNGFND1_RMETRIC	1	RNGFND4_PWRRNG	0
RC7_OPTION	0	RNGFND1_SCALING	3	RNGFND4_RMETRIC	1
RC7_REVERSED	0	RNGFND1_STOP_PIN	-1	RNGFND4_SCALING	3
RC7_TRIM	1070	RNGFND1_TYPE	0	RNGFND4_STOP_PIN	-1
RC8_DZ	0	RNGFND2_ADDR	0	RNGFND4_TYPE	0
RC8_MAX	1919	RNGFND2_FUNCTION	0	RNGFND5_ADDR	0

RNGFND5_FUNCTION	0	RNGFND8_ADDR	0	RNGFNDA_TYPE	0
RNGFND5_GNDCLEAR	10	RNGFND8_FUNCTION	0	RPM_MAX	100000
RNGFND5_MAX_CM	700	RNGFND8_GNDCLEAR	10	RPM_MIN	10
RNGFND5_MIN_CM	20	RNGFND8_MAX_CM	700	RPM_MIN_QUAL	0.5
RNGFND5_OFFSET	0	RNGFND8_MIN_CM	20	RPM_PIN	54
RNGFND5_ORIENT	25	RNGFND8_OFFSET	0	RPM_SCALING	1
RNGFND5_PIN	-1	RNGFND8_ORIENT	25	RPM_TYPE	0
RNGFND5_POS_X	0	RNGFND8_PIN	-1	RPM2_PIN	-1
RNGFND5_POS_Y	0	RNGFND8_POS_X	0	RPM2_SCALING	1
RNGFND5_POS_Z	0	RNGFND8_POS_Y	0	RPM2_TYPE	0
RNGFND5_PWRRNG	0	RNGFND8_POS_Z	0	RSSI_TYPE	0
RNGFND5_RMETRIC	1	RNGFND8_PWRRNG	0	RST_MISSION_CH	0
RNGFND5_SCALING	3	RNGFND8_RMETRIC	1	RST_SWITCH_CH	0
RNGFND5_STOP_PIN	-1	RNGFND8_SCALING	3	RTL_AUTOLAND	0
RNGFND5_TYPE	0	RNGFND8_STOP_PIN	-1	RTL_RADIUS	0
RNGFND6_ADDR	0	RNGFND8_TYPE	0	RUDD_DT_GAIN	10
RNGFND6_FUNCTION	0	RNGFND9_ADDR	0	RUDDER_ONLY	0
RNGFND6_GNDCLEAR	10	RNGFND9_FUNCTION	0	SCALING_SPEED	15
RNGFND6_MAX_CM	700	RNGFND9_GNDCLEAR	10	SCHED_DEBUG	0
RNGFND6_MIN_CM	20	RNGFND9_MAX_CM	700	SCHED_LOOP_RATE	300
RNGFND6_OFFSET	0	RNGFND9_MIN_CM	20	SCR_ENABLE	0
RNGFND6_ORIENT	25	RNGFND9_OFFSET	0	SERIAL_PASS1	0
RNGFND6_PIN	-1	RNGFND9_ORIENT	25	SERIAL_PASS2	-1
RNGFND6_POS_X	0	RNGFND9_PIN	-1	SERIAL_PASSTIMO	15
RNGFND6_POS_Y	0	RNGFND9_POS_X	0	SERIAL0_BAUD	115
RNGFND6_POS_Z	0	RNGFND9_POS_Y	0	SERIAL0_PROTOCOL	2
RNGFND6_PWRRNG	0	RNGFND9_POS_Z	0	SERIAL1_BAUD	57
RNGFND6_RMETRIC	1	RNGFND9_PWRRNG	0	SERIAL1_OPTIONS	0
RNGFND6_SCALING	3	RNGFND9_RMETRIC	1	SERIAL1_PROTOCOL	1
RNGFND6_STOP_PIN	-1	RNGFND9_SCALING	3	SERIAL2_BAUD	57
RNGFND6_TYPE	0	RNGFND9_STOP_PIN	-1	SERIAL2_OPTIONS	0
RNGFND7_ADDR	0	RNGFND9_TYPE	0	SERIAL2_PROTOCOL	1
RNGFND7_FUNCTION	0	RNGFNDA_ADDR	0	SERIAL3_BAUD	38
RNGFND7_GNDCLEAR	10	RNGFNDA_FUNCTION	0	SERIAL3_OPTIONS	0
RNGFND7_MAX_CM	700	RNGFNDA_GNDCLEAR	10	SERIAL3_PROTOCOL	5
RNGFND7_MIN_CM	20	RNGFNDA_MAX_CM	700	SERIAL4_BAUD	38
RNGFND7_OFFSET	0	RNGFNDA_MIN_CM	20	SERIAL4_OPTIONS	0
RNGFND7_ORIENT	25	RNGFNDA_OFFSET	0	SERIAL4_PROTOCOL	5
RNGFND7_PIN	-1	RNGFNDA_ORIENT	25	SERIAL5_BAUD	57
RNGFND7_POS_X	0	RNGFNDA_PIN	-1	SERIAL5_OPTIONS	0
RNGFND7_POS_Y	0	RNGFNDA_POS_X	0	SERIAL5_PROTOCOL	-1
RNGFND7_POS_Z	0	RNGFNDA_POS_Y	0	SERIAL6_BAUD	57
RNGFND7_PWRRNG	0	RNGFNDA_POS_Z	0	SERIAL6_OPTIONS	0
RNGFND7_RMETRIC	1	RNGFNDA_PWRRNG	0	SERIAL6_PROTOCOL	-1
RNGFND7_SCALING	3	RNGFNDA_RMETRIC	1	SERIAL7_BAUD	115200
RNGFND7_STOP_PIN	-1	RNGFNDA_SCALING	3	SERIAL7_OPTIONS	0
RNGFND7_TYPE	0	RNGFNDA_STOP_PIN	-1	SERIAL7_PROTOCOL	2

SERVO_AUTO_TRIM	0	SERVO15_MAX	1900	SERVO9_REVERSED	0
SERVO_BLH_AUTO	0	SERVO15_MIN	1100	SERVO9_TRIM	1500
SERVO_BLH_DEBUG	0	SERVO15_REVERSED	0	SOAR_ENABLE	0
SERVO_BLH_MASK	0	SERVO15_TRIM	1500	SR0_ADSB	5
SERVO_BLH_OTYPE	0	SERVO16_FUNCTION	0	SR0_EXT_STAT	1
SERVO_BLH_POLES	14	SERVO16_MAX	1900	SR0_EXTRA1	1
SERVO_BLH_PORT	0	SERVO16_MIN	1100	SR0_EXTRA2	1
SERVO_BLH_REMASK	0	SERVO16_REVERSED	0	SR0_EXTRA3	1
SERVO_BLH_TEST	0	SERVO16_TRIM	1500	SR0_PARAMS	10
SERVO_BLH_TMOUT	0	SERVO2_FUNCTION	19	SR0_POSITION	1
SERVO_BLH_TRATE	10	SERVO2_MAX	1900	SR0_RAW_CTRL	1
SERVO_RATE	50	SERVO2_MIN	1100	SR0_RAW_SENS	1
SERVO_ROB_POSMAX	4095	SERVO2_REVERSED	0	SR0_RC_CHAN	1
SERVO_ROB_POSMIN	0	SERVO2_TRIM	1500	SR1_ADSB	5
SERVO_SBUS_RATE	50	SERVO3_FUNCTION	70	SR1_EXT_STAT	2
SERVO_VOLZ_MASK	0	SERVO3_MAX	1900	SR1_EXTRA1	4
SERVO1_FUNCTION	4	SERVO3_MIN	1100	SR1_EXTRA2	4
SERVO1_MAX	1900	SERVO3_REVERSED	0	SR1_EXTRA3	2
SERVO1_MIN	1100	SERVO3_TRIM	1100	SR1_PARAMS	10
SERVO1_REVERSED	1	SERVO4_FUNCTION	21	SR1_POSITION	2
SERVO1_TRIM	1500	SERVO4_MAX	1900	SR1_RAW_CTRL	1
SERVO10_FUNCTION	0	SERVO4_MIN	1100	SR1_RAW_SENS	2
SERVO10_MAX	1900	SERVO4_REVERSED	1	SR1_RC_CHAN	2
SERVO10_MIN	1100	SERVO4_TRIM	1500	SR2_ADSB	5
SERVO10_REVERSED	0	SERVO5_FUNCTION	33	SR2_EXT_STAT	1
SERVO10_TRIM	1500	SERVO5_MAX	1900	SR2_EXTRA1	1
SERVO11_FUNCTION	0	SERVO5_MIN	1100	SR2_EXTRA2	1
SERVO11_MAX	1900	SERVO5_REVERSED	0	SR2_EXTRA3	1
SERVO11_MIN	1100	SERVO5_TRIM	1500	SR2_PARAMS	10
SERVO11_REVERSED	0	SERVO6_FUNCTION	34	SR2_POSITION	1
SERVO11_TRIM	1500	SERVO6_MAX	1900	SR2_RAW_CTRL	1
SERVO12_FUNCTION	0	SERVO6_MIN	1100	SR2_RAW_SENS	1
SERVO12_MAX	1900	SERVO6_REVERSED	0	SR2_RC_CHAN	1
SERVO12_MIN	1100	SERVO6_TRIM	1500	SR3_ADSB	5
SERVO12_REVERSED	0	SERVO7_FUNCTION	35	SR3_EXT_STAT	2
SERVO12_TRIM	1500	SERVO7_MAX	1900	SR3_EXTRA1	4
SERVO13_FUNCTION	0	SERVO7_MIN	1100	SR3_EXTRA2	4
SERVO13_MAX	1900	SERVO7_REVERSED	0	SR3_EXTRA3	2
SERVO13_MIN	1100	SERVO7_TRIM	1500	SR3_PARAMS	10
SERVO13_REVERSED	0	SERVO8_FUNCTION	36	SR3_POSITION	2
SERVO13_TRIM	1500	SERVO8_MAX	1900	SR3_RAW_CTRL	1
SERVO14_FUNCTION	0	SERVO8_MIN	1100	SR3_RAW_SENS	2
SERVO14_MAX	1900	SERVO8_REVERSED	0	SR3_RC_CHAN	2
SERVO14_MIN	1100	SERVO8_TRIM	1500	STAB_PITCH_DOWN	2
SERVO14_REVERSED	0	SERVO9_FUNCTION	0	STALL_PREVENTION	1
SERVO14_TRIM	1500	SERVO9_MAX	1900	STAT_BOOTCNT	51
SERVO15_FUNCTION	0	SERVO9_MIN	1100	STAT_FLTTIME	3201

STAT_RESET	1.23E+08	TERRAIN_ENABLE	1	YAW2SRV_RLL	1
STAT_RUNTIME	24530	TERRAIN_FOLLOW	0	YAW2SRV_SLIP	0
STEER2SRV_D	0.005	TERRAIN_LOOKAHD	2000		
STEER2SRV_DRTFCT	10	TERRAIN_SPACING	100		
STEER2SRV_DRTMIN	4500	THR_FAILSAFE	1		
STEER2SRV_DRTSPD	0	THR_FS_VALUE	950		
STEER2SRV_FF	0	THR_MAX	15		
STEER2SRV_I	0.2	THR_MIN	0		
STEER2SRV_IMAX	1500	THR_PASS_STAB	0		
STEER2SRV_MINSPD	1	THR_SLEWRATE	100		
STEER2SRV_P	1.8	THR_SUPP_MAN	0		
STEER2SRV_TCONST	0.75	THROTTLE_NUDGE	1		
STICK_MIXING	1	TKOFF_ACCEL_CNT	1		
SYS_NUM_RESETS	69	TKOFF_ALT	50		
SYSID_ENFORCE	0	TKOFF_DIST	200		
SYSID_MYGCS	255	TKOFF_FLAP_PCNT	0		
SYSID_THISMAV	1	TKOFF_LVL_ALT	20		
TECS_APPR_SMAX	0	TKOFF_LVL_PITCH	15		
TECS_CLMB_MAX	5	TKOFF_PLIM_SEC	2		
TECS_HGT_OMEGA	3	TKOFF_ROTATE_SPD	0		
TECS_INTEG_GAIN	0.1	TKOFF_TDRAG_ELEV	0		
TECS_LAND_ARSPD	-1	TKOFF_TDRAG_SPD1	0		
TECS_LAND_DAMP	0.5	TKOFF_THR_DELAY	2		
TECS_LAND_IGAIN	0	TKOFF_THR_MAX	0		
TECS_LAND_PDAMP	0	TKOFF_THR_MINACC	0		
TECS_LAND_PMAX	10	TKOFF_THR_MINSPD	0		
TECS_LAND_SINK	0.25	TKOFF_THR_SLEW	0		
TECS_LAND_SPDWGT	-1	TKOFF_TIMEOUT	0		
TECS_LAND_SRC	0	TRIM_ARSPD_CM	1500		
TECS_LAND_TCONST	2	TRIM_AUTO	0		
TECS_LAND_TDAMP	0	TRIM_PITCH_CD	0		
TECS_LAND_THR	-1	TRIM_THROTTLE	50		
TECS_OPTIONS	0	TUNE_CHAN	0		
TECS_PITCH_MAX	15	TUNE_CHAN_MAX	2000		
TECS_PITCH_MIN	0	TUNE_CHAN_MIN	1000		
TECS_PTCH_DAMP	0	TUNE_ERR_THRESH	0.15		
TECS_RLL2THR	10	TUNE_MODE_REVERT	1		
TECS_SINK_MAX	5	TUNE_PARAM	0		
TECS_SINK_MIN	2	TUNE_RANGE	2		
TECS_SPD_OMEGA	2	TUNE_SELECTOR	0		
TECS_SPDWEIGHT	1	USE_REV_THRUST	2		
TECS_SYNAIRSPEED	0	WP_LOITER_RAD	60		
TECS_THR_DAMP	0.5	WP_MAX_RADIUS	0		
TECS_TIME_CONST	5	WP_RADIUS	2		
TECS_TKOFF_IGAIN	0	YAW2SRV_DAMP	0		
TECS_VERT_ACC	7	YAW2SRV_IMAX	1500		
TELEM_DELAY	0	YAW2SRV_INT	0		

Appendix B

Concept of Operations

LAB-SCALE AIRBORNE WIND ENERGY PROTOTYPE

CONCEPT OF OPERATION

QUADPLANE

Summary

Airborne Wind Energy Systems (AWES) can harness the power of the wind using a tethered plane or kite. Crosswind flight generates high tether tension that drives a winch-generator system. We have developed a lab-scale prototype with the goal of proving the concept and validating the flight models. The vehicle is a hybrid between a quadcopter and a fixed-wing plane, namely a quadplane. It allows vertical take-off and landing (VTOL) as well as crosswind flight. The quadplane has been structurally reinforced for crosswind flight and enhanced for autonomous operation. The quadplane must be tuned in quadcopter and fixed-wing flight prior to tethered. The concept of operation in this document defines the objective, what role is performed by the crew members, checks performed before the operation, and pre-flight briefing. The site survey contains a description of the flight area, along with the steps to be performed before the beginning of the operation. The emergency procedures describe the potential scenarios that could occur during the operation along with executable contingency countermeasures. Finally, the testing procedures explain the intended flight plan in detail.

CONCEPT OF OPERATIONS

Purpose

This document provides the information required to perform a safe operation. It is structured as follows:

1. Concept of Operations
    - 1.1. Crew coordination: description of the crew roles and responsibilities
    - 1.2. Pre-operation checks: Check performed prior to the operation day
    - 1.3. Briefings: Information provided to the crew before the beginning of each flight test
    - 1.4. Aircraft specifications: estimated performance of the aircraft
2. Site Survey
    - 2.1. Flight area: description of the testing site
    - 2.2. Site survey on operation day: steps to follow to ensure the site is appropriate for the operation
3. Emergency Procedures
    - 3.1. Potential scenarios and countermeasures
4. Flight Procedures
    - 4.1. Pre-flight checks: task list to be performed before each flight
    - 4.2. Test Cards: describe in detail the intended test flight
    - 4.3. Post-flight checks: tasks performed after each flight

The goal of the AWES prototype is to validate the flight simulation performed with the incorporation of the tether dynamics to the plane physics model. In addition, provide technical, hands-on experience in the development of this novel technology for a better understanding of the overall system. Finally, the platform will serve the purpose of proving the concept of being able to develop a small scale Airborne Wind Energy device with relatively low investment.

Crew Definitions

Each member of the operation crew must take one of the following roles. This is decided by the Test Director prior to the testing day, each member must be clear and in agreement of their role before the operation begins.

Test Director (TD)

- Coordinates the test flight.
- Verifies weather and crew readiness.
- Defines the operation and its objectives.
- Gives the flight plan briefings and distributes the test cards

Pilot In Command (PIC)

- Is directly responsible and is the final authority as to the operation of the aircraft.
- Is the final authority as to the operation of the aircraft.
- Ensures the safety of the crew, external individuals, and property in case of losing control over the aircraft.
- Ensure compliance of the applicable rules and regulations.
- Inspect the aircraft before each flight (pre-flight checks).
- Commands take-off.
- Is in manual control of the aircraft through RC transmitter in a manual operation.
- Is in control of the aircraft through the ground control software in an autonomous operation.
- Is responsible for conducting emergency procedures if needed.
- Performs the post-flight checks.

Visual Observer (VO)

- Maintain line of sight with the aircraft at all times.
- Notifies the crew in case of an unexpected event or abnormalities during flight.

Range Safety Officer (RSO)

- Performs the site inspection

- Provides oversight of the airspace in use
- In command of radio communications
- Notifies the crew if manned aircraft is approaching the flight zone
- Notifies the public entering the flight zone
- Notifies air traffic control in case of emergency

Ground Crew (GC)

- Set up equipment and cameras for the test.

Briefings

The objective of briefings is to inform the operation crew of the intended plan. This involves describing what is going to be done, how it is going to be done, and the safety considerations. Test cards must be distributed to the crew members during the briefing. The briefings should follow a simple structure as presented below.

1. Purpose of the operation
2. Operation roles confirmation
3. Flight plan description
    a. Flight tests description
4. Questions and concerns

Vehicle Specifications

The vehicle consists of a combination of a fixed-wing plane with a quadcopter, commonly called a quadplane. The Volantex Phoenix V2 off-the-shelf model airplane was structurally reinforced for tethered flight, and for supporting the mounting of a quadcopter frame. It has a wingspan is 2 meters and a total weight of 3.6 kg. The thrust to weight ratio of the quadcopter motors is approximately 2.5, allowing hover at 40% vertical thrust. The battery type is a 4-cell Lithium-Polymer with 5000mAh capacity. Allowing approximately 6 minutes of hover time. The expected trim speed is around 15 m/s with a zero degree angle of attack and 40% throttle. The estimated stall speed is 11m/s at 90% throttle and 10 deg angle of attack. The stall speed is reduced to zero if the VTOL motors provide assistance during forward flight. A summary of the estimated aircraft performance is provided in the table below.

Fixed-Wing		Quadcopter	
Trim speed	15 m/s	Climb speed	3 m/s
Trim throttle	40%	Hover throttle	40%
Max. Speed	25 m/s	Max. Climb speed	10 m/s
Stall speed	11 m/s	Descent speed	3 m/s
Stall AOA	10°	Max. Descent speed	9 m/s
Cruise time	20 min	Hover time	6 min

CHECKLISTS

Pre-Operation checks

Before the operation day ensure that the following steps are completed.

- ❏ Inspect aircraft for:
  - ❏ Structural damage
  - ❏ Loose components such as bolts, motor mounts, boom mounts, flight controller, telemetry and radio systems, airspeed sensor, GPS, motors, propellers, and servos.
  - ❏ Disconnected linkages in ailerons, elevator, and rudder
  - ❏ Disconnected cables or pitot airlines
  - ❏ Free rotation of motors and control surfaces
- ❏ Check flight batteries charge
- ❏ Check RC transmitter battery charge
- ❏ Check field laptop battery charge
- ❏ Check proper ground station software operation
- ❏ Check telemetry connection
- ❏ Check that the documentation folder contains:
  - ❏ Concept of operations
  - ❏ Checklists
  - ❏ Emergency procedures
  - ❏ Site survey
  - ❏ Flight plan and test objectives
  - ❏ Aircraft registration
  - ❏ Pilot certification
  - ❏ Flight Log
  - ❏ Maintenance Log
- ❏ Check the expected weather conditions for the next day
- ❏ Confirm with the involved crew members

Packing list

Check that the field tool kit contains:

- ❏ Documentation folder
    - ❏ Concept of operations
    - ❏ Checklists
    - ❏ Emergency procedures
    - ❏ Site survey
    - ❏ Flight plan and test objectives
    - ❏ Aircraft registration
    - ❏ Pilot certification
    - ❏ Flight Log
    - ❏ Maintenance Log
- ❏ #3 Square screwdriver (motor and boom mounts)
- ❏ ¼" wrench (motor mounts)
- ❏ Phillips screwdriver (fuselage cover)
- ❏ #10 hex key die with a ratchet (propellers),
- ❏ Cable clipper (removing transport foam)
- ❏ Field laptop with charger
- ❏ Telemetry system with a micro USB cable
- ❏ RC transmitter and additional batteries
- ❏ Aircraft batteries in safety fireproof container
- ❏ Fire extinguisher
- ❏ Air horn
- ❏ First aid kit
- ❏ VHF radio
- ❏ High visibility safety vest (one per each crew member)
- ❏ Safety glasses (one per each crew member)
- ❏ Charged cell phones
- ❏ Additional motor mount screws and nuts
- ❏ Additional fuselage cover screws
- ❏ Additional propeller nuts

- ❏ Cable ties
- ❏ Electrical tape
- ❏ Duct tape
- ❏ Garbage bag
- ❏ Paper towel
- ❏ Cameras

Pre-flight Checks

Perform the following actions before each flight test.

- ❏ Inspect aircraft for:
    - ❏ Loose parts (bolts, electronics, wires, propellers)
    - ❏ Loose connections
    - ❏ Servo linkages
    - ❏ Free motor rotation
    - ❏ Free servo rotation
- ❏ Check LiPo battery levels is over 4.15V per cell
- ❏ Check RC transmitter battery levels
- ❏ Verify correct operation of the ground control software
- ❏ Verify connection between aircraft and ground control software
- ❏ Verify connection between aircraft and RC transmitter
- ❏ Verify servo direction
- ❏ Verify motor direction
- ❏ Verify pitch, roll, yaw rotations
- ❏ Perform pre-flight calibration (cover airspeed sensor)
- ❏ Verify GPS lock
- ❏ Verify airspeed measurement (noise under 3 m/s)
- ❏ Verify AHRS (Altitude Heading Reference System)
- ❏ Verify EKF
- ❏ Load and write parameter file
- ❏ Load and write mission file
- ❏ Notify crew pre-flight checks has been completed

During Flight Checks

Perform the following actions during each flight.

Every 10 seconds	❏ Verify airspeed ❏ Verify ground speed ❏ Verify throttle ❏ Verify altitude
Every 30 seconds	❏ Verify battery voltage ❏ Verify communication signal strength (strong, medium, low) ❏ Verify target heading (waypoint)
When achieved	❏ Notify when vehicle is armed ❏ Notify when vertical take-off completed ❏ Notify when transition to forward flight completed ❏ Notify when waypoint # reached ❏ Notify when transition into hover completed ❏ Notify when landing completed ❏ Notify when vehicle disarmed
If arises	❏ Notify crew of low battery warning ❏ Notify crew of loss of connectivity ❏ Notify crew of incorrect or unexpected sensor data ❏ Notify crew of emergency procedures executed

Post-flight Checks

Perform the following actions after each flight test.

- ❏ Recover aircraft from landing area
- ❏ Unplug battery
- ❏ Remove and inspect battery, place in a fire-safe container
- ❏ Inspect aircraft for:
    - ❏ Structural damage
    - ❏ Loose parts
    - ❏ Disconnected wires
    - ❏ Disconnected servo linkages
    - ❏ Power electronic temperature level
- ❏ Transfer recorded data by connecting USB cable directly into the flight controller and using the Mission Planner option “Download DataFlash Log Via Mavlink” in the DataFlash Logs tab
- ❏ Rename the downloaded file with the test flight reference number

Post-flight Analysis

This step is performed after the operation is finished. The goal is to evaluate the flight logs compared with the test flight simulations. Aircraft parameters such as trim speed and throttle can be identified and implemented as flight controller parameter in further flights.

Analyze the following variables

- Reference and actual position (lat,long,alt)
- Trajectory
- Reference and actual attitude
- Quad and plane throttle
- Airspeed and ground speed
- Linear and rotational accelerations
- Battery voltage

SITE SURVEY

Flight Area

The potential flight area is located off the British Columbia Highway 14. It has a clear logged area of approximately 340,000 m^2 (google maps measurement), bordered by trees under 20 meters high to the north, east, and west. The figure below showing dense vegetation is outdated, and it doesn't show the clear area. The highway borders the area to the south where the power lines run parallel to the highway at under 20 meters high. A logging road provides access from the highway to the center of the area. The landowner is still unknown, efforts are currently being made to make contact and ask for permission for daily use.

On inspection day, the wind was coming from the east. The terrain contains loose logs and tree stumps, preventing horizontal landing procedures. The access logging road ends in a clear area of approximately 10-meter diameter ideal for vertical take-off and landing

Potential plane recovery within the area can be done by walking to its location. However, walking on terrain could be challenging due to irregularities and loose logging debris.

There is a low likelihood of people entering the flight area. A possible scenario could be people stopping on the highway shoulder and entering the flight area from the south, or landowner approaching from the logging road to the take-off site.

Site survey on operation day

A site survey is performed before the operation of the quadplane, with the objective of determining that the location is suitable to carry-on the operation. The following tasks must be performed by the Ground Support crew member:

1. Determine a suitable take-off, landing location.
2. Define the boundaries of the area of operation.
3. Identify the location type of airspace and comply with the respective regulatory requirements.
4. Define the altitudes and routes used during the operation.
5. Verify the location of air traffic.
6. Inspect the site for potential obstacles and hazards such as trees, wires, masts, towers, and buildings.
7. Inspect the site for bystanders and animals that can potentially come in interaction with the vehicle.
8. Verify that the weather conditions are appropriate for the operation.
9. Inspect the area and determine the potential recovery routes in case of a crash.

EMERGENCY PROCEDURES

This section describes possible scenarios that can put in risk the operation, the pilot and crew, and 3rd party people. And the actions that should be taken in case of occurring.

Fly away or loss of line of sight

1. Switch flight mode to RTL on RC transmitter
2. Switch flight mode to RTL on Mission Planner
3. Wait 1 second for Short Failsafe to activate
4. Wait 10 second for Long Failsafe to activate
5. If the plane is still not responsive, attempt to shut down the motors by Disarming to allow gliding descent
6. Inform air traffic control if possible at 1-613-563-5588 (NAV Canada)
    a. Reporting fly-away RPAS, last known location is 2 km East of Shirley, on the British Columbia Highway 14, heading LAST KNOW HEADING, at LAST KNOWN SPEED, and ALTITUDE high, with an expected range of no more than 15 minutes. The aircraft is a 2-meter wingspan foam plane with quadcopter motors the wings are blue, with red and orange stripes.
7. Attempt to recover the aircraft
8. Remove battery
9. Perform post-flight check
10. Submit an incident report

Loss of Aircraft Control: Aircraft not responding to the pilot's control

1. Wait 1 second for Short Failsafe to activate
2. Wait 10 second for Long Failsafe to activate
3. Switch flight mode to RTL
4. Turn off and on RC transmitter
5. Switch flight mode to RTL on Mission Planner
6. If is safe to do so, attempt to disarm motors
7. Inform air traffic control if possible at 1-613-563-5588 (NAV Canada)
    a. Reporting fly-away RPAS, last known location is 2 km East of Shirley, on the British Columbia Highway 14, heading LAST KNOW HEADING, at LAST KNOWN SPEED, and ALTITUDE high, with an expected range of no more than 15 minutes. The aircraft is a 2-meter wingspan foam plane with quadcopter motors the wings are blue, with red and orange stripes.
8. Recover aircraft
9. Remove battery
10. Perform post-flight checks

Loss of Power: Empty battery or motor malfunction

1. Perform circular maneuver to attempt gliding down into safe landing area
2. Disarm
3. Recover the aircraft

4. Remove the battery
5. Perform post-flight checks

Deviation from flight path in fixed-wing mode: aircraft diverges from intended trajectory

1. Bring aircraft to trimmed flight
2. Navigate the aircraft toward the landing area
3. Switch flight mode to QHOVER
4. Navigate the aircraft to the landing area
5. Vertically land
6. Disarm
7. Remove battery
8. Perform post-flight checks

Unexpected VTOL and hover behavior: aircraft in quadcopter mode deviates from trajectory

1. Switch mode to QHOVER
2. Attempt to bring the aircraft to hover
3. Land in the designated landing area or rally point
4. Disarm
5. Recover the aircraft
6. Remove the battery
7. Perform post-flight checks

Unsuccessful transition to forward flight: Quadplane fails to sustain forward flight after transition begins

1. Switch flight mode to QHOVER
2. Attempt to bring aircraft to stable hover

VTOL motors not responsive during transition to quadcopter mode: VTOL motors fail to provide enough lift during transition (significant loss of altitude)

1. Set throttle at 50%
2. Switch mode to FBWA
3. Attempt to bring aircraft to trimmed flight

Incorrect telemetry data: Incorrect or inaccurate data shown in Mission planner

1. Notify pilot in command
2. Bring plane to trimmed flight (during fixed-wing flight),
3. Or, bring the plane to stable hover (during quadcopter flight)
4. Verify if the error persists
5. Switch mode to QHOVER
6. Transition into hovering if in quadcopter mode.
7. Navigate aircraft into the landing area
8. Land
9. Disarm
10. Remove battery
11. Perform post-flight checks

Public entering flying area

1. Notify the public that they are entering an active fly zone
2. Bring the airplane to trimmed flight
3. Switch mode to QHOVER to transition into quadcopter mode
4. If the public is further than 30 meters from the landing area. Navigate aircraft to landing
5. If the public is within 30 meters from lading area, Navigate the aircraft to a rally point
6. Land
7. Disarm
8. Remove battery
9. Perform post-flight checks
10. Report incident

Manned aircraft approaching the flight area: spotted manned aircraft approaching the area or made radio contact with the ground support crew

1. Wait for instructions from the Ground Support team
2. If a manned vehicle will become in conflict with aircraft, lower flight altitude
3. Switch flight mode to QHOVER to begin transition into quadcopter mode
4. Land in aircraft in the closest rally point.
5. Disarm vehicle
6. Recover vehicle
7. Remove the battery
8. Perform a post-flight check

Tether rupture during tethered flight: sudden tether rupture and loss of fixed-wing control

1. Attempt to bring aircraft to trimmed flight
2. Switch flight mode to QHOVER to begin transition into quadcopter mode
3. Navigate the aircraft to the landing area
4. Land
5. Disarm
6. Remove battery
7. Perform post-flight checks

Ground station unexpected behavior: Tether is being reeled in with the plane attached

1. Attempt to shut down the ground station power
2. Bring aircraft to trimmed flight
3. Switch flight mode to QHOVER to begin transition into quadcopter mode
4. Navigate the aircraft to the landing area
5. Land
6. Disarm
7. Remove battery
8. Perform post-flight checks

Fly-Away Emergency Checklist

1. Switch flight mode to RTL on RC transmitter
2. Switch flight mode to RTL on Mission Planner
3. Wait 1 second for Short Failsafe to activate
4. Wait 10 second for Long Failsafe to activate
5. If the plane is still not responsive, attempt to shut down the motors by Disarming to allow gliding descent
6. Inform air traffic control if possible at 1-613-563-5588 (NAV Canada)
    a. Reporting fly-away RPAS, last known location is 2 km East of Shirley, on the British Columbia Highway 14, heading LAST KNOW HEADING, at LAST KNOWN SPEED, and ALTITUDE high, with an expected range of no more than 15 minutes. The aircraft is a 2-meter wingspan foam plane with quadcopter motors the wings are blue, with red and orange stripes.
7. Attempt to recover the aircraft
8. Remove battery
9. Perform post-flight check
10. Submit an incident report

FLIGHT PLAN

This section defines the flight tests to be performed by the AWES quadplane. A common flight plan consists of safely perform vertical take-off, transition into forward flight, perform several crosswind loops, transition into hovering, and vertically land. Each test is performed with the goal of meeting one or more specific objectives. The flight test contains:

1. Test reference number
2. A general overview of the flight test
3. The objective
4. Airplane control type
5. Estimated flight time
6. Flight altitudes
7. Key flight controller parameters
8. Test card with the detailed operation

In addition, each flight plan will contain a pre-flight, during flight, and post-flight checklist

The flight operations are fully described

Test # 1: Airspeed Sensor calibration

Mission Overview: The flight operation consists in performing a wind box in fixed-wing mode to calibrate the airspeed sensor. The operation will be performed in assisted control, where pitch, roll are stabilized by the flight controller. The pilot in command will manually take-off in quadcopter mode, climb to 30 meters high, transition into fixed-wing flight, perform one circle of approximately 100 meter radius, transition back into quadcopter flight, vertically descent, and land in the launch location. The expected duration of the operation is 5 minutes.

Objective: Calibrate the airspeed sensor, evaluate the transition parameters

Control type: Assisted

Flight time: 5 minutes

Flight altitude: 30 meters

Flight controller parameter checks:

PARAMETER	VALUE	UNIT	DESCRIPTION
THR_MAX	100	%	Maximum throttle output
TRIM_ARSPD_CM	1800	cm/s	Trim speed
TRIM_THROTTLE	50	%	Trim throttle
ARSPD_FBW_MIN	16	m/s	Minimum airspeed in FBW mode, transition will begin when value is reached
ARSD_FBW_MAX	25	m/s	Maximum airspeed in FBW mode
Q_ASSIST_SPEED	19	m/s	Speed at which quad motors will stop providing assist lift

Test Card AWEQP001

LAB-SCALE AIRBORNE WIND ENERGY PROTOTYPE

TEST CARD

Small Remotely Piloted Aircraft System: Custom built quadplane

TC registration number: C-1933442617

Airspeed sensor calibration	Init.Volt		Wind Spd.		Take-off time	
AWEQP001	End Volt		Wind Dir.		Landing time	

#	Action	Throttle (%)	Altitude (m)	Airspeed (m/s)	Duration (mm:ss)	Time (mm:ss)	Notes
1	Set QHOVER mode	0	0	0	0:05	0:05	Mode switch 1
2	ARM aircraft	0	0	0	0:05	0:10	
3	Take-off	50	2	0	0:10	0:20	
4	Stabilize hover	40	2	0	0:02	0:22	
5	Vertical climb	50	30	0	0:30	0:52	
6	Set FBWA mode	40	30	0	0:02	0:54	Mode switch 2
7	Transition to forward flight	60	30	16	0:10	1:04	
8	Circle 'home' location	40	30	18	1:00	2:04	
9	Trimmed flight	40	30	18	0:05	2:09	
10	Set QHOVER mode	40	30	18	0:02	2:11	Mode switch 1
11	Transition to hover	30	30	16	0:10	2:21	
12	hover to landing	40	30	5	1:00	3:21	
13	vertical descent	30	2	0	0:30	3:51	
14	Land	30	0	0	0:10	4:01	
15	Disarm	0	0	0	0:05	4:06	

Detailed operation

1. Perform pre-flight checks
2. Set QHOVER mode (first mode switch position)
3. Arm
4. Apply 40% throttle to take-off (hover throttle)
5. Apply 50% throttle to climb vertically up to 30 meters high
6. Apply hover throttle to maintain aircraft stable at 30 meters high
7. Set FBWA mode (second mode switch position)
8. Apply over 50% throttle to start fixed-wing transition
9. Maintain aircraft in straight line until transition is achieved, over 50% throttle might be required
10. Perform one circle of 100 meter radius at an altitude of 30 meters
11. Bring aircraft to trimmed flight
12. Set QHOVER mode (first mode switch position), to shut down the forward motor and begin transition into quadcopter flight
13. Reduce the throttle to hover throttle
14. Bring aircraft to hover
15. Navigate to the landing location
16. Lower throttle to land
17. Disarm
18. Remove battery

Test # 2: Autonomous waypoint tracking in fixed-wing mode at constant altitude

Mission Overview: The flight operation consists in performing a waypoint mission at a constant altitude. The objective is evaluating the autonomous flight control performance in meeting the defined target points, in addition to evaluating autonomous transitions into and out from fixed-wing flight. The autopilot will perform, vertical take-off and climb to an altitude of 50 m, transition into fixed-wing flight, navigate to four waypoints in a figure-8 configuration, return to landing location, transition into quadcopter mode, vertically descend and land. The expected flight time is 5 minutes. Back up pilot is on standby to take manual control in case of deviation from flight path.

Objective: Evaluate the autopilot ability to autonomously follow a series of waypoints

Control type: Autonomous

Flight time: 5 minutes

Flight altitude: 50 meters

Flight controller parameter checks:

PARAMETER	VALUE	UNIT	DESCRIPTION
THR_MAX	100	%	Maximum throttle output
TRIM_ARSPD_CM	1800	cm/s	Trim speed
TRIM_THROTTLE	50	%	Trim throttle
ARSPD_FBW_MIN	16	m/s	Minimum airspeed in FBW mode, transition will begin when value is reached
ARSD_FBW_MAX	25	m/s	Maximum airspeed in FBW mode
Q_ASSIST_SPEED	19	m/s	Speed at which quad motors will stop providing assist lift

Test Card AWEQP002

LAB-SCALE AIRBORNE WIND ENERGY PROTOTYPE

TEST CARD

Small Remotely Piloted Aircraft System: Custom built quadplane

TC registration number: C-1933442617

Const. altitude waypoint tracking	Init.Volt		Wind Spd.		Take-off time	
AWEQP002	End Volt		Wind Dir.		Landing time	

#	Action	Throttle (%)	Altitude (m)	Airspeed (m/s)	Duration (mm:ss)	Time (mm:ss)	Notes
1	Set QHOVER mode	0	0	0	0:05	0:05	Mode switch 1
2	ARM aircraft	0	0	0	0:05	0:10	
3	Set AUTO mode	0	0	0	0:02	0:12	Mode switch 2
4	Take-off	50	3	0	0:10	0:22	
5	Stabilize hover	40	3	0	0:05	0:27	
6	Vertical climb	50	50	0	0:50	1:17	
7	Transition to forward flight	60	50	16	0:10	1:27	
8	Waypoint 1	40	50	18	0:30	1:57	
9	Waypoint 2	40	50	18	0:30	2:27	
10	Waypoint 3	40	50	18	0:30	2:57	
11	Waypoint 4	40	50	18	0:30	3:27	
12	Waypoint 1	40	50	18	0:30	3:57	
13	Return to launch	40	50	18	0:30	4:27	
14	Transition to hover	30	50	16	0:10	4:37	
15	hover to landing	40	50	5	1:00	5:37	
16	vertical descent	30	2	0	0:50	6:27	
17	Land	30	0	0	0:10	6:37	
18	Disarm	0	0	0	0:05	6:42	

Detailed operation

1. Perform pre-flight checks
2. Set QHOVER mode (first mode switch position)
3. Arm
4. Set AUTO mode (Third mode switch position)
5. Operation lead communicates to the crew the phase of the mission:
    a. take-off completed
    b. Defined altitude reached
    c. Transition into forward flight completed
    d. Waypoint # reached
    e. Return to launch activated
    f. Transition into quadcopter mode completed
    g. Navigating to landing area
    h. Landing completed
    i. Disarmed
6. Pilot in command on standby for taking manual control
    a. If needed, take manual control by switching the flight mode to FBWA in fixed-wing flight.
    b. or, take manual control by switching the flight mode QHOVER in quadcopter flight.
7. Disarm aircraft after landing
8. Remove battery

Test # 3: Autonomous waypoint tracking in fixed-wing mode at variable altitude

Mission Overview: The flight operation consists in performing a waypoint mission at a variable altitudes. The objective is evaluating the autonomous flight control performance in meeting the altitude targets, in addition to evaluating forward thrust variation during climbs and dives. The autopilot will perform, vertical take-off and climb to an altitude of 50 m, transition into fixed-wing flight, navigate to four waypoints in a figure-8 configuration with a range of altitudes between 50-80 meters, return to landing location, transition into quadcopter mode, vertically descend and land. The expected flight time is 5 minutes. Back up pilot is on standby to take manual control in case of deviation from flight path.

Objective: Evaluate the autopilot ability to meet altitude targets, and evaluate the forward thrust variation

Control type: Autonomous

Flight time: 5 minutes

Flight altitude: 50-80 meters

Flight controller parameter checks:

PARAMETER	VALUE	UNIT	DESCRIPTION
THR_MAX	100	%	Maximum throttle output
TRIM_ARSPD_CM	1800	cm/s	Trim speed
TRIM_THROTTLE	50	%	Trim throttle
ARSPD_FBW_MIN	16	m/s	Minimum airspeed in FBW mode, transition will begin when value is reached
ARSD_FBW_MAX	25	m/s	Maximum airspeed in FBW mode
Q_ASSIST_SPEED	19	m/s	Speed at which quad motors will stop providing assist lift

Test Card AWEQP003

LAB-SCALE AIRBORNE WIND ENERGY PROTOTYPE

TEST CARD

Small Remotely Piloted Aircraft System: Custom built quadplane

TC registration number: C-1933442617

Var. altitude waypoint tracking	Init.Volt		Wind Spd.		Take-off time	
AWEQP003	End Volt		Wind Dir.		Landing time	

#	Action	Throttle (%)	Altitude (m)	Airspeed (m/s)	Duration (mm:ss)	Time (mm:ss)	Notes
1	Set QHOVER mode	0	0	0	0:05	0:05	Mode switch 1
2	ARM aircraft	0	0	0	0:05	0:10	
3	Set AUTO mode	0	0	0	0:02	0:12	Mode switch 2
4	Take-off	50	3	0	0:10	0:22	
5	Stabilize hover	40	3	0	0:05	0:27	
6	Vertical climb	50	50	0	0:50	1:17	
7	Transition to forward flight	60	50	16	0:10	1:27	
8	Waypoint 1	40	50	18	0:30	1:57	
9	Waypoint 2	40	80	18	0:30	2:27	
10	Waypoint 3	40	50	18	0:30	2:57	
11	Waypoint 4	40	80	18	0:30	3:27	
12	Waypoint 1	40	50	18	0:30	3:57	
13	Return to launch	40	50	18	0:30	4:27	
14	Transition to hover	30	50	16	0:10	4:37	
15	hover to landing	40	50	5	1:00	5:37	
16	vertical descent	30	2	0	0:50	6:27	
17	Land	30	0	0	0:10	6:37	
18	Disarm	0	0	0	0:05	6:42	

Detailed operation

9. Perform pre-flight checks
10. Set QHOVER mode (first mode switch position)
11. Arm
12. Set AUTO mode (Third mode switch position)
13. Operation lead communicates to the crew the phase of the mission:
    a. take-off completed
    b. Transition altitude reached
    c. Transition into forward flight completed
    d. Waypoint # reached at altitude
    e. Return to launch activated
    f. Transition into quadcopter mode completed
    g. Navigating to landing area
    h. Landing completed
    i. Disarmed
14. Pilot in command on standby for taking manual control
    a. If needed, take manual control by switching the flight mode to FBWA in fixed-wing flight.
    b. or, take manual control by switching the flight mode QHOVER in quadcopter flight.
15. Disarm aircraft after landing
16. Remove battery

Appendix C

List of Materials

Qty	Part	Site
1	Volantex Phoenix V2 759-2 2000mm Wingspan EPO Sport Aerobatic Glider RC Airplane PNP	https://www.banggood.com/Volantax-Phoenix-V2-759-2-2000m-Wingspan-EPO-Sport-Aerobatic-Glider-RC-Airplane-PNP-p-1311032.html?rmmds=buy&cur_warehouse=CN
1	Pixhawk 4(plastic case)&GPS (UBLOX NEO-M8N)&PM07	https://shop.holybro.com/pixhawk-4beta-launch_p1089.html
1	100mW Telemetry Radio V3 915MHz	https://shop.holybro.com/transceiver-telemetry-radio-set-v3_p1103.html
1	Pixhawk Digital Airspeed Sensor w/ Pitot Tube	https://hobbyking.com/en_us/pixhawk-digital-airspeed-sensor-w-pitot-tube.html
1	Turnigy 9X 9Ch Transmitter w/ Module & iA8 Receiver (Mode 2) (AFHDS 2A system)	https://hobbyking.com/en_us/turnigy-9x-9ch-transmitter-w-module-ia8-receiver-mode-2-afdhs-2a-system.html
4	Turnigy Graphene Battery 5000mAh 4S 45C Lipo Pack w/XT90	https://hobbyking.com/en_us/graphene-5000mah-4s-45c-w-xt90.html
1	iSDT T6 Lite Charger (600W)	https://hobbyking.com/en_us/isdt-t6-lite-600w-charger.html
4	Turnigy Aerodrive SK3 - 3536-1200kv Brushless Outrunner Motor	https://hobbyking.com/en_us/turnigy-aerodrive-sk3-3536-1200kv-brushless-outrunner-motor.html
3	Quanum Carbon Fiber Propeller 11x5 (CW/CCW) (2pcs)	https://hobbyking.com/en_us/quanum-carbon-fiber-propeller-11x5-cw-ccw-2pcs.html
4	Turnigy Plush-32 40A Speed Controller w/BEC	https://hobbyking.com/en_us/turnigy-plush-32-40a-speed-controller-w-bec.html
2	CC Carbon Fiber Tube Twill 16mm x 14mm x 1.2m	https://shop.compositescanada.com/#/product/CFT-16X14TW
2	AOWISH 1 Pair XT60 Male/Female Connector with 10CM Silicone Wire Cable 14AWG for RC Lipo Battery	https://www.amazon.ca/gp/product/B07H5HRYCY/ref=ox_sc_act_title_2?smid=A1IN3SS47QRDR0&psc=1
2	PolyMax 3.5mm Gold Connectors 10 PAIRS (20PC)	https://hobbyking.com/en_us/polymax-3-5mm-gold-connectors-10-pairs-20pc.html
1	TL-242 Thread Locker & Sealant Medium Strength	https://hobbyking.com/en_us/tl-242-thread-locker-sealant-medium-strength.html
1	AGW 18 wire (12m)	

Appendix D

Part Drawings

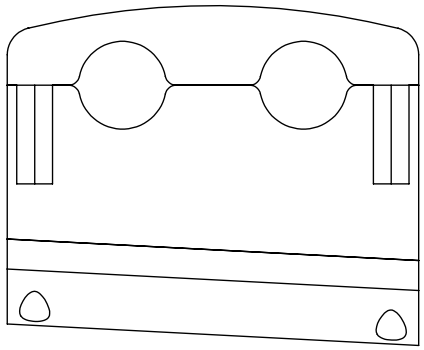

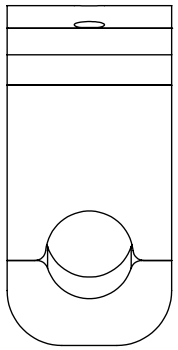

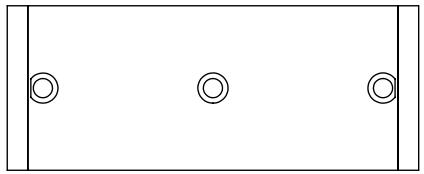

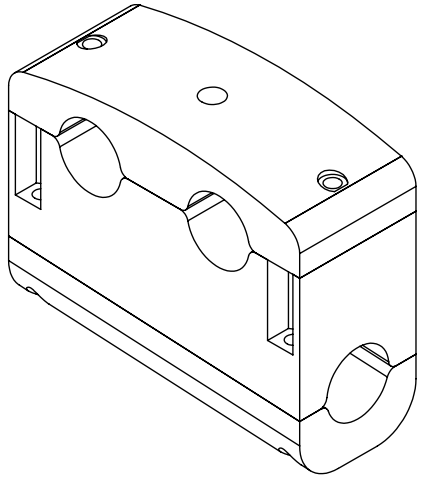

Boom mount assembly	PLA (3D printed)	Quadplane	Andreas Klein-Miloslavich

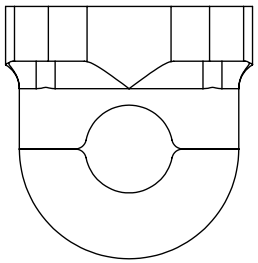

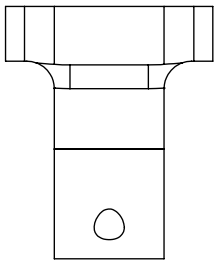

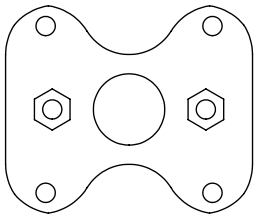

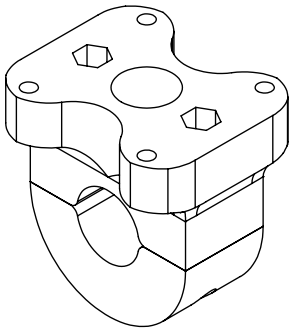

Motor mount assembly	PLA (3D printed)	Quadplane	Andreas Klein-Miloslavich